Politecnico di Torino

ScuDo
Scuola di Dottorato ~ Doctoral School
WHAT YOU ARE, TAKES YOU FAR

Doctoral Dissertation
Doctoral Program in Electronics and Telecommunications Engineering (35^{th}cycle)

Development of self-assembled hyperbolic metamaterial-based photonic devices for enhanced single-photon sources

By

Marwan Channab

******

Supervisor(s):
Prof. C. F. Pirri, Supervisor
Dr. A. Angelini, Co-Supervisor

Doctoral Examination Committee:
Prof. A.B. , Referee, University of...
Prof. C.D, Referee, University of...
Prof. E.F, University of...
Prof. G.H, University of...
Prof. I.J, University of...

Politecnico di Torino
2023

Declaration

I hereby declare that, the contents and organization of this dissertation constitute my own original work and does not compromise in any way the rights of third parties, including those relating to the security of personal data.

Marwan Channab
2023

* This dissertation is presented in partial fulfillment of the requirements for **Ph.D. degree** in the Graduate School of Politecnico di Torino (ScuDo).

I would like to dedicate this thesis to the ones who chase their passion

Acknowledgements

I would like to thank my supervisors Prof. Fabrizio C. Pirri and Dr. Angelo Angelini for giving me the opportunity to work on this exciting topic and for their precious advices during my PhD research. I feel lucky to have had the chance to share brilliant and interesting scientific discussions with them.

And I would like to acknowledge also all the members of the Istituto Nazionale di Ricerca Metrologica (INRiM) Advanced Materials and Devices group for their continuous support and collaboration during my experience.

I want also to thank Dr. Fernando Castro and his group for hosting me at the National Physical Laboratory (NPL) during my activities. In particular, I want to acknowledge Dr. Yameng Cao and Dr. Sebastian Wood who collaborated with me during my experience at NPL in Teddington (UK). It has been a pleasure to meet you and to work together on something that was unexplored for me.

Last but not least, I want to express my deepest gratitude to the friends that I met during my PhD work. Without their friendship and support my PhD would have been less extraordinary.

Abstract

This Thesis is focused on the development and characterization of self-assembled hyperbolic metamaterials-based photonic devices for enhanced single-photon sources.

In the last decades, different kinds of single-photons sources (SPSs) have been deeply studied for the development of photonic devices in fields such as quantum computing, quantum communication and metrology. Unfortunately, most of the SPSs are characterized by drawbacks that limit their applications. For example, a solid-state SPS such as Nitrogen-Vacancy (NV) in diamond lattice is featured by low emission rate and a broadband emission. To overcome such limitations, we propose the exploitation of self-assembled hyperbolic metamaterials.

Hyperbolic metamaterials (HMMs) are artificial material designed to provide optical properties that cannot be found in natural materials. They are usually composed of two alternating materials: a metal and a dielectric. HHMs are characterized by periodic structures with typical periodicity dimensions (Δ) that are much smaller than the incident wavelength of interest. In this work, the typical dimensions are at the nanoscale since the incident wavelengths of interest are in the visible range, i.e. $\Delta \sim 40$ nm. The nanostructured materials introduce an anisotropy in the permittivity tensor that leads to a hyperbolic isofrequency surface. The exotic isofrequency surface shape enables two interesting optical properties: the directional emission and the increase of the available optical states, and consequently the enhancement of the spontaneous emission. Hence, properties allow to overcome some of the typical limitations of solid-state SPS.

In order to fabricate the HMMs, self-assembling block copolymers (BCPs) have been used. BCPs are composed of two or more immiscible homopolymer chains linked by a covalent bond. The most interesting characteristic of BCPs is represented by their capability to organize themselves in periodic nanostructures. The self-assembly can be induced by providing thermal energy by means of an

annealing process. By exploiting BCP self-assembly different final morphologies can be obtained by varying the volume fraction: gyroids, cylinders, and spheres. In this Thesis, we focused our attention on the fabrication of lamellae perpendicular to the substrate. Then, the polymeric lamellar nanostructure has been used to obtain a hyperbolic metasurface composed of lamellae made of gold and air.

To investigate the proposed hyperbolic metasurface, the sustained modes have been calculated through modal analysis exploiting quasi-normal modes formalism. In addition, simulations have been performed by means of Finite Element Method software Comsol Multiphysics 5.2 to study the optical response of the hyperbolic metasurface, in terms of emission enhancement, when coupled to a dipole as photon emitter. The obtained results showed a good agreement with the experimental optical characterization for what concerns the wavelength region where the enhancement occurs. The measurements have been performed analyzing the photoluminescence emission of NVs in nanodiamonds dispersed on the fabricated hyperbolic metasurfaces.

In addition, in this dissertation we discuss the fabrication of a tool for the estimation and characterization of the increased number of available optical states: a diamond-based nano-probe for optical near-field characterization. The proposed probe is composed of an Atomic Force Microscopy (AFM) tip with an emitting nanodiamond on top of it.

Finally, we present further techniques for the fabrication and optical characterizations of self-assembled hyperbolic metamaterials that will be used to enhance single-photon sources' emission.

Contents

List of Figures

Chapter 1

Single Photon Sources

In this first chapter, we introduce Single Photon Sources (SPS), focusing particularly on their properties and quantum applications. We describe the theoretical parameter used to determine the nature of quantum light source. Then main SPSs at the state of art are presented.

1.1 Ideal Single Photon Properties

When a system can emit a single photon at a time after a sent trigger signal, we are observing a single photon source. An ideal SPS should possess the following emission features [1]:

- **Monochromatic**: in order to optimize the quantum indistinguishability of photons, as well as the optical transport and detection protocols
- **On demand**: for every sent excitation the ideal source should emit one single photon with high efficiency and reliability
- **Bright**: corresponds to a source with a short lifetime and consequently to a high emission rate

1.2 Single Photon Sources: fundamentals

In the first part of this section, we introduce the theoretical parameter used to characterize whether a light emitter is a single photon source. While in the second part we evaluate this parameter for different kinds of photon sources in order to show how its value can easily determine the nature of the emitted light under investigation.

1.2.1 The second-order autocorrelation function

As mentioned before, it is necessary to define a criterion in order to characterize the quantum nature of the light emitted by a photon source. Usually, as criterion and parameter, the second-order autocorrelation function, also referred to as $g^{(2)}(\tau)$, is applied for the determination of the single photon nature [11]. Since this function is evaluated when $\tau = 0$, hence when the time delay is equal to zero between two photons, it is straightforward that this condition leads to a value that approaches zero when we are considering an SPS. Here, we report the definition of $g^{(2)}(\tau)$:

$$g^{(2)}(\tau) = \frac{< I(t) \cdot I(t+\tau) >}{< I(t) >^2} \tag{1.1}$$

Where the intensities of the electromagnetic field at two different times are represented by I (t) and I (t + τ). Exploiting the quantum mechanics field theory, we can rewrite this formula through the operators of creation and destruction, respectively $\hat{a}^\dagger$ and $\hat{a}$, obtaining the following result:

$$g^{(2)}(\tau) = \frac{< \hat{a}^\dagger \cdot \hat{a}^\dagger \cdot \hat{a} \cdot \hat{a} >}{< \hat{a}^\dagger \cdot \hat{a} >< \hat{a}^\dagger \cdot \hat{a} >} \tag{1.2}$$

Assuming $\tau \to 0$:

$$\lim_{\tau \to 0} g^{(2)}(\tau) \approx g^{(2)}(0) = \frac{< \hat{a}^\dagger(t) \cdot \hat{a}^\dagger(t+\tau) \cdot \hat{a}(t) \cdot \hat{a}(t+\tau) >}{< \hat{a}^\dagger(t) \cdot \hat{a}(t) >^2} \quad (1.3)$$

Considering the following relations between the operators:

$$\hat{a} \left| n \right\rangle = \sqrt{n} \left| n-1 \right\rangle \quad (1.4)$$

$$\hat{a}^\dagger \left| n \right\rangle = \sqrt{n+1} \left| n+1 \right\rangle \quad (1.5)$$

$$\hat{a}\hat{a}^\dagger = \hat{n} \quad (1.6)$$

$$\hat{n} \left| n \right\rangle = n \left| n \right\rangle \quad (1.7)$$

$$[\hat{a}^\dagger(t_1), \hat{a}(t_2)] = \delta_{t_1,t_2} \quad (1.8)$$

Here the number of photons is represented by the state $|n\rangle$, also referred to as *Fock state* for a quantized monochromatic field with n photons and an angular frequency ω.

At this point we obtain the final form of our parameter $g^{(2)}(0)$:

$$g^{(2)}(0) \sim \frac{< \hat{n}^2 > - < \hat{n} >}{< \hat{n} >^2} \quad (1.9)$$

Observing the equation is straightforward to note that for a state with a single photon, n = 1, the $g^{(2)}(\tau)$ is equal to zero. It is worth to notice that this case is reachable only in ideal conditions, indeed if we consider the real-world experimental procedures we have several non-idealities represented by the background noise and dark counts from the detectors that may affect the evaluation of $g^{(2)}(0)$ during the characterization.

Hence, we have to regard the $g^{(2)}(0)$=0 as an ideal limit. This is translated in an estimation of $g^{(2)}(0)$ value that has to be less than the threshold value corresponding to two emitted photons in order to safely determine a single photon source:

$$g^{(2)}(0) < 0.5 \tag{1.10}$$

1.2.2 Photon Sources Classification

Here, we consider different kinds of light sources: coherent sources, thermal sources, and SPS. In order to simplify the evaluation of $g^{(2)}(\tau)$ we assume the following expression for each source:

$$g^{(2)}(\tau) = 1 + \frac{\int P(\varepsilon)(|\varepsilon|^2 - <|\varepsilon|^2>)\,d\varepsilon}{<|\varepsilon|^2>} \tag{1.11}$$

Where $P(\varepsilon)$ represents a finite probability distribution in order to obtain $g^{(2)}(0) \geq 1$ for a classical light source. Now we can distinguish the three types of above-mentioned sources.

Coherent source

A well-known example of this category of light source is the laser. In this case, this kind of source is described by means of a coherent state $|\alpha\rangle$, moreover, the eigenvectors of the destruction operator can be considered in Fock's basis with the following expression:

$$|\alpha\rangle = \sum_n c_n |n\rangle \tag{1.12}$$

For this kind of source the probabilistic distribution is Poissonian, always considering as the distribution's average value μ, we obtain the following formulas:

$$P_n = \frac{\mu^n e^{-n}}{n!} \tag{1.13}$$

$$\Delta n = \sqrt{\mu} \tag{1.14}$$

Observing these formulas and the following equation for $g^{(2)}(\tau)$, we can see that for a coherent source the $g^{(2)}(\tau)$ is equal to 1 for every τ value, even for $\tau = 0$.

$$g^{(2)}(\tau) = 1 + \frac{< (\Delta\hat{n})^2 > - < \hat{n} >}{< \hat{n} >^2} \tag{1.15}$$

This can be intuitively explained by the fact that coherent sources have constant intensity. In addition, the fact that coherent light has $g^{(2)}(\tau)$=1 for any τ can be interpreted as the manifestation of the randomness of the Poissonian photon statistics.

Thermal sources

One of the most common light sources of this kind is an incandescent lamp. In this case, we can formalize the description of photon state by means of thermal states, in particular, we report the number of photons statistics distribution for thermal states:

$$P_n = \frac{1}{1-\mu}\left(\frac{\mu}{\mu+1}\right)^n \tag{1.16}$$

Where μ is the average value. This leads to the second-order autocorrelation values reported here:

$$g^{(2)}(\tau) = 2 \qquad \tau = 0 \tag{1.17}$$

$$g^{(2)}(\tau) \to 1 \qquad \tau \to \infty \tag{1.18}$$

Single photon source

As we have stated previously, the photonic states emitted by an SPS can be described by Fock's states $|n\rangle$. Considering the Eq. 1.10 we can express $g^{(2)}(\tau)$ with this formula:

$$g^{(2)}(\tau) \sim 1 - \frac{1}{n} < 1 \tag{1.19}$$

We can see that for a single photon source, with an n = 1 the parameter value is equal to zero, while if we have under investigation a source that emits two photons the function value will be 0.5, and so on. It is clear that the limit case is represented by the coherent light ($g^{(2)}(0)=1$), and therefore the SPSs are the manifestation of the quantum nature of light. In this way, we are moving from classical optics to *quantum optics*.

At this point, it is straightforward that the value of the $g^{(2)}(0)$ function can determine the light source nature. We can summarize the obtained results in the following figure also reported as *antibunching curves*:

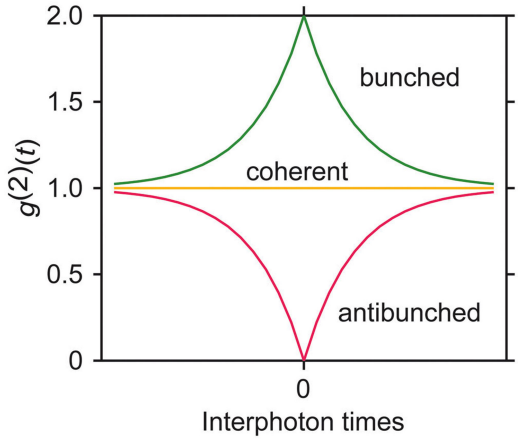

Fig. 1.1 Scheme of the possible antibunching curve's results with different kinds of sources: SPS (antibunched), laser (coherent), and thermal sources (bunched) [12]

1.3 Single Photon Sources: State of Art

In this section, we analyze the different platforms commonly used in order to generate single photons. In particular, we focus on solid-state sources such as strongly attenuated lasers, parametric down-conversion, quantum dots, 2D materials, and solid-state defects in diamonds.

1.3.1 Strongly attenuated lasers

First, we report here the strongly attenuated lasers that are probabilistic single photon sources. In this case, the lasers are strongly attenuated by simply applying neutral optical filters in order to statistically reach the emission of single photons. For the simplicity of this approach, they have been the first devices exploited for the generation of single photons, and nowadays they are commonly used in commercial systems for quantum cryptography. Since the emission has a Poissonian distribution, strongly attenuated lasers have a stochastic nature. Moreover, they have two main drawbacks: a large multi-photonic component, related due to the stochastic nature, and a not on-demand nature, instead as requested for an ideal single photon source[13, 14].

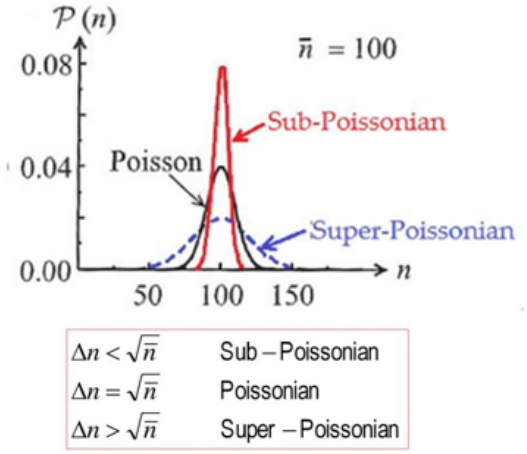

Fig. 1.2 Example of a Poisson photon distribution with an average value equal to 100 photons. In the graph, sub-Poissonian and super-Poissonian distributions are reported too. In these cases, the variance is $\Delta n < \sqrt{\bar{n}}$ and $\Delta n > \sqrt{\bar{n}}$, respectively.

1.3.2 Parametric down-conversion

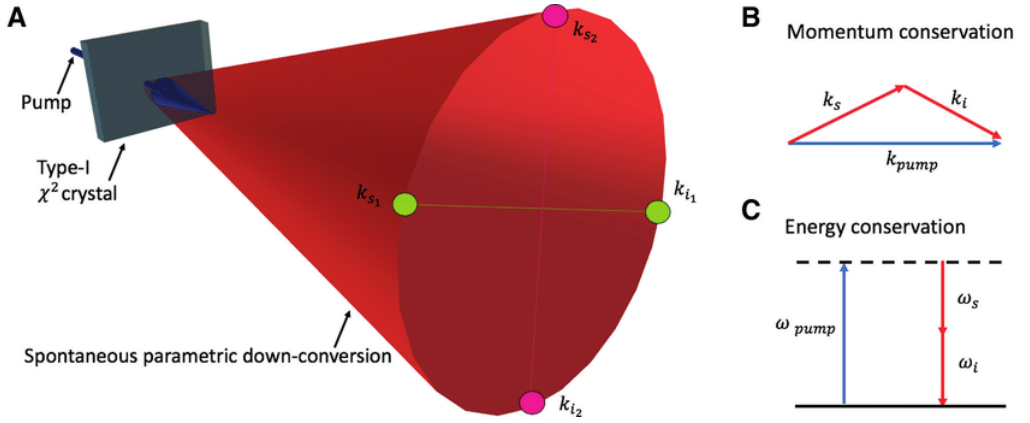

Fig. 1.3 Schematical representation of the parametric down-conversion process with the conservation of energy and momentum [15]

This kind of process occurs only in some crystals characterized by non-linear effects. These effects are related to second-order electrical susceptibility that is not equal to zero. Unfortunately, the parametric down conversion is not a deterministic approach to obtain single photons. In this process, we have the emission of entangled quantum states of light: pairs of photons that are correlated. As reported in literature [16, 17],

in the photon pair one photon is the so-called "signal" and the other one "idler". They show correlation properties that have not classical analogous. The photon pair has correlated polarizations and moreover, it is phase-matched in the frequency domain too. We refer usually to the same polarization as type 1 and to perpendicular polarizations as type 2. It is worth to notice that between consecutive photon pairs the polarization correlation does not exist. From the experimental point of view, the photon emission is related to the excitation of the non-linear crystal by means of a UV pump laser. While this process occurs, there is no energy exchange between excitation photons and the crystal, hence the crystal has no variations too. In this way, the input photon simply moves from the initial state to the final one. In addition, we can easily detect the presence of a photon of the pair by the revelation of the other photon. This feature plays a key role in quantum information since we have "heralded" photons. Another interesting feature is the strongly directional emission. Even if this process may seem simple and suitable for different quantum optical applications, it has a great limitation [18] due to the fact that this category of SPS is not on-demand since the photon creation is a probabilistic process. Furthermore, this process has a success probability of the order of 10^{-10}. For this practical reason, it results in a difficult creation of the signal.

1.3.3 Quantum dots

Quantum dots are another important example of solid-state single-photon sources [19–23]. A Quantum Dot (QD) has a nanostructure composed of semiconductor material within another semiconductor with a larger bandgap, see Fig.1.4. In particular, the inner semiconductor has dimensions that are comparable to the De Broglie wavelength. With this kind of structure, we can generate a three-dimensional potential in which particles, i.e. electrons, can be confined inside a region with a nanometric spatial dimension. This leads to strongly quantized energy levels. In this nanometric structure, we can have photoluminescence. Indeed, when light absorption occurs in the QD, an electron is excited from the valence to the conduction band, hence a hole is created in the valence band. Then the electrons and holes can recombine, leading to photon emission. Since the dimensions of the QD affect the confinement energy, it is possible to tune the absorption and photoluminescent emission by varying the size in the synthesis process (i.e. colloidal synthesis). For instance, a shift towards lower energy values, a red-shift, is observable when there is an increase

in the sizes. Whilst by decreasing sizes, a blu-shift occurs. In addition, the QD's dimension can determine not only the photon energy but the luminescence lifetime too. This is due to the fact that smaller dots are characterized by larger energy steps between the levels in which the particles are trapped. Hence, electron-hole pairs can be trapped for less time. Since they can be excited also electrically, it is possible to have electroluminescence. For these reasons, they are reliable on-demand SPS. Nonetheless, their application as SPSs is limited since they can operate as SPS only at cryogenic temperatures. This drawback must be considered a huge limitation, indeed such technologies are supposed to be implemented within everyday devices at room temperature to be widely used.

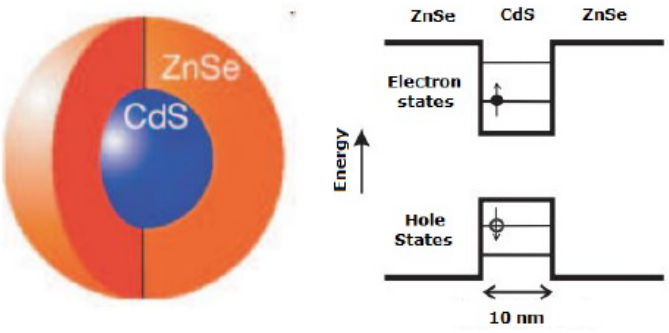

Fig. 1.4 Schematical representation of a quantum dot and its quantized energy levels.

1.3.4 2D materials

Only in the last years, 2D materials have attracted the attention of the quantum optics community. They have been deeply investigated recently since they possess exotic and very interesting features for what concerns quantum optical applications. Indeed, they can act not only as SPS but also as memories in quantum computing technologies [135]. In these years, the most studied 2D material is surely graphene. This single-atomic monolayer composed of carbon atoms has remarkable properties which make it very appealing for different applications since it has diamond robustness and plastic flexibility. This is possible since it is characterized by atoms that form hexagons, with 120° angles, and have sp^2 hybridized bonds. These properties make it the ideal silicon substitute in electronics, allowing the improvement of nowadays performances. In addition, graphene has played another key role indeed it has renewed the interest

in 2D materials especially the inorganic ones with exotic optical and electronic properties such as the transition metal dichalcogenides (TMDCs). Indeed since their optical properties can be engineered and integrated into photonics devices [24–27], they have been subject of interest for decades. In fact, it is worth to notice that TMDCs have been studied for years, but it is only with the recent development of new technologies for nanoscale characterization that TMDCs have been considered for nanoelectronic and optoelectronic devices such as transistors, photon detectors, and electroluminescent devices. Moreover, in this kind of material the photon emission is related to trapped excitons, particles formed by bound electrons and holes, that may recombine. This recombination enables the single photon emission. Unfortunately, similarly to QDs, the single photon emission occurs only at cryogenic temperature. In these 2D materials, we can observe layers stacked together by means of Van Der Waals interactions. In this way, it is possible to exfoliate the stacked layers into 2D layers with the thickness of a single unit cell enabling strong in-plane bonding. TMDCs are composed of a transition metal element, i.e. groups IV, V, and VI such as Mo, W, and a chalcogen such as S, Se, or Te. We can find them with the layered structure of form X–M–X, where X is chalcogen and M is the transition metal. We report their structure in the following figure Fig. 1.5 with the chalcogen atoms in two hexagonal planes separated by a plane of metal atoms, as shown in Fig 1.5b.

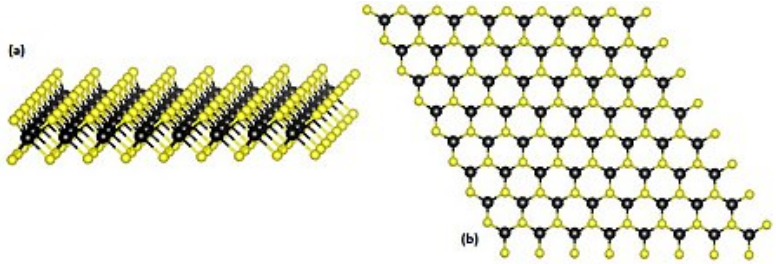

Fig. 1.5 TMDC typical lattice: we can see very clearly that the chalcogen atoms are in two hexagonal planes separated by a plane of transition metal atoms

1.3.5 Solid-state defects in diamond

In this paragraph, we discuss one of the most promising single photon sources: atom-like defects in diamonds, also known as color centers since they usually emit in the visible range. They have different significant properties as SPS, indeed they can emit on-demand and they have high quantum efficiency, defined as the ratio between radiative and non-radiative decay rates. In addition, they can be produced very easily by means of ion implantation. The description of these color centers is straightforward since they can be observed as a quantum system with two or three levels. Unfortunately, the third level so-called *shelving state* leads to a strong decrease in the emission rate since the *shelving state* has lifetime values that are 100-1000 times the values of the other two states [28, 29]. Another important feature is the fact that in principle they can be integrated into everyday devices since they can operate at room temperature too. Nonetheless, until now the other kind of sources can not be replaced by color centers since they are characterized by low emission rates with respect to the previous SPS. In particular, in this Thesis, we report the use of Hyperbolic Metamaterials (HMM), in order to overcome this limitation by reaching a higher emission rate and collection efficiency. The different kinds of defects in the diamond lattice are reported in the literature: substitutionals, interstitials, and vacancies. Substitutional defects can be found when a carbon atom has been replaced by a different element. The interstitial defects are formed by additional atoms in the lattice placed between the atomic positions. The vacancy defects are simply formed by a carbon atom that is missing. Moreover, we can have also different combinations for example a silicon vacancy (SiV). All these defects can be observed in Fig 1.6:

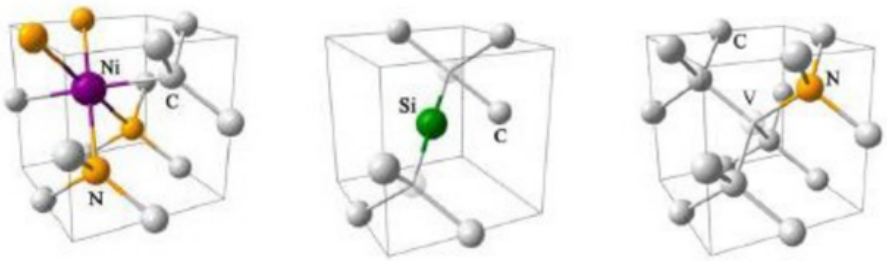

Fig. 1.6 Different types of possible structures for color centers [30]: on the left a substitutional defect with a Ni atom, on the center an interstitial defect with a Si atom, and on the right a combination of a vacancy with a substitutional N atom (Nitrogen-Vacancy center) [30].

The presence of impurities in the lattice introduces additional electronic levels that would be forbidden, enabling new radiative transitions. When there is no phononic interaction in the lattice the transition is called Zero Phonon Line (ZPL), but this condition has a higher probability at cryogenic temperatures. Indeed, at room temperature, while the electrons are excited and transitions occur, the transition electrons interact with phonons. This effect results in a broadening of the emission spectrum and it will show phonon sidebands as reported in the following figure:

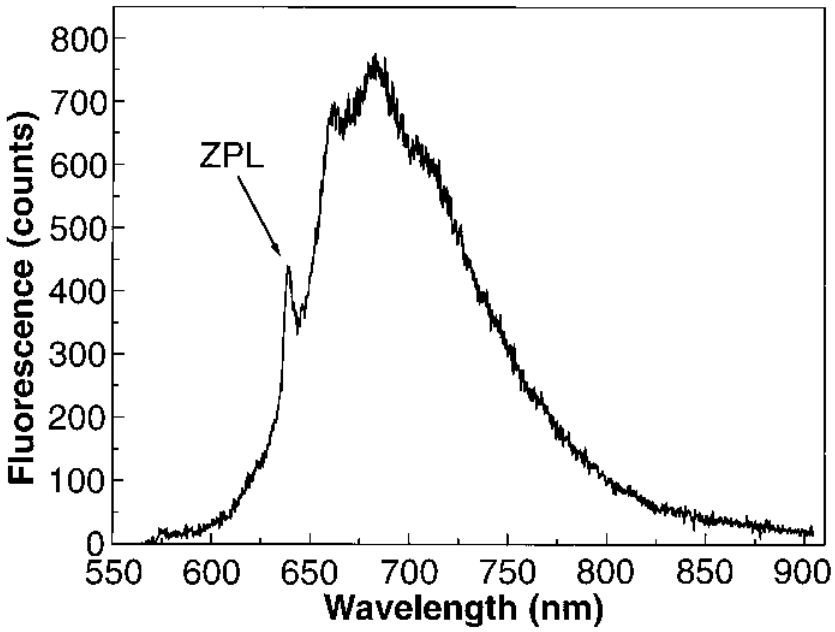

Fig. 1.7 Emission spectrum for NV center with its phonon sideband [31], reprinted with permission from AAAS

The nitrogen-vacancy center referred to as the NV center, has been the most studied color center in the last years [32–38] and in particular, we have exploited it for our experimental activities. As the name suggests, the defect is composed of a substitutional nitrogen atom in proximity to a carbon vacancy.

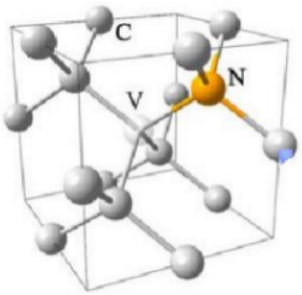

Fig. 1.8 NV center structure [30]

Moreover, NV centers can have two different charge states: NV^- and NV^0 center. If we consider the negative charge that is due to an additional electron captured, in this case, the emission spectrum presents the ZPL emission at 637 nm with a broad phonon band, see Fig. 1.7. From the applications point of view, this charged state is more interesting for what concerns quantum computing and sensing, since it has a triplet spin S=1. Indeed, the metastable state enables the opportunity of converting the spin state of the system via a transition [39]. Once the NV^- center has been excited after a time comparable with the metastable state's lifetime, around 10^{-7} s, the *inter-system crossing* can be enabled leading the system spin state into the ground state with $m_s = 0$ even if the starting state was with $m_s = 1$. The process is also known as *optical cooling*. This represents the chance to initialize the state of the quantum system. Moreover, NV^- lifetime is too long for quantum communication devices, because of the shelving state presence as mentioned before, see Fig 1.9.

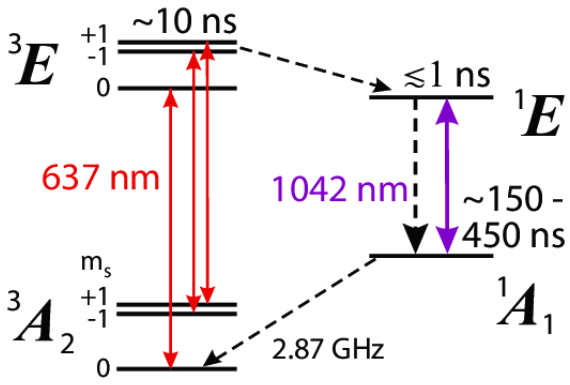

Fig. 1.9 The NV^- center possible transitions in the three-level system: the red lines represent the photon transition, the purple line the phonon relaxation and the dash lines the inter-system crossing [40]

If instead, we consider the NV center neutral state, we have a doublet spin for the electronic structure with the ground and excited states (S = $\frac{1}{2}$). In this case, the emission spectrum shows a ZPL emission 575 nm with a broad phonon band at lower energies.

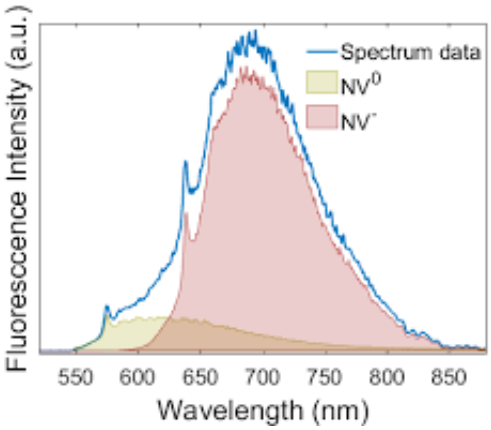

Fig. 1.10 The NV center possible spectra from the two different charge states [41]

Indeed, the ZPL emission is only the 4 % of the photons emitted. This happens in both charge states as can be seen in Fig 1.10, resulting in a broadened spectrum. As above-mentioned, this is one of the most significant drawbacks related to these color centers when we consider their application as SPSs.

1.4 Single Photon Sources applications

1.4.1 Cryptography: Quantum Communication

Cryptography has always had a crucial role in our society, since establishing a safe communication channel was important to exchange sensitive information with intruders even in the past. Indeed, the word cryptography takes its origin from the Greek, "hidden writing", and we use it to refer to a technique exploited to transmit messages safely. This could be obtained by sharing particular information between the authorized interlocutors: the cryptography key. Without the *key* the message is not readable. The message, a combination of letters or bits, will result comprehensible only by combining it with its key through a suitable algorithm. The creator of the cipher known as "one-time pad" Gilbert Vernam is considered the

father of modern cryptography [2, 3]. He suggested using random keys as long as the message and only years later it was demonstrated by Claude Shannon that this methodology results in an inviolable technique [140]. In other words, the message could be decrypted in principle when the key is shorter than the message. One of the most famous secure communication protocols, the Enigma machine used by Germany during World War II, employed a much shorter key with respect to the message and the allied forces decrypted the messages. This historic example shows how important can be the production of safe keys and this is still valid since nowadays for cryptography we use a technique based on key distribution (KD). The cryptographic protocols that use this method can be divided into two main categories: symmetric and asymmetric protocols. In the first category, the same key is used for the encryption of the message and also for its decoding. In this case, the main limitation lies in the practical difficulty in sharing safely the key between the two interlocutors. On the other hand, the asymmetric category exploits two different keys to encrypt and decrypt the message. In this way, through a communication public channel, the message can be easily transmitted since it will be indecipherable by intruders, with the only exception of the recipient who is the only owner of the algorithm that decrypts the content of the message. In this context, the *Quantum Key Distribution* (QKD) represents not only an innovation in the key distribution but a revolutionary step towards an inviolable communication protocol. In this way, we can use a set of protocols, systems, and procedures already elaborated by mathematically safe systems (like the Vernam one) to encrypt, transmit and decrypt information while to produce and distribute cryptographic keys we exploit the properties of quantum mechanics. Here the advantages of the QDK are reported:

- This technique is based on the validity of universal physical laws combined with a cryptographic technique whose inviolability is assured by a mathematical proof (Shannon)
- It is possible to detect a possible intruder to the involved interlocutors.
- It is impossible to measure a priori the state of an unknown quantum system without modifying or destroying it, therefore without perturbing it. This is formally expressed by the quantum no-cloning theorem.

Hence, this cryptographic technique will remain safe even if we had a machine with the computational capacity of deciphering any key.

One of the most famous quantum protocols is represented by the "BB84", proposed by Bennet and Bressard in 1984 [4]. Subsequently demonstrated in 1992 exploiting coherent attenuated sources [5]. With this protocol, the information can be safely transmitted and codified through the polarization of exchanged photons. Since the sender is always referred to as A, and the receiver as B in literature we usually refer to them as "Alice" and "Bob". Instead, an eavesdropper is conventionally referred to as Eve. In the BB84 protocol, Alice has got a single photon source of polarized photons which she can control and change randomly the polarization of each photon in 4 different orientations that correspond to two non-orthogonal bases. For example, we can consider the first one composed of vertical and horizontal polarizations (rectilinear), in this case, the photon states will be indicated with $|\updownarrow\rangle$ and $|\leftrightarrow\rangle$. Instead, the other base is composed of the two opposite diagonal components, indicated with $|\nearrow\rangle$ and $|\nwarrow\rangle$. At this point, Alice may send a sequence of photons randomly polarized to Bob. From his side, Bob may choose one of the two bases to measure the photon states. For instance, he could choose a diagonal base and if the sent photon was encoded in the same base, he will measure the correct polarization state. Instead, Bob may detect the two different polarization states with the same probability (50% for each polarization) when the photon was encoded in the other base. Afterward, when many photons have been sent, in order to consider only the photons decoded correctly Alice shares the sequence of employed bases with Bob through a public (unsafe) communication line and Bob does the same toward Alice. After that, they do not take into account the photons that were decoded with different bases in the encoding. So, statistically, only 50% of the sequence can survive in this process. The survived sequence of the encoded photons will be used as their key and exploited to encrypt the message. For example, they can assign binary values to the two states ($|\updownarrow\rangle$ and $|\nwarrow\rangle = 1$ and $|\nearrow\rangle$ and $|\leftrightarrow\rangle = 0$). So, a binary sequence can be easily obtained and the encoding and decoding can be implemented with the OR operator between the key and the message.

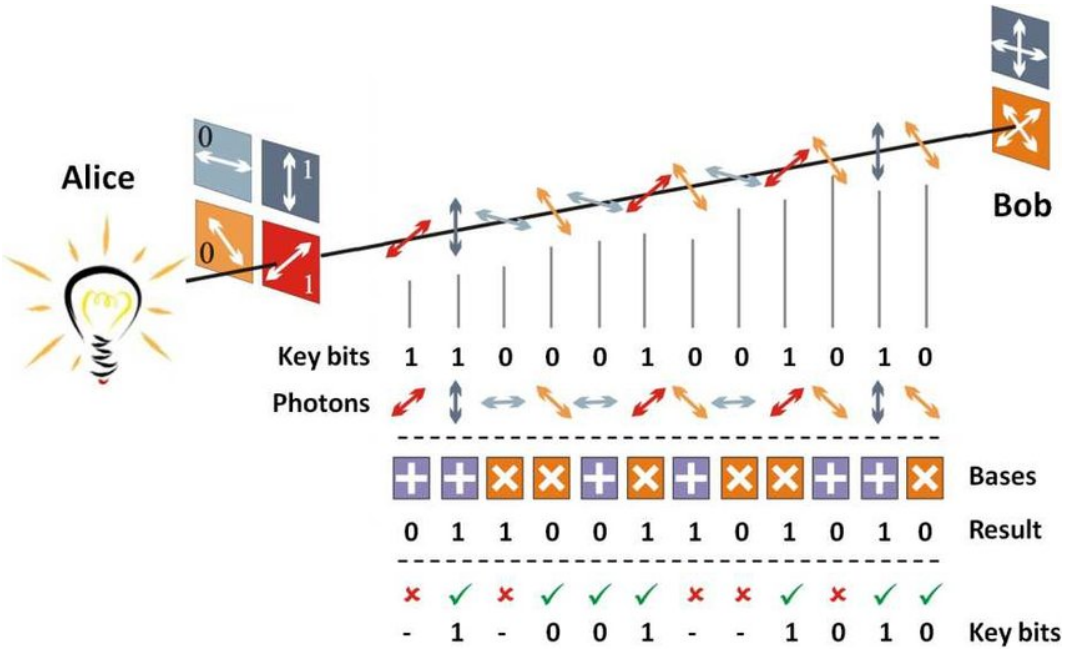

Fig. 1.11 BB84 protocol schematically represented [7]

In this way with this protocol Eve, a hypothetical interceptor, may only intercept the base sequence once is openly communicated in the public channel, nonetheless, the key remains still unknown. Let us consider the worst case: in which Eve tries to intercept every single photon in the sequence sent by Alice, measures the polarization state, and then re-transmits it to Bob without being noticed by him. Also, in this case, the original bases chosen by Alice for each photon are unknown to the receiver Eve, thus also Eve may statistically choose the right basis only half of the times. Moreover, as mentioned previously Eve will modify the polarization state of the transmitted photons by measuring them. This is the result of a fundamental characteristic of quantum mechanics: any measure which is not performed in a basis of which the measured state is an eigenstate will inevitably alter the measured state. Indeed, as the no-cloning theorem states: an unknown quantum state cannot be cloned. Hence, Eve's attack can be easily detected since Eve's presence leads to the change of the polarization of about half of the photons. Considering that Bob uses the same basis as Alice half of times, he will obtain as result there will be the 12.5% of incorrect bits. To find out the possible presence of Eve, Alice and Bob can compare part of the key through a classical channel, sacrificing a part of the key, and they can check the probability of incorrect bits received by Bob and therefore discover Eve's presence. The remaining part of the key can be safely used if the incorrect rate is

below 12.5%. Unfortunately, this method holds only if single photons are transmitted. Indeed if we use a standard pulsed laser instead of a single photon source, the key will be encoded into a multi-photon bunch, thus Eve may be able to measure the polarization state of one of them in the bunch without destroying the others. For this practical reason, a single photon source shall be mandatory for the implementation of this protocol. The opportunity of detecting attacks and the natural robustness given by the fundamental quantum mechanics laws set quantum cryptography as the ultimate protocol for secure data exchange. The Quantum Key Distribution approach was experimentally demonstrated using in 2002 by means of NV centers in nanodiamonds as single-photon sources [6].

1.4.2 Quantum Computing

As reported in the well-known Moore's law, in the last decades computers have grown their computation capability very fast by increasing the density of the basic computational element: the transistor. This miniaturization cannot continue forever, since dimensions will reach sizes where the quantum effects become more significant. Hence, it is necessary to define a new kind of computation: quantum computing. This concept is not so recent. Indeed in the 1982 [129], Feynman pointed out that a quantum computer was necessary in order to simulate quantum systems, whose properties are too complex for a classical computer.

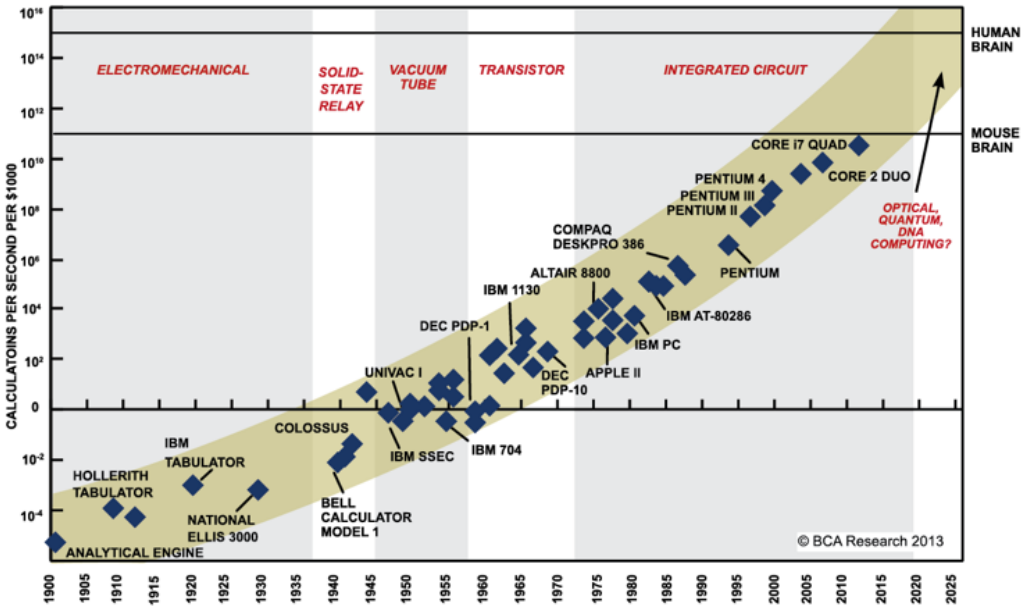

Fig. 1.12 Moore's law: empirical observation of the number of the transistor in different years [154].

As the classical computer has a fundamental unit called a bit (with binary values 0 and 1), the Quantum computers have as fundamental unit the quantum bit or *qubit*. Qubits are experimentally implemented as states of atoms [130–132], nuclei [133], photons, etc. Photons are very promising since they allow the opportunity to encode information in different degrees of freedom. Polarization-encoded systems are characterized by low decoherence and represent a simple way to realize single-qubit gates for quantum computing.

The most interesting thing is that a qubit has not binary values, but it can take infinite values. This is due to the quantum nature of the qubit that can be described as a superposition of basis states $|0\rangle$ and $|1\rangle$:

$$|\psi\rangle = \alpha\,|0\rangle + \beta\,|1\rangle \tag{1.20}$$

It is straightforward that due to the probabilistic nature of quantum mechanics, performing a measurement on the state $|\psi\rangle$ we will obtain a zero with the probability α^2, and the qubit will be in the state $|0\rangle$.

To help the visualization of the single qubits and operations on single qubits, the state $|\psi\rangle$ is usually represented geometrically as a point on a unit sphere called *Bloch sphere*.

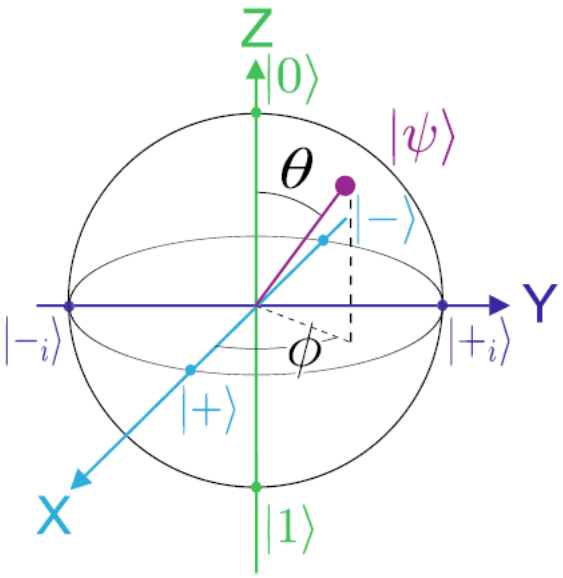

Fig. 1.13 Bloch sphere used for the visualization of qubits. The state $|\psi\rangle$ can be rewritten as a function of the polar angle θ and the azimuthal angle ϕ: $|\psi\rangle = \cos(\frac{\theta}{2})\,|0\rangle + e^{i\phi}\sin(\frac{\theta}{2})\,|1\rangle$. In the figure, it is also possible to observe the most frequently used states that lie on the axes of the Bloch sphere: on the x-axis $|+\rangle = \frac{1}{\sqrt{2}}(|0\rangle + |1\rangle)$ and $|-\rangle = \frac{1}{\sqrt{2}}(|0\rangle - |1\rangle)$, while on the y-axis $|+_i\rangle = \frac{1}{\sqrt{2}}(|0\rangle + i\,|1\rangle)$ and $|-_i\rangle = \frac{1}{\sqrt{2}}(|0\rangle - i\,|1\rangle)$

For example, the Hadamard gate H turns superposition states into basis states and vice versa and it can be observed on the Bloch sphere as a first π rotation about the z-axis followed by a $\pi/2$ rotation about the y-axis. This gate can be easily implemented with a beam splitter and it has the following matrix form:

$$H = \frac{1}{\sqrt{2}} \begin{pmatrix} 1 & 1 \\ 1 & -1 \end{pmatrix} \tag{1.21}$$

Two-qubit gates are theoretically necessary to perform universal quantum computing, but in 2001 it was reported that efficient quantum computing is possible by exploiting simply linear optics (beam splitters and phase shifters), detectors and *single-photon sources* [134]. So, it is clear that the key challenges are the development of low-loss scalable optical circuits, high-efficiency single-photon detectors, and *high-efficiency single-photon sources*.

1.4.3 Metrology

Single photon sources play a key role also in different fields, aside from the development of innovative quantum technologies, such as in Metrology [8–10] in particular in what concerns the definition of *Candela*. Indeed, in the International System (SI) the base unit for the luminous intensity is so-called *Candela* (cd) and it has been re-defined recently in 2019. Here we report the new definition from the SI website (Bureau International des Poids et Measures): *The candela is defined as the fixed numerical value of the luminous efficacy of monochromatic radiation of frequency* $540{\cdot}10^{12}$ *Hz,* K_{cd}*, to be 683 when expressed in the unit lm* W^{-1}*, which is equal to cd sr* W^{-1}*, or cd sr* kg^{-1} m^{-2} s^3*, where the kilogram, meter and second are defined in terms of h, c and* $\Delta\nu_{Cs}$.

Nonetheless, a photon-based definition would be more useful for the development of new optical communication technologies and devices even if this new definition is based on a constant value (K_{cd}). In this context, a so-called *Quantum Candela* would be more functional and it would be defined as the luminous intensity of a source that emits photons of frequency $540{\times}10^{12}$ Hz at a rate of $4.092{\cdot}10^{15}$ photons

s^{-1} sr^{-1} in a given direction. Where the required rate was determined by exploiting the following formula:

$$P = nh\nu \tag{1.22}$$

with

P= 1/683 W

n= photon rate (per second)

ν= 540×10^{12} Hz

h=6.62607015 × 10^{-34} J s

Chapter 2

Hyperbolic Metamaterials

Part of the work described in this chapter was also previously published in "Funneling Spontaneous Emission into Waveguides via Epsilon-Near-Zero Metamaterials." Nanomaterials 11.6 (2021) by Channab, M., et al.

In the previous Chapter, we have analyzed the single-photon source properties and applications. In particular, it is worth to notice that the SPSs play a key role in quantum technologies even if they have different limitations such as low emission rate, collection efficiency, and broadband emission. In this Thesis, we propose the use of Hyperbolic Metamaterials in order to overcome such SPS limitations by exploiting their extraordinary optical properties. In this way, it would be possible to develop innovative SPS-based quantum technologies. In this chapter, we will discuss briefly the main properties related to Hyperbolic Metamaterials, focusing on their exotic optical response.

2.1 Hyperbolic Metamaterials

There are different definitions of the word *Metamaterial* since a few kinds of metamaterials exist, indeed *Metamaterials* (MM) have been deeply applied in different fields such as telecommunications[158], construction engineering [159, 160], particularly for anti-earthquake technologies, and photonics [161–163]. Here we report the most general definition:

"A metamaterial is an artificial material with characteristics that go beyond the natural properties we can find in nature and often characterized by periodical geometrical patterns or combinations."

The MMs show interesting properties in several wave phenomena. In MMs, the unit cell has dimensions much smaller than the wavelength range in which the MMs are applied ($d << \lambda$), in this way the incident waves perceive the MM as a homogeneous medium. Hence, it is straightforward that MMs have been seen with huge interest since they can be exploited very easily for different wave phenomena.

In this Thesis, we focus our attention on the *Hyperbolic Metamaterials* (HMM). They have been studied in nanophotonics in the last years since they show incredible optical properties such as negative refractive index [161], ε and μ near zero [162], and light trapping [163]. These properties can enable the implementation of innovative sensing, imaging, and quantum devices (e.g hyperlens) [42–45]. HMMs' extraordinary features come from their electrical permittivity anisotropy introduced by the presence of two materials: a metal and a dielectric one ordered in nanometric periodic structures such as multilayer, metal nanorods in dielectric matrix and lamellae, see Fig 2.1.

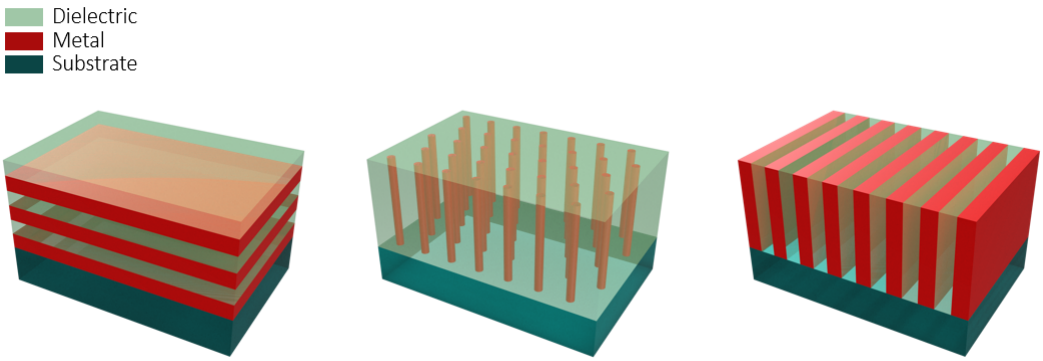

Fig. 2.1 Different kinds of hyperbolic metamaterials

They are called *hyperbolic* due to their isofrequency surface shape that is related to the strong electrical permittivity anisotropy as can be observed from the following equations for a lamellar structure and in Fig 2.2:

$$\rho = \frac{t_m}{t_m + t_d} \tag{2.1}$$

$$\varepsilon_y = \varepsilon_z = \rho\varepsilon_m + (1-\rho)\varepsilon_d \tag{2.2}$$

$$\varepsilon_x = \left(\frac{\rho}{\varepsilon_m} + \frac{1-\rho}{\varepsilon_d}\right)^{-1} \tag{2.3}$$

$$\varepsilon = \begin{bmatrix} \varepsilon_x & 0 & 0 \\ 0 & \varepsilon_y & 0 \\ 0 & 0 & \varepsilon_z \end{bmatrix} \tag{2.4}$$

$$\frac{k_z^2 + k_y^2}{k_0^2} \cdot \frac{1}{\varepsilon_x} + \left(\frac{k_x}{k_0}\right)^2 \cdot \frac{1}{\varepsilon_z} = 1 \tag{2.5}$$

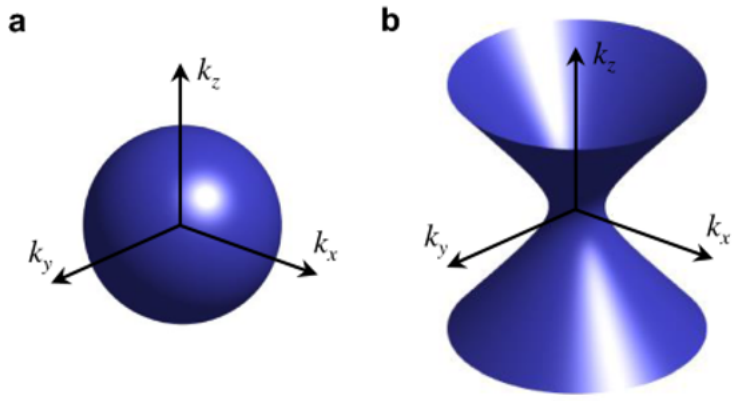

Fig. 2.2 Isofrequency surface shape related to an isotropic medium (**a**) and to the HMM dispersion relation reported in eq. 2.5 (**b**) [155].

Where ρ is the metal fill factor, t_i is the thickness of the material in the unitary cell with t_m and t_d referred to the metal and dielectric materials and k_i and ε_i are the wavevector and electric permittivity components in the reported tensor of the effective medium. In the chosen Cartesian coordinate system, the X-axis corresponds to the anisotropy axis in the lamellar structure and the Z-axis and Y-axis determine the plane where the permittivity components are isotropic. For simplicity, here we have considered the HMM a homogeneous medium by means of the effective medium approximation (EMA), see Eq.2.2 and Eq. 2.3. Indeed, the theoretical description is one of the difficulties related to these systems. It is worth to notice that in the EMA the permittivity components follow equations that depend on the structure under investigation (metal nanorods, multilayers, etc...) and on the chosen coordinate system [43].

If we now consider Fig 2.2 and Eq. 2.5, we can observe that the curvature of the isofrequency surfaces is determined by the effective permittivity values. Their particular anisotropy in the optical behavior enables spontaneous emission properties such as emission enhancement and control over the emission directivity and spectrum of photon sources coupled with the HMM. These appealing characteristics make this kind of metamaterials very interesting as a platform for the development of a new generation of photonic devices based on single-photon sources (SPSs), especially for what concern quantum communication and quantum computing, as previously mentioned. The HMM properties open up the opportunity to overcome the SPS limi-

tations [1, 18] previously mentioned such as the NV low emission rate and broadband emission spectrum. Therefore, by exploiting the above-mentioned properties, it is theoretically possible to increase the emitter intensity by enhancing the spontaneous emission and tuning the directivity of a specific emission wavelength only controlling the geometrical parameters of the HMM (e.g. period of the periodic structure, fill factor, etc...) in order to strongly increase the computational capability of photonic devices. In the next sections, we will focus on the HMM theoretical description (EMA), enhanced spontaneous emission, and directional emission properties.

2.1.1 Effective Medium Approximation: properties and limits

Due to the anisotropic and subwavelength nature of HMMs, they are generally described exploiting the effective medium approximation in order to simplify the estimation of their optical behavior (e.g. transmission and reflection spectra). In this kind of description, as reported in the previous section, the metamaterial is observed and considered as a homogeneous medium with averaged permittivity values (see Eq. 2.1-2.5) along the directions perpendicular and tangential to the optical axis [50, 51]. The EMA is quite straightforward for multilayer, lamellar, and nanowire structures but unfortunately, there are several limitations and considerations to take into account. Indeed, for instance, if we study a multilayer HMM the EMA model does not take into account the single layer (metal or dielectric) dimensions but only their ratio. Regarding this limitation, Kidwai et al. [50, 51] have demonstrated that the distance between the photon source (a dipole) and HMM and the thickness of the layers are fundamental parameters for optical response estimation. In particular, they have demonstrated that conditions for the applicability of the EMA can be related to the thickness of the metal layer (d_m), the dielectric layer (d_d) in the HMM and to the distance h between the emitter and the HMM surface:

$$\frac{d_m + d_d}{h} < \frac{1}{5.32} Re\left(ln\left(2\frac{(\varepsilon_m - \varepsilon_m)^2 - 4\varepsilon_m\varepsilon_d}{(\varepsilon_m + \varepsilon_m)^2} \right) \right) \tag{2.6}$$

They have also shown how the averaged thickness determines firstly the cutoff wavenumber for large-k modes sustained by the HMM ($k_{cutoff} \propto d^{-1}$) [52, 53, 57]. It is clear that there are several physical limitations on the dimension of fabricated

nanostructures that leads to a finite LDOS, despite the traditional EMA approach suggesting a medium that has an infinite LDOS.

Moreover, in this approximation non-local effects can be considered in order to describe the finite number of available optical states and quantum optical processes that can occur inside an HMM. It has been demonstrated that such non-local effects can occur inside HMM [136]. A physical system is considered non-local when at a given point its behavior depends on its state in another spatially separated region. The traditional EMA does not consider non-locality and it becomes invalid especially when the losses in the metal are moderate. It was reported in different works that by introducing non-locality in the theoretical description additional propagating modes emerge inside the HMM [58, 59]. In particular, the manifestation of these modes is related to the impact of the non-locality on the LDOS topology that affects quantum processes such as spontaneous decay and spectral response. The non-locality introduces a degree of freedom that is not present in the local EMA: the optical response does depend on the dimension of the unit cell and can be engineered by scaling the unit cell enabling the opportunity to design devices with higher performances.

2.1.2 Enhanced Spontaneous Emission

Regarding the spontaneous emission enhancement, it has been shown empirically and mathematically [46–49] that the hyperbolic isofrequency surface leads directly to an increase in the local density of optical states (LDOS). By increasing the LDOS, there is an increase in the number of radiative decay channels available for large-k states manifesting an enhanced spontaneous emission as stated by the Fermi golden rule. These states would be otherwise evanescent in isotropic materials.

Here we report the Fermi's golden rule that describes the transition rate for a radiative channel and the photons states:

$$\Gamma = \frac{1}{\tau} = \frac{2\pi}{h} \sum_{k,\sigma} \langle f | H_{int}(k,\sigma) | i \rangle^2 \, \delta(h\omega_{k,\sigma} - h\omega) \tag{2.7}$$

$$\rho_{\sigma}(\omega) = \sum_{k} \delta(h\omega_{k,\sigma} - h\omega) \tag{2.8}$$

Where τ is the lifetime, ω is the energy of the emitted photon with k wavenumber and polarization σ, $\langle f|H_{int}(k,\sigma)|i\rangle$ is the matrix element of the transition that leads from the initial state $|i\rangle$ to the final state $\langle f|$ with a transition energy hω and $\rho_\sigma(\omega)$ is the density of states.

The HMMs can affect the spontaneous emission and consequently the decay rate by introducing lifetime decreasing. This is straightforward since the radiative decay rate and LDOS are directly proportional, see Eq. 2.8 and Eq. 2.9. Moreover, considering the different contributions (radiative channels, surface plasmon polaritons, and high-k modes), it is known that the contribution of the high-k modes becomes dominant in the near field [60]. We have to take into account also the non-radiative channels too. In fact, by decreasing the distance between the source and the HMM surface there is an increase in the quenching effect that occurs in the metal layer in the HMM. This leads to a lifetime reduction but with no photon emission. Furthermore, since the emission enhancement is related to the coupling between the evanescent waves in the near field emitted by the source and the large-k modes in the HMM, the enhancement will be stronger when the source is closer to the surface [50, 51, 56]. This effect and the supported large-k modes are the main ones responsible for the emission enhancement also called the Purcell effect [139]. This effect can be estimated with a parameter called the Purcell factor that is always overestimated considering the HMM described with EMA with respect to the actual metamaterial [54, 55]. Here we report the general definition of this parameter:

$$F_P = \frac{\Gamma_{HMM}}{\Gamma_0} \tag{2.9}$$

Where Γ_0 is the spontaneous emission rate when the emitter is in free space and Γ_{HMM} in the case the emitter interacts with an HMM.

2.1.3 Directional emission

For what concerns the control of the directivity of the emission, in classical materials we have an isofrequency surface that is spherical. In this case, we obtain isotropic emissions considering the fact that the Poynting vectors are always perpendicular to this surface. Instead, with a hyperbolic surface, we will obtain Poynting vectors that lie in an emission cone with a specific angle of aperture that depends on the curvature of the surface and therefore on the permittivity values with this relation:

$$tan(\theta) = \sqrt{\frac{\varepsilon_y}{\varepsilon_x}} \tag{2.10}$$

In addition, it is reported in the literature [61] that the emission directivity can be tuned only by manipulating the metal fill factor in the HMM metasurface obtaining perpendicular and horizontal emissions, a feature that is crucial for the communication and elaboration of data transmitted as photons. In particular, a directional emission can be reached for a source in the proximity to the HMM surface when the Epsilon Near Zero (ENZ) conditions are achieved [61]. Indeed, it is possible to tune the *curvature* of the isofrequency surface by controlling the values of the effective permittivity. For example, we now consider a multilayer structure and we report the necessary conditions to achieve horizontal emission:

$$Re|\varepsilon_y(\rho)| \approx 0 \ \cap \ |\varepsilon_y(\rho)| = o(\varepsilon_x(\rho)) \tag{2.11}$$

This condition has to be considered for one single wavelength value. By obtaining the horizontal emission a high effective photon extraction is achievable as we have demonstrated [62]. In that paper, we have shown how a system composed of an in-plane waveguide and a multilayer (Au/Al_2O_x) could be used for different applications for which there is a need for higher photon rate. With the previous conditions we have achieved the horizontal emission in the multilayer structure and coupled the emission with the in-plane waveguide as can be observed in the following figures:

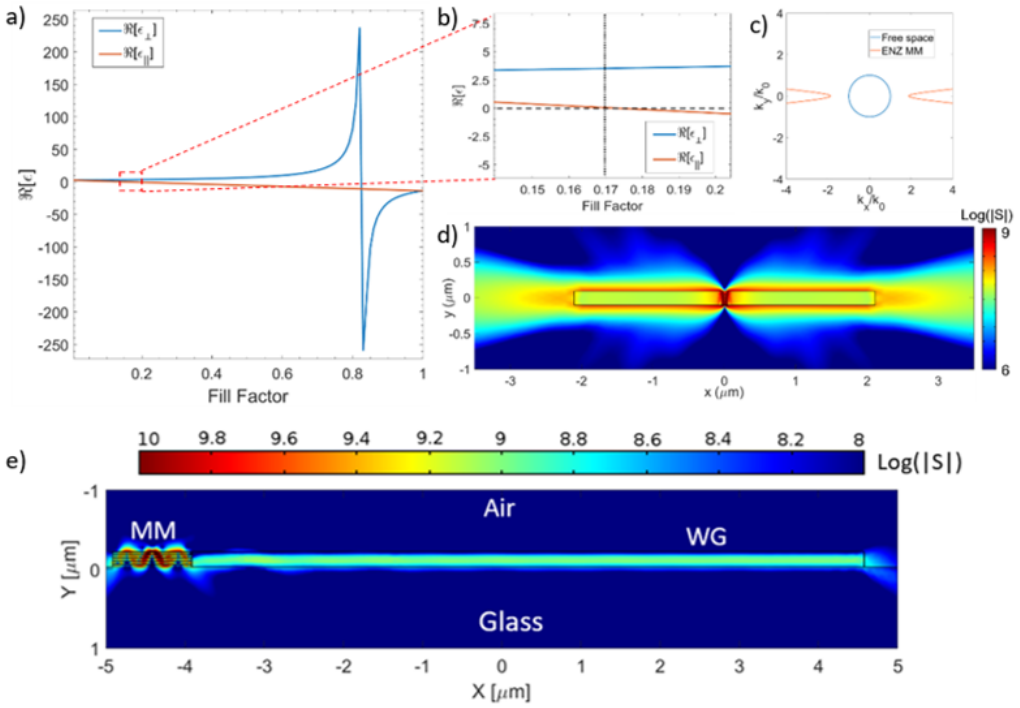

Fig. 2.3 Here we report: (a) the real part of the permittivity components dependence on the metal fill factor used in the EMA, (b) the magnification of the reddotted region highlighted in Fig 2.3a, showing the region in which the ENZ value is expected, (c) isofrequency curves for the air (blue circle) and the ENZ metamaterial (red line), (d) magnitude of the Poynting vector plotted for the EMA at = 637 nm for the fill factor found in Fig 2.3b, (e) magnitude of the Poynting vector at 637 nm for a 1 μm long HMM coupled with the waveguide. It is worth to notice that in this case, we have used the actual HMM with $\rho = 0.17$ since it is characterized by the same directional emission of the effective medium.

In particular, it has been demonstrated that the ratio of the total emitted and outgoing power depends exponentially on the lateral length of the multilayer structure. More importantly, by considering the ratio between the outgoing power and the total emitted by the source in a whole domain of air they report values of 1414% for a 150 nm long metamaterial at 630 nm and 377 % for a 500 nm long one at 632 nm, see Fig 2.4:

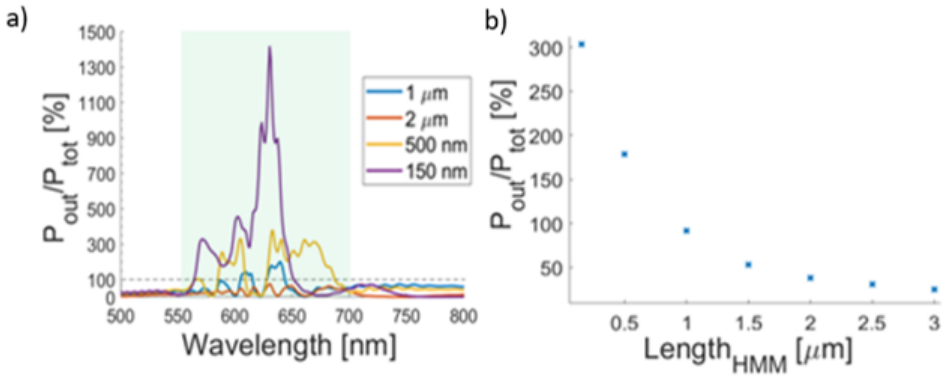

Fig. 2.4 a: ratio between the power emitted by a dipole in air and the outgoing power when it is coupled with the HMM for different HMM lengths. Fig 2.4b: integrated values in the highlighted region in Fig 2.4a for different HMM lengths

This effect could be explained by the fact that by reducing the lateral dimension it is possible to access sustained modes that have short propagation lengths.

It is worth to notice that the directional emission and the spontaneous emission enhancement properties do not depend on the kind of photon source and on the temperature. Hence, HMM can be in principle exploited as a platform for several photon sources not only for room temperature SPSs such as NV centers.

Chapter 3

Self-assembling Block Copolymers

As mentioned in the previous Chapter, the HMMs are characterized by dimensions that are sub-wavelength with respect to the wavelengths of interest, i.e. visible range in this Thesis. To produce HMMs with these dimensions several techniques have been used such as electron-beam lithography, photolithography, and ion-beam etching [63–67]. These top-down lithographic processes are usually very time-consuming and not cost-effective when precise control over a large area is needed at the nanoscale, particularly in terms of shapes and sizes that are below 100 nm. Material deposition techniques have been also suggested and used as a simple and direct way to fabricate multilayers. Unfortunately, this kind of HMMs has a limited Purcell enhancement due to the non-radiative nature of the dominating plasmonic modes [128, 141, 142]. By means of a lithographic process, an outcoupling grating is a possible way to overcome this drawback and extract energy from the non-radiative plasmonic modes but only for specific wavelengths. For these reasons, we propose the use of the so-called Self-assembling Block Copolymer (BCP) as an innovative and low-cost technique that enables the opportunity to pattern large area in a short amount of time. In this Thesis, we have focused our attention, particularly on the fabrication of lamellae perpendicular oriented with respect to the substrate since this structure is characterized by an in-plane optical axis that is fundamental for photon extraction [89]. Furthermore, BCPs can be synthesized with low-cost processes that are already available at an industrial scale. We will discuss the self-assembly process of BCPs used for this Thesis with more details in the Methodologies' section dedicated to the fabrication steps. In this Chapter we will analyze their main properties, focusing

on applications and on fabrication techniques that are available nowadays for their self-assembly.

3.0.1 Block Copolymers

In order to understand the BCPs, we first consider their molecular structure which is composed of macromolecules called polymers that are formed by repeated monomers: sub-units linked via covalent bonds. In particular, a repetition of only one monomer sub-unit is called a homopolymer. BCPs are formed by two or more immiscible homopolymers (i.e. A and B) chains linked by a covalent bond, for example with the repetition structure of di-block Copolymer A-A-A-B-B-B. In figure 3.1 some of the most common configurations are reported:

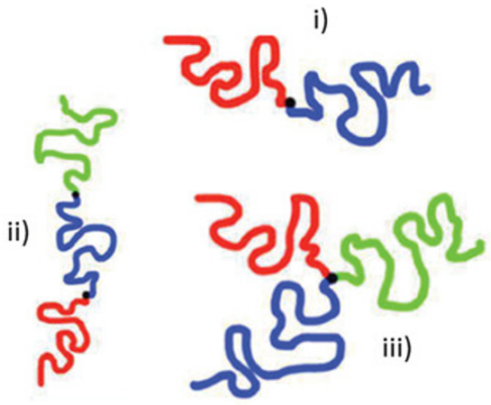

Fig. 3.1 Different BCP configurations: (i) diblock, (ii) triblock, and (iii) miktoarm star BCPs [68]

The most interesting feature of BCPs is their capability to organize themselves in periodic nanostructures when subjected to an annealing process, the above-mentioned self-assembly. By exploiting this characteristic self-assembly, several nanostructured metamaterials have been fabricated [68–70, 80–85]. The nanostructured patterns have typical sub-50 nm dimensions. This is due to the length scales of the separation that is limited by the polymer chain length. The microphase separation depends mainly on three parameters: the fraction of each homopolymer (f_A and f_B), the Flory–Huggins parameter (χ) that is the interaction parameter between the homopolymers, and the number of monomeric sub-units (N=N_A+N_B) [86–88]. During phase segregation, enthalpy and entropy changes occur. The first one is strongly

related to the parameter χ while the second one is to the number of sub-units also referred to as the degree of polymerization. Hence in the equilibrium phase diagram, the phase behavior can be described using the product $\chi_{AB}N$ and the volume fraction f_A for example, as reported in Fig. 3.2:

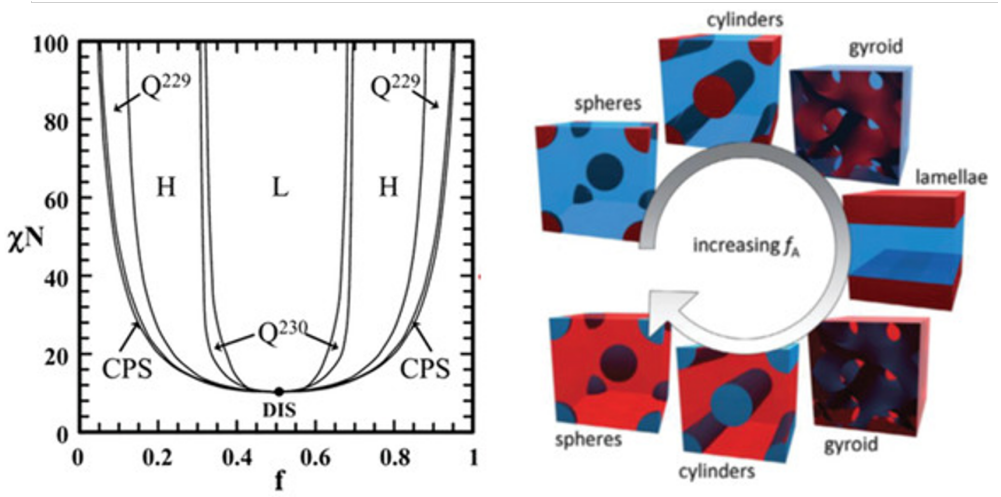

Fig. 3.2 Theoretical phase diagram of a diblock BCP [68] on the left and the possible corresponding morphologies [69] on the right

Moreover, it is also clear from the figure above that the volume fraction can determine the final nanostructure too. Increasing the volume fraction f_A different morphologies can be obtained such as gyroids, cylinders, spheres, and lamellae.

3.0.2 BCP applications

In nanotechnology, the fabrication processes have different critical steps: one of them is surely the transfer of nanopatterns into inorganic materials. In order to overcome these critical points, chemical and physical techniques have been deeply developed related to the BCPs such as different block polymer degradation [90, 91] and selective etching resistance [92]. This is possible since BCPs can be directly converted into fully inorganic structures by simply eliminating one of the polymeric phases [93, 94] and transferring the pattern on an inorganic substrate by etching. Moreover, block-selective vapor and liquid phase infiltration methods have been studied in order to replace one of the two BCP phases with metals or metal oxides because of their functional features [95–98] or further pattern transfers [99–104].

In optics, BCPs have been widely used in particular for what concerns plasmonic sensors, photonic devices, and broadband antireflection applications, see Fig 3.3.

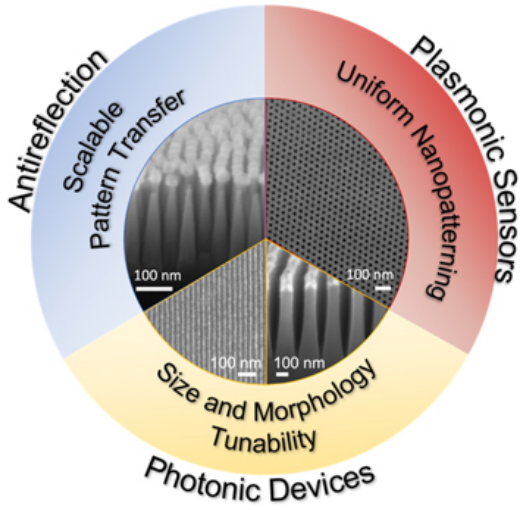

Fig. 3.3 Notable characteristics of BCP thin film nanopatterned structures and their potential areas of nanophotonic applications [70]

If we consider the plasmonic sensors, based on the coupling between photons and collective motions of the conduction electrons in a metal surface (i.e. plasmons), BCPs have been used mainly for the development of nanostructured substrates for SERS (Surface Enhanced Raman Scattering) applications [105, 106]. These applications have received attention since it is possible to tailor the plasmonic resonance wavelength by tuning the size of metallic nanostructures and changing the refractive index and size of the dielectric gap material. Indeed at wavelengths in which the plasmonic resonance occurs, a large scattering cross-section and enhanced absorption appear. When metallic nanostructures are separated by a dielectric thin gap, there is a strong enhancement of the electric field in the gaps. BCPs have been usually used in order to obtain an initial pattern, often cylinders with controlled spacing and diameter, and afterward a plasmonic metal is deposited onto or into the pattern. Typically the final pattern is composed of arrays of metal nanoparticles, i.e. Au, with tailored optical response in the visible range, suitable for biosensing applications, see Fig 3.4a-c.

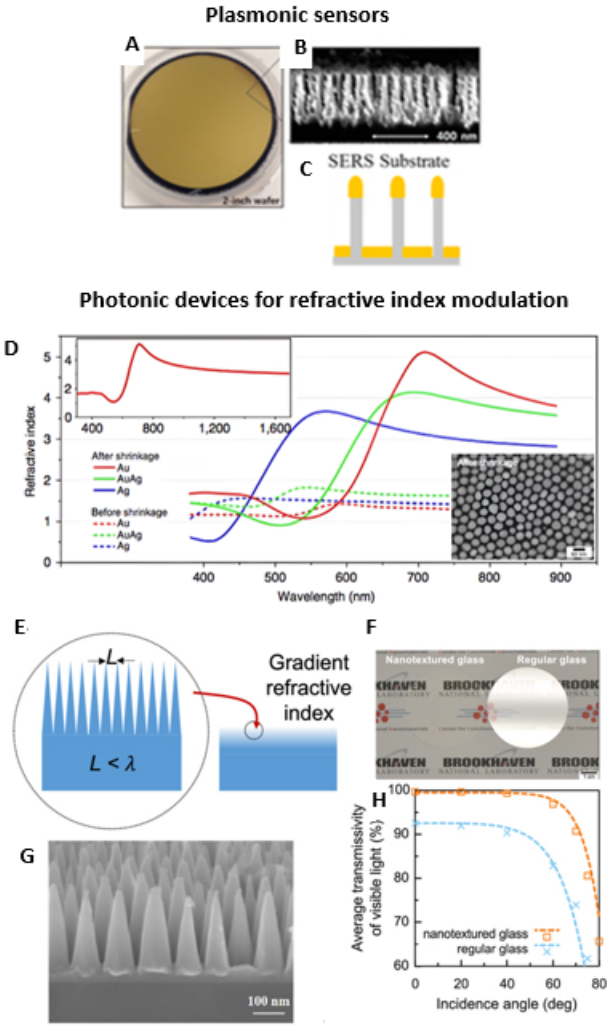

Fig. 3.4 Substrates fabricated via BCP self-assembly for different applications. (A) Picture of a 2-inch wafer-scale with nanopillars for SERS applications. (B) Cross-sectional SEM image and (C) schematic of the nanopillars[71]. (D) Refractive indices for Au, Ag, and Au–Ag alloy nanoparticle arrays obtained through BCP thin films. The inset shows the SEM image of Au nanoparticles array [72]. (E) Schematic of an effective gradient refractive index obtained through BCP self-assembly. (F) TiO_2 nanocones (top) SEM image and (bottom) their measured reflectance, reproduced from [74], with the permission of AIP Publishing, (G) Picture comparing nanostructured glass to untreated glass. (H) Experimental and simulated transmissivity for both nanostructured and untreated glass, reproduced from [74], with the permission of AIP Publishing

For what concerns photonic devices, BCPs are introduced in order to produce metasurfaces to obtain refractive index modulation and polarization-dependent optical response. Regarding the refractive index tuning, it has been demonstrated that is

possible to obtain metamaterial refractive index values that are tunable from 1.43 to 5.10 by embedding metal nanoparticles into shrinkage films fabricated through BCP assembly [107], see Fig 3.4d. This is simply obtained by tuning the gap between metal nanoparticles by controlling the BCP film shrinkage. Moreover, by controlling the refractive index it is also possible to tune broadband antireflection properties. Usually, surfaces are coated with a material whose refractive index has intermediate values between the surface of interest and the surrounding material. In this case, BCPs have been exploited for their ability to form thin films with highly tuned porosity by removing selectively one copolymer phase in order to obtain low refractive index antireflection coating that is ideal for glass, see Fig 3.4e-h.

Finally, considering the polarization-dependent optical response, alternating BCP films have been used to fabricate polarizers, in particular as masks for reactive ion etching to obtain Si wires. In this wire-grid polarizers [108, 109], wavelengths that are larger than the nanostructure period show a polarization dependence in the optical response, indeed light polarized orthogonally to the wires will be transmitted while in the opposite case will be reflected.

3.0.3 BCP Self-Assembly Techniques

In this section, we discuss the different annealing techniques that enable self-assembly in BCPs. The self-assembly is enabled when the glass transition temperature is reached since this gives enough energy to the polymer chains to assemble in ordered structures. Therefore annealing techniques are required. In particular, we analyze solvent vapor annealing, thermal annealing and finally laser annealing.

- **Solvent Vapor Annealing**

  One of the most exploited methodologies for the self-assembly of thin BCP films it is the Solvent Vapor Annealing process (SVA). This is due to the fact that there is a wide range of solvent or solvent mixtures that can be used to order BCPs with different chemical compositions and morphologies such as gyroids, cylinders and lamellae [110–112]. Moreover, this process usually represents the starting method to study how to induce the BCP self-assembly, since it can be implemented with low-price equipment. Indeed, the simplest way to implement this technique is a closed chamber in which the liquid solvent can evaporate spontaneously or with thermostated annealing. While in advanced SVA setups, the chamber can be equipped with a flow regulator to introduce the solvent vapor and control the solvent saturation.

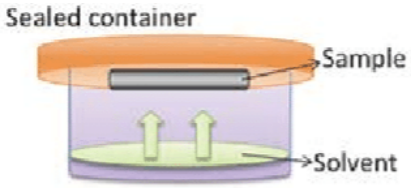

Fig. 3.5 Typical SVA setup [76]

Another important feature of this process is related to polymer chain dynamics. When the solvent vapor is present the BCP chain dynamics increases drastically and this leads to the ordered nanostructures not only in low molecular weight BCPs but also for ultrahigh molecular ones. These BCPs are very interesting for plasmonics and dielectric metamaterials, since they can form larger periodical nanostructures ($\approx$ *100 nm*) with respect to the low molecular weight BCPs [113–115]. Unfortunately, these kinds of BCPs are very challenging because of their slow kinetics.

- **Thermal Annealing**

  The thermal annealing process is a more direct method to reach locally the glass transition temperature and so to give the necessary energy to the polymer chains to order themselves in nanostructures [120, 121]. For this reason, this technique can require less time with respect to the SVA which can last from hours to days. This technique is usually performed in a closed space where the temperature is uniform such as a hotplate or in a vacuum oven. Hence, in this case, its main drawback is related to small-area scalability. A method to overcome this limitation can be represented by the *zone annealing*. In this process, the sample overcomes the glass transition temperature [116, 117] locally through a filament that is heated and scanned across the sample [118, 119].

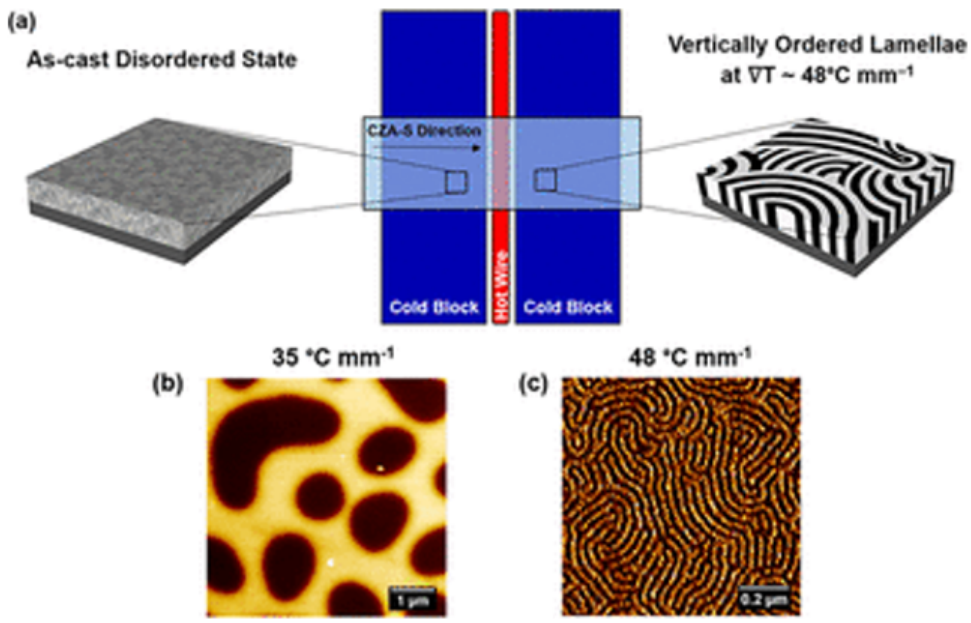

Fig. 3.6 (a) Schematic of the zone annealing process for the self-assembly of BCPs. (b, c) AFM images of nanostructures obtained at different temperature gradients [77]

In this way, this self-assembly process can be exploited more widely with roll-to-roll technologies [75] for continuous large-area manufacturing.

- **Laser Annealing**

Laser annealing is widely exploited as Direct Self Assembly (DSA) technique. In this case, the temperature necessary for the activation of the DSA is achieved by a photothermal process [122–124]. In this process the energy transported by the photons is converted into thermal energy, enabling ultra-fast and high-temperature annealing in selected areas obtaining highly order nanostructures. Indeed, it is worth to notice that laser annealing has a superior spatial control with respect to the other self-assembly techniques, i.e. zone thermal annealing [125, 126], even if the laser annealing technique seems very similar. Here we report the setup used for the standard laser annealing method:

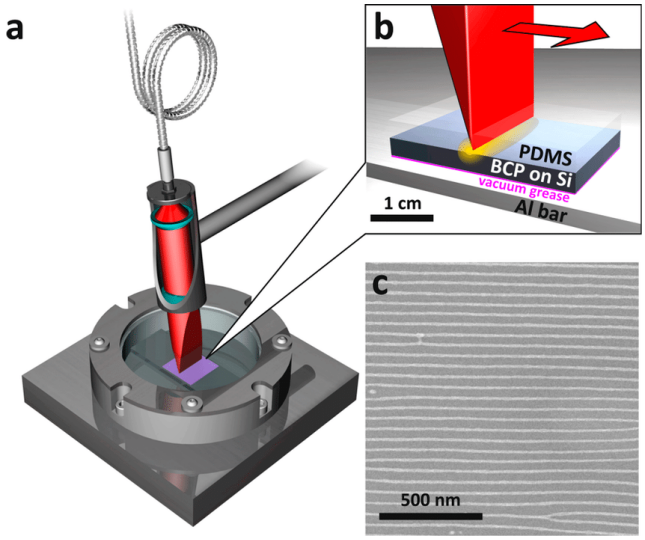

Fig. 3.7 Compact laser annealing setup. (a) The laser beam is focused onto a sample inside a vacuum chamber mounted on a translation stage. (b) Zoom of the ongoing process on the sample. (c) Ordered nanowires after the process [78]

Despite the above-mentioned advantages, the laser annealing method shows a significant drawback: due to the small size of the linear or elliptical laser beam that is focused on the sample the DSA in a large area is critical. Recently, an innovative approach has been proposed [79]. In this new method, the photothermal process is enabled by a flashlight of milliseconds in length. The light does not come from a laser, but from a lamp as reported in Fig 3.8:

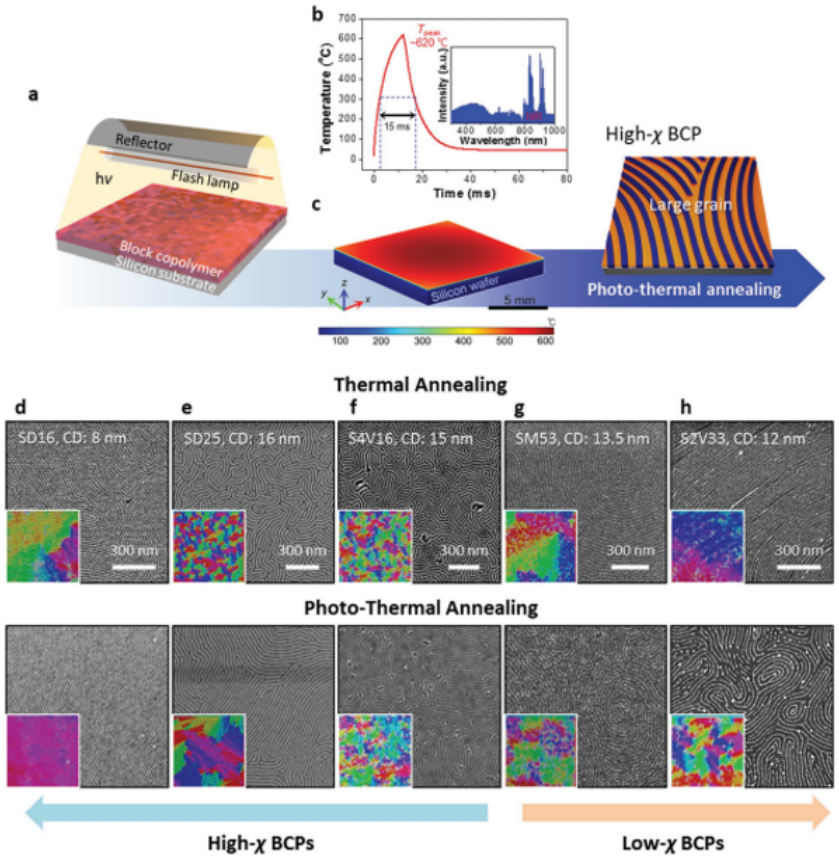

Fig. 3.8 (a) Flash lamp annealing (FLA) setup for BCP self-assembly, (b,c) Estimated temperature profile and distribution during FLA. The inset of (b) shows the wavelength distribution of the used lamp. (d-h) Self-assembled morphologies of high- BCPs comparison between conventional thermal annealing and FLA [79]

We can also notice that the light is reflected by a reflector introducing a large illuminated area. This feature may overcome the main laser annealing limitation, allowing its use at an industrial scale. More importantly, this technique has great efficiency when applied to high-χ BCP that are usually affected by slow self-assembly kinetics and hence they require a longer time scale for standard thermal DSA processes.

Chapter 4

Methodologies and Experimental Setups

Part of the work described in this chapter was also previously published in "Hyperbolic metamaterials via hierarchical block copolymer nanostructures." Advanced Optical Materials 9.7 (2021) by Murataj, Irdi, et al.

In this chapter, we will describe the methodologies used for the preliminary analysis of the proposed HMM lamellar structure (i.e. lamellae made of air and gold) and the experimental setups exploited for their fabrication and optical characterization. This chapter is formed by three sections: simulations' methodology, fabrication processes and instruments, and optical characterization setups.

4.1 Simulations' Methodology

Since we want to couple the HMM structure to a well-known SPS such as NV centers in diamond, first we have estimated the optical response, i.e. Purcell factor values and sustained modes, in the NV center emission's wavelength range by means of simulations. For this reason, we have performed different simulations with the software *Comsol Multiphysics 5.2*. This software exploits the Finite Element Method (FEM). In particular, we have designed a 2D asymmetric geometry model with a semi-circumference of 10 μm as a domain to calculate the electromagnetic field distribution and the radiated power of a photon source in the proximity of our

lamellar HMM metasurface with a frequency domain analysis. In the model, the photon source was a vertically oriented dipole introduced with a pseudo magnetic current of $8{\cdot}10^{-8}$ V flowing in a point at the desired height for the dipole, see Fig 3.1. Moreover, we have estimated the radiated power by the dipole integrating the Poynting vector along a square of 5 nm lateral size with the flowing magnetic current at its center, see Fig 4.1. We have used the radiated power by the dipole to estimate the Purcell factor as the ratio between the total emitted power by the dipole when coupled to the HMM (P_{HMM}) and when placed in an air domain (P_0) for every wavelength:

$$F_P = \frac{P_{HMM}}{P_0} \tag{4.1}$$

In this way, we consider for simplicity that every possible transition can be modelled with a monochromatic dipole. Here we report the geometrical configuration used for the simulations:

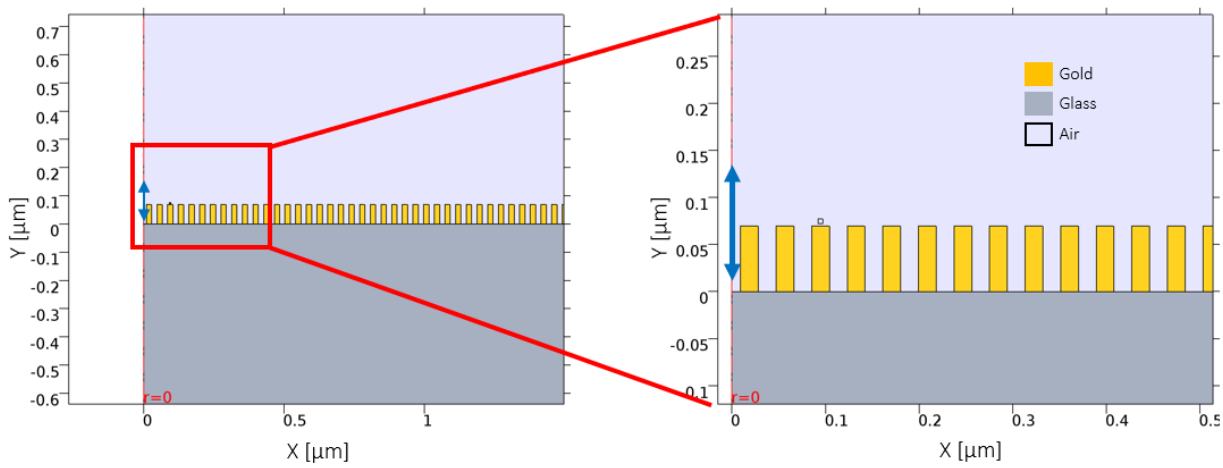

Fig. 4.1 In this figure we can observe the geometrical configuration used for the simulations: gold lamellae of 19 nm lateral size on a glass substrate with an upper domain of air. It is worth to notice that the dipole (the blue arrow) is in the center of the geometry with the height of the point in which the pseudo magnetic current flows. This point is placed in the center of the small square that can be seen above one of the lamellae.

In all our simulations the metasurface was composed by gold lamellae on a glass substrate alternated with air gap of the same lateral dimension that was set at 19 nm. In this way, we obtain a metasurface of air/gold lamellae where air acts as a dielectric

in order to obtain our hyperbolic metasurface. Furthermore, the refractive indexes used for air and glass were 1 and 1.45 respectively, while for the gold lamellae we have estimated the refractive index of a 20 nm thick layer deposited on a silica substrate with a J.A. Wollam ellipsometer (Fig 4.2).

We report the measured refractive index of the gold in Fig 4.3:

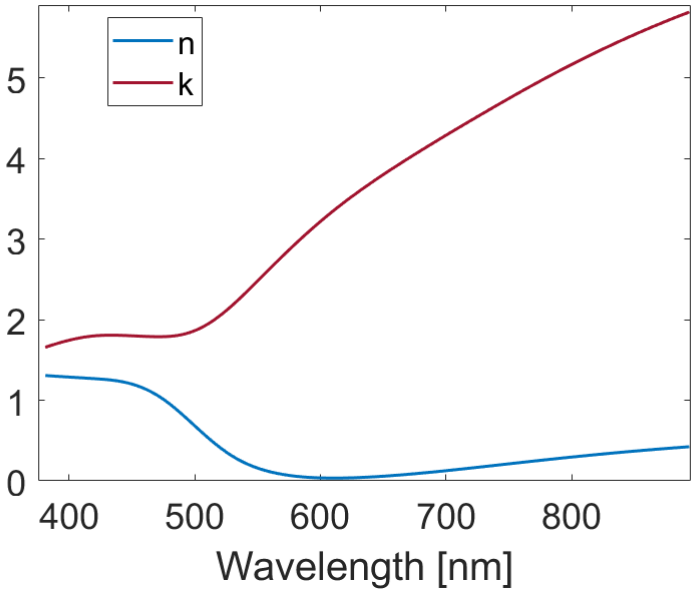

Fig. 4.2 Measured refractive index of 20 nm thick Au layer deposited on a silica substrate: real part reported with the blue line and the imaginary part with the red line.

Fig. 4.3 J.A. Wollam alpha-SE model

With the designed geometry in the simulations, we have performed a dipole frequency sweep between 500 nm and 800 nm in order to estimate the Purcell factor at different lamellae heights and different dipole distances from the metasurface. This has been done to determine the best height for the proposed metasurface and then to estimate the optimal coupling between the dipole and the HMM structure by tuning the dipole distance from the surface. Moreover, we have also performed modal analysis by implementing in Comsol the quasi-normal mode formalism described in [164]. The results of this preliminary study will be presented in the following Chapters.

4.2 Samples Fabrication

In this section, we will discuss the necessary steps for the fabrication of the hyperbolic metasurface made of air/gold lamellae. In particular, we have fabricated two kinds of samples: uniform samples with a height gradient, and samples with dewetted droplets.

4.2.1 Uniform samples with a height gradient

First, for these samples, we have performed a substrate neutralization. The substrate was glass and it has been neutralized by a grafting process of α-hydroxy ω-Br polystyrene-stat-polymethyl methacrylate (PS-stat-PMMA) random copolymer (RCP) (14.60 kg mol^{-1}), with styrene fraction (f) of 0.59 and a polydispersity index D = 1.30. The PS for the RCP was synthesized by activators regenerated by electron transfer-atom transfer radical polymerization (ARGET-ATRP), catalyzed by copper (II) bromide ($CuBr_2$) complexed by tris (2-(dimethylamino) ethyl) amine (Me_6TREN) ligand and initiated by tertbutyl α bromoisobutyrate in the presence of tin (II) 2-ethylhexanoate (Sn $(EH)_2$) as the reducing agent. All these substances have been purchased from Sigma-Aldrich. The molar ratios between the monomer, initiator, $CuBr_2$, Me_6TREN, and Sn $(EH)_2$ were 100/1/0.02/0.22/0.2. The polymerization reaction have been conducted for 2 h at 90 °C. The obtained PS was characterized by M_n = 3.1 kg/mol and D = 1.09. For the synthesis of the PMMA for the RCP we have used the same initiator, catalyst, and reducing agent of the PS synthesis employed for the ARGET-ATRP. In this case, the ligand was TPMA and

the molar ratios between the monomer, initiator, $CuBr_2$, TPMA, and Sn $(EH)_2$ were 30/1/0.04/0.24/0.2. Polymerization reactions have been conducted for 45 min at 70°C. The obtained PMMA was characterized by Mn = 3.9 kg/mol and D = 1.18.

To neutralize the substrate, the first step requires the cleaning and the substrate activation using oxygen (O_2) plasma treatment at 130 W for 10 min, see Fig 4.4.

Fig. 4.4 Plasma cleaner used during fabrication process

Then a solution of PS-stat-PMMA (18 mg) in toluene (2 mL) was spin-coated onto the glass substrate at 3000 rpm for 60 s. After the spin-coating, the sample was processed at high temperature (T_a = 290 °C for 300 s) in a rapid thermal processing machine (RTP, see Fig 4.5) in order to induce the grafting.

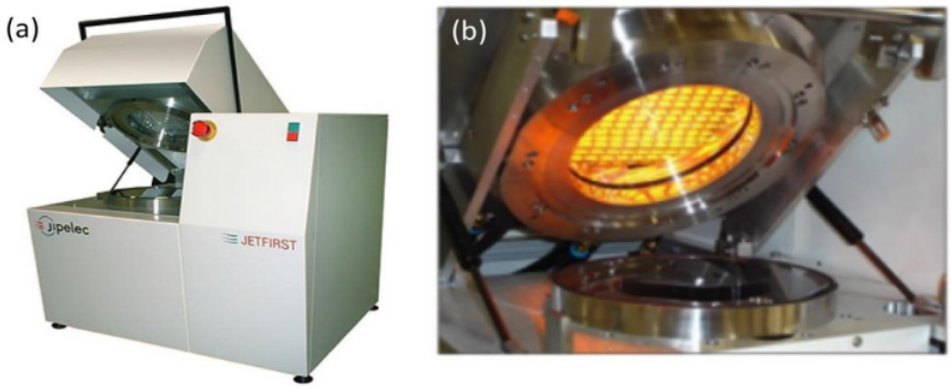

Fig. 4.5 RTP machine: (a) The Jipelec JetFirst 100C at INRiM, (b) halogen lamps furnace.

The annealing treatment has been followed by the cleaning of the residual RCP with sonication in a toluene bath for 6 min. At the end of this step, we have obtained a 7 nm thick grafted RCP layer, measured by the previously mentioned spectroscopic ellipsometry, see Fig 4.3.

After the grafting process, we have performed the BCP deposition. In this Thesis, we have used as BCP a polystyrene-block-polymethylmethacrylate (PS-b-PMMA) (66 kg mol^{-1}) with styrene fraction (f) of 0.50 and polydispersity index D = 1.09 previously purchased from Polymer Source Inc. and used without any further purification. A blended BCP solution, i.e. PS (with 3.1 kg mol^{-1} and D = 1.09) and PMMA (with 3.9 kg mol^{-1} and D = 1.18) homopolymers (1.12 mg) synthesized as described in [167] and blended with BCP (4.5 mg) and in 2 mL toluene, was used to spin-coat the previous RCP-neutralized substrate obtaining a 75 nm thick layer. The blending was necessary in order to increase the lateral ordering of the nanometric features and to reduce the required time for self-assembly up to one order of magnitude higher with respect to the unblended BCPs solution [165, 166]. Then, self-assembly was induced by thermal annealing with above mentioned RTP machine at 270 °C for 600 s in N_2 environment. In the end, in order to remove one polymer phase (PMMA) the sample has been exposed to ultraviolet radiation (5 mW cm^{-2}, λ = 253.7 nm) for 180 s and etched with an isotropic O_2 plasma treatment for 30 s with 40 W.

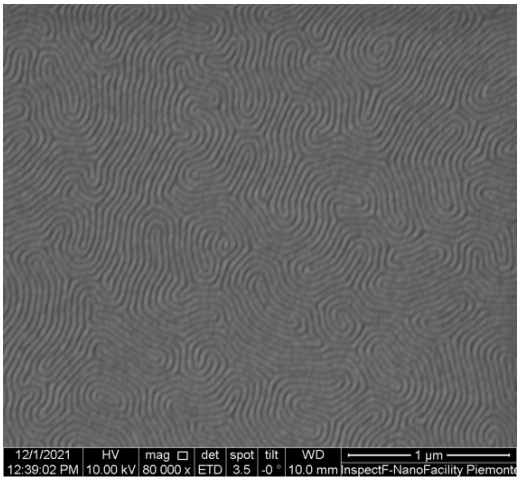

Fig. 4.6 SEM image of the uniform sample showing the morphology of the obtained lamellae. SEM image acquired with InspectF machine at the NanoFacility Piemonte lab in INRiM. It is worth to notice that in this case the lamellae have a low degree of order.

After obtaining the desired morphology, see fig 4.6, a 90 nm thick layer of Au was deposited on the samples exploiting a homebuilt RF sputtering system with a deposition rate of 0.2 nm·s^{-1} generated via an Ar plasma at 100 W at 5·10^{-3} mbar.

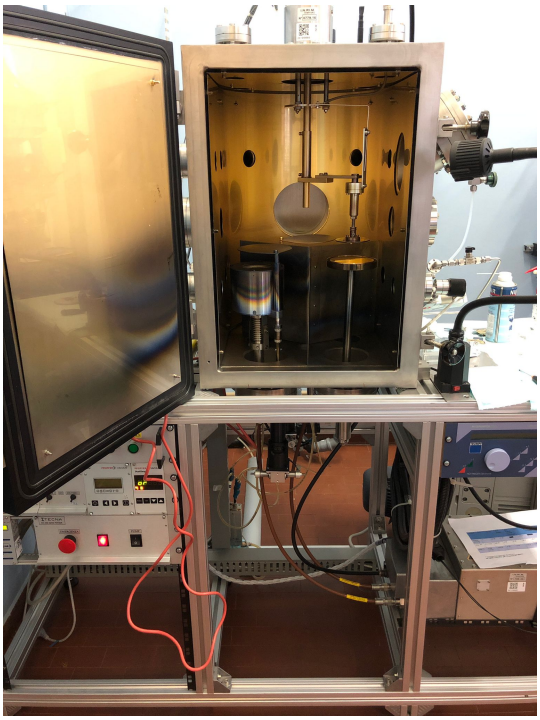

Fig. 4.7 Homebuilt RF sputtering system used for the gold deposition

Then the samples have been treated in a homebuilt sputtering using Ar at 100 W and pressure equal to $14 \cdot 10^{-3}$ mbar for 80 s in order to obtain a tilted etching and so a height gradient to measure the dependence of the optical response on the height.

Fig. 4.8 Homebuilt tilted etching sputtering

4.2.2 Samples with dewetted droplets

Since the previous technique leads to a nanopatterned large area but with the drawback of a low degree of order, we have focused our attention on another technique in order to obtain highly ordered lamellae. This is achievable by exploiting a dewetting process that in this case leads to the formation of micrometric domains: droplets. It is worth to notice that the dewetting process has intrinsically a stochastic nature as can be observed from the following figures:

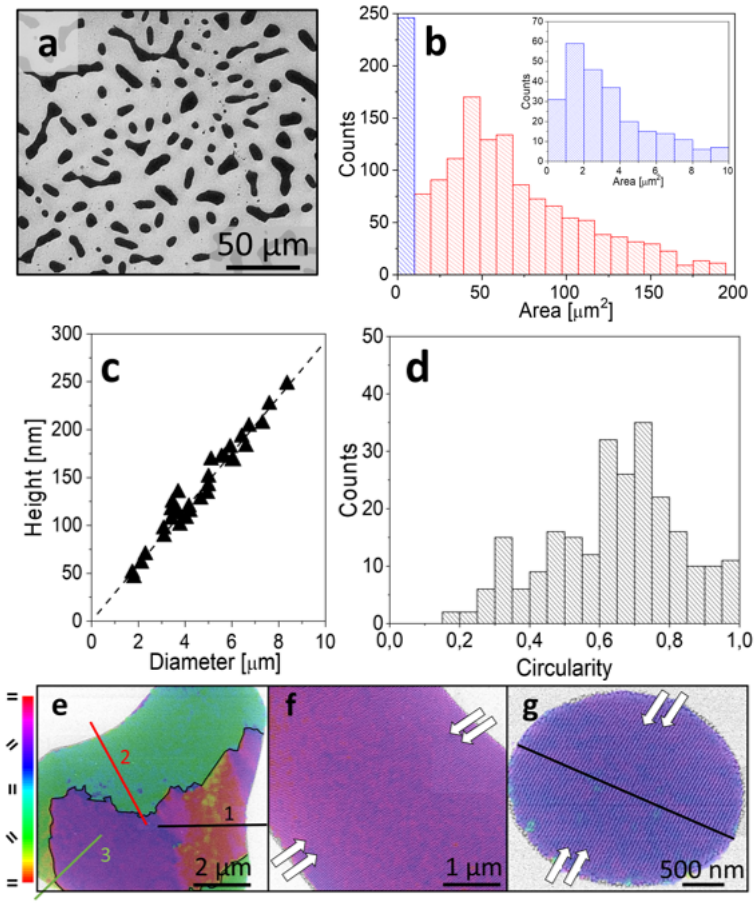

Fig. 4.9 (a) SEM image of dewetted BCP blend on an unpatterned substrate. (b) The droplet area distribution with inset of droplets with sub-10 μm^2 area (see the blue columns). (c) Droplet heights dependence on the diameter (d) Droplets circularity. (e-g) SEM image of a droplet with an irregular shape, elongated droplets with parallel dewetting fronts (reported as the white arrows), and elliptical droplets. The images are overlapped to a false-color map in order to describe the orientation of the lamellae along adjacent edges (indicated by the black, red, and green lines)[127].

In Fig 4.9, we report the results concerning a dewetting process on an unpatterned substrate. It is straightforward that this process induces the formation of randomly arrange droplets not only in terms of position but also in terms of morphology, see Fig 4.9a-b. Moreover, the linear dependence of the droplets' height on their diameter, reported in Fig 4.9c, with the wide distribution of circularity, reported in Fig 4.9d, imposes restrictions on their technological exploitation for example as a lithographic tool. Another important feature of this process is that the morphologies of the droplets can impact the ordering of the nanostructures. In Fig 4.9e, we can observe clearly that droplets with irregular shapes induce an alignment of the lamellae with defects in the inner zone. While, in more regular and elongated shapes the parallel borders induce the alignment along opposite orientations promoting the formation of a single defectless orientation, see Fig 4.9f. This effect becomes even more observable with small elliptical droplets, see Fig 4.9g. Since the nanopatterning of the substrate represents a simple and fast way to obtain small elliptical droplets during the dewetting process, we have exploited it to obtain micrometric droplets with highly ordered lamellae.

It is worth to notice that, unlike the previous uniform samples, in these ones, the neutralized substrate was a silicon substrate with 1 nm native oxide previously patterned. The patterns were composed of squares with micrometric edges and periodicity (equal to the edges) from 5 to 50 μm obtained through a laser lithographic process. The pattern has been obtained over a 5 mm $\times$ 5 mm area by means of a direct laser writer lithography machine (Heidelberg Laser Writer μPG101) using the AZ 5214E from MicroChemicals GmbH as optical resist spin-coated on the silica substrate with a 1 μm layer thickness. The resist has been exposed to a UV laser beam (λ=375 nm) with 15 mW power.

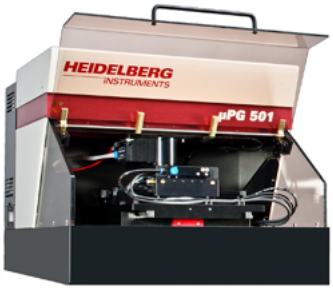

Fig. 4.10 Heidelberg Laser Writer μPG101

Then the sample has been immersed for 40 s in a 1:1 solution of deionized water and AZ Developer purchased from Merck Performance Materials GmbH, and subsequent rinsing in water for 60 s to perform the development. A RIE process has been performed with C_4F_8 and SF_6 to transfer the pattern into the silica substrate with a final depth of 200 nm. After the patterning of the substrate and the following neutralization, we have performed the deposition of the same BCP mixture previously mentioned, obtaining 35 nm uniform thin film, and the dewetting process followed by Au deposition (70 nm of gold in this case) as described in the previous section. It is worth to notice that at the end of the dewetting process the droplets are much higher ($\sim$ 100 nm) than the thin film measured before the self-assembly. At this point, in order to obtain the hyperbolic metasurface on a transparent substrate the pattern has been transferred by peeling off the Au deposited layer from the polymeric template by exploiting a flexible UV-curing resin (Optical Norland Adhesive 81) previously deposited on top of the sample. In this way, we have obtained lamellae with a 70 nm nominal height. The necessary steps and final results are reported in the following figures:

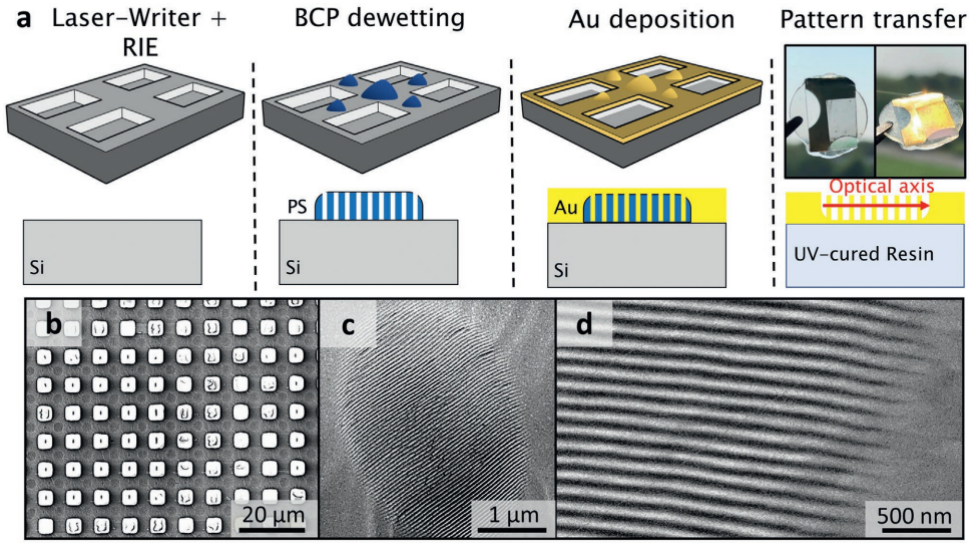

Fig. 4.11 (a) Schematic of the fabrication steps necessary for the highly ordered lamellae in micrometric droplets. (b-d) SEM images with a different magnification of the transferred pattern [127]

As mentioned before the pattern can induce the formation of lamellae in micrometric domains (droplets) by means of the dewetting process. This gives rise to

the formation of controlled droplets in terms of size, position, and shape, see Fig 4.12a-e.

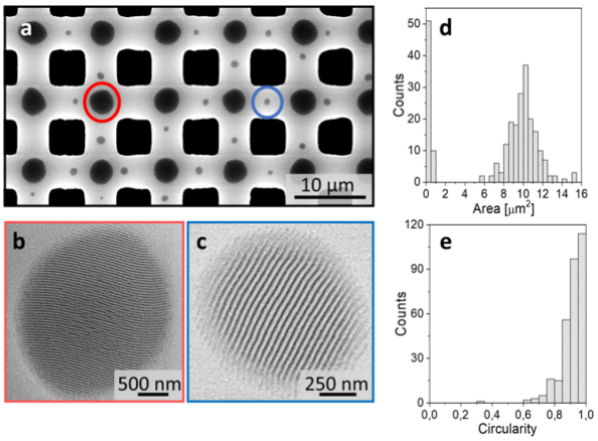

Fig. 4.12 (a) SEM image of dewetted BCP blend over a large-area patterned defined substrate. (b-c) SEM images of lamellar micrometric droplets in single grain configuration of the highlighted region in Fig 3.11a. (d) Area distributions centered that are clearly centered at 10 μm^2 for Fig 3.11b and at 0.5 μm^2 for Fig3.11c. (d) Circularity values of dewetted droplets over the patterned substrate [127].

Moreover in the obtained elliptical droplets, we can see that the lamellae are characterized by a higher degree of order with respect to the samples described in the previous section. Different gap sizes have been studied to determine the gap size value that allows the best results in terms of the degree of order and control of the position and shape. Here we report the results of this analysis:

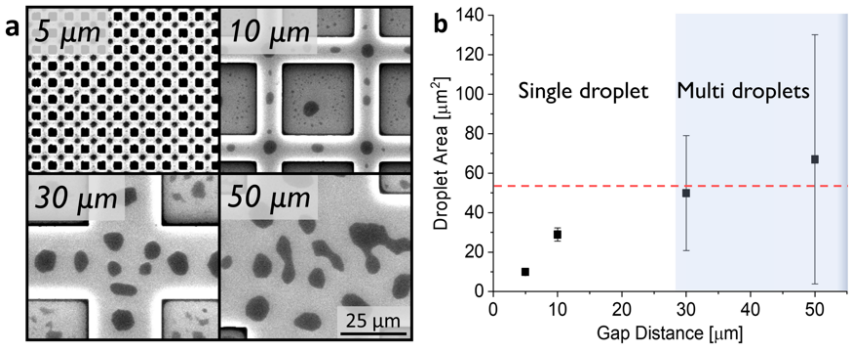

Fig. 4.13 (a) SEM images of different dewetted lamellae droplets obtained with different size gaps. (b) Dependence of the droplets area on the gap distance [127]

It is clear from Fig 4.13 that there is an opportunity to obtain single droplets by decreasing the gap between the squares with defined dimensions, position, and highly ordered lamellae.

4.3 Optical Characterization Setups

In this last section, I will discuss the setups and methodology used for the optical analysis of the samples fabricated with the processes described previously. In particular, we have measured the optical response of NV centers in nano-diamond coupled with the proposed hyperbolic metasurface by measuring their photoluminescence (PL) spectra and fluorescence lifetime. A dispersion of nanodiamonds in ethanol has been used to deposit the emitters on the sample surface. Here we describe the setups used for the PL and fluorescence lifetime spectroscopy.

4.3.1 Photoluminescence Setup

We have built up the photoluminescence setup at the laboratories at INRiM in Turin in order to characterize the PL of the nano-diamonds when they are coupled to the hyperbolic metasurface. Here we report the schematic of the PL setup used during our investigations:

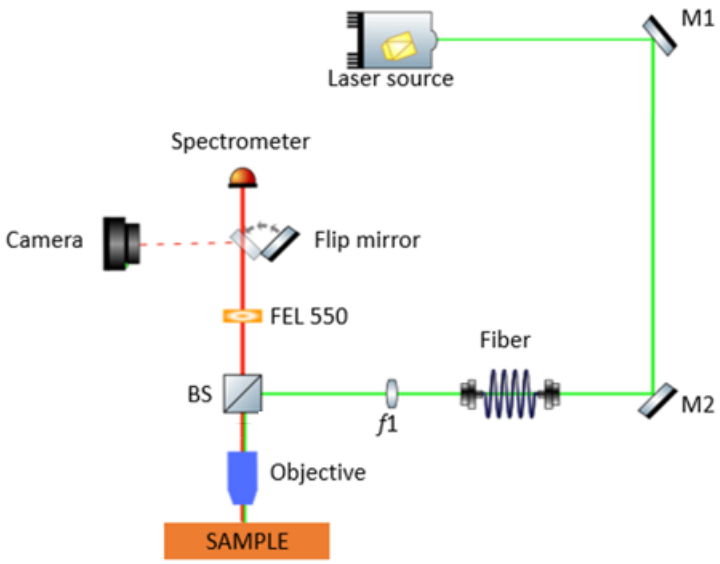

Fig. 4.14 PL setup used at the INRiM laboratories

As can be observed from Fig. 4.14, we have used as a laser source a Multi-wavelength Matchbox laser purchased from Integrated Optics to excite the NV

centers fluorescence in diamonds with a 520 nm wavelength radiation. Then the laser beam has been coupled into a single-mode fiber in order to obtain a clean Gaussian beam. It is worth to notice that the emitted power was 90 mW before the fiber coupling and 0.6 mW after it. The gaussian beam went through a collimation lens with focal length $f1$= 75 mm to control the divergence of the laser beam and a beam splitter. The objective was an Olympus 40X 0.17 NA objective. It was placed in a stage that can be finely moved to adjust the focus of the laser beam. Then the fluorescence has been collected from the sample, placed on a 3-axis NanoMax stage that allows fine-scale positioning, by the same objective and directed to the photosensors (i.e. camera or spectrometer). We used a long pass filter (FEL 550) to eliminate the laser signal from the collected light. Finally, a flip mirror is used to send the fluorescence signal to an iDs camera or to an Ocean Optics USB2000 spectrometer to measure the emitted spectrum from the NV centers. All the optical components (mirrors, lenses, filter, beam splitter) and the 3-axis NanoMax stage have been purchased from Thorlabs Inc.

4.3.2 Fluorescence Lifetime Spectroscopy Setup

In this section, we describe the fluorescence lifetime spectroscopy technique and setup used for the time-resolved fluorescence lifetime decay-rate measurements. The setup for the fluorescence lifetime spectroscopy is schematically represented in Fig 4.15:

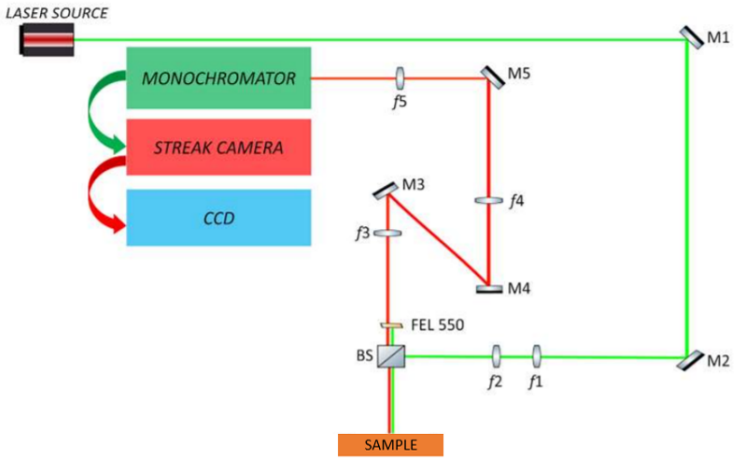

Fig. 4.15 Fluorescence lifetime spectroscopy setup used at the PoliTo laboratories

In this setup, the employed laser source is a Tsunami from Spectra-Physics, a tunable pulsed laser in the visible-IR wavelength range. This laser source can provide 10 ps laser pulses with an 80 MHz repetition rate. In the experiments, we centered the laser at 490 nm. The laser pulses have been directed towards a beam expander composed by two lenses (*f1* and *f2*) to adjust the laser collimation. Then, a beam splitter (BS) has been used to reflect the laser pulses into a 20× objective that can focus them on the sample. The sample has been positioned on a Vitec microscope stage that allows to have double-side imaging. From one side, we have acquired the sample surface image in white light by means of a 100× microscope objective (Nikon 100 × 0.95 NA), while from the opposite side, we have employed a Nikon 20 × 0.40 NA objective to focus the laser pulses on the sample surface and to collect the NV centers fluorescence. Afterward, the fluorescence has been directed to a long pass filter (FEL 550 from Thorlabs) that filters out the reflected laser pulses from the sample. Then the PL passes through a set of lenses (*f1*,*f2* and *f3*) and after it has been injected into a monochromator (Princeton Instruments Acton SpectraPro SP-2300i).

Fig. 4.16 Princeton Instruments Acton SpectraPro SP-2300i

The employed monochromator has a 1200g/mm grating with a 0.1 nm resolution. The monochromator is coupled to a Hamamatsu universal streak camera and a CCD camera allowing the possibility to perform time-resolved fluorescence decay measurements, and so to determine the lifetime values or simply the behavior if the lifetime values are below the resolution.

Fig. 4.17 Hamamatsu universal streak camera

Indeed, a streak camera is an ultrahigh-speed detector that can analyze light emission phenomena occurring in very short time periods. Once the laser pulse is projected onto the slit, it is focused by the lenses into an optical image on the streak tube photocathode. For example, we consider four light pulses, each with a different light intensity, and spatial and temporal offset, see Fig 4.18. In the photocathode, the photons are sequentially converted into electrons. The number of electrons is proportional to the intensity of the incident light. Then these electrons are accelerated and directed toward the phosphor screen passing through a pair of sweep electrodes where a high voltage is applied. This results in a high-speed sweep: the direction of the electrons is swept from top to bottom. At this point, the electrons are conducted to a micro-channel plate (MCP) where they are multiplied several thousand times. Afterward, they go against the phosphor screen where they are converted into light.

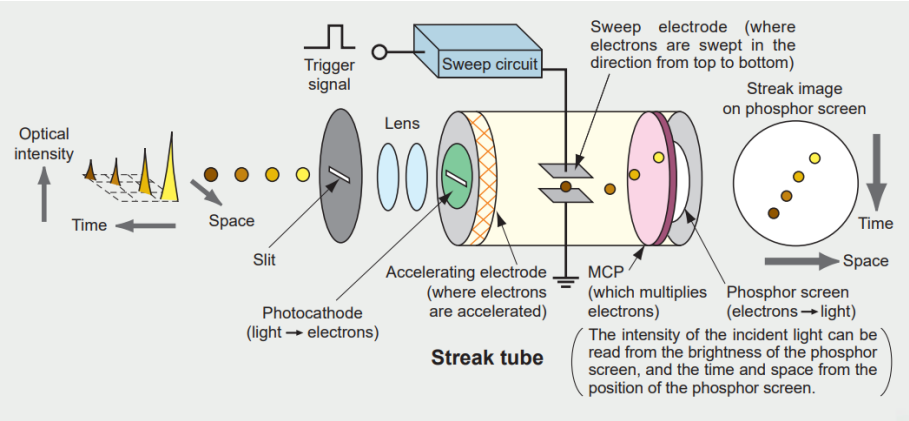

Fig. 4.18 Schematic of the functioning of the Hamamatsu universal streak camera from its manual

The first incident light pulse will have the corresponding fluorescence image positioned at the top of the screen, followed by the others in descending order. It is straightforward that in this way the vertical axis on the phosphor screen will correspond to the temporal axis. For what concerns the brightness of the fluorescence images, is proportional to the intensities of the corresponding incident pulses. Finally, the wavelength-decay time maps can be acquired, see the following figure as an example:

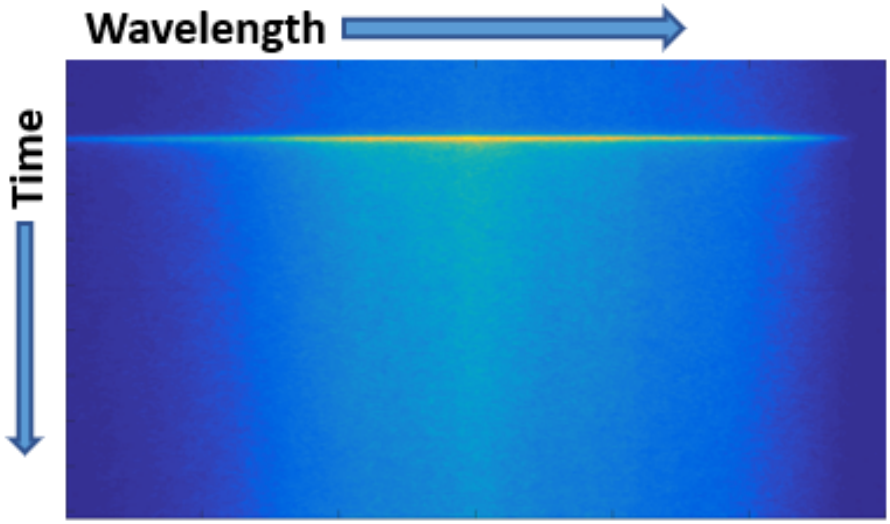

Fig. 4.19 Example of wavelength-decay time map.

Chapter 5

Hyperbolic metasurface characterization

In this Chapter, we will discuss the results obtained from our research and investigations on the proposed hyperbolic metasurface. The chapter is divided into two main parts: Simulation Results and Optical Characterization Results. In the first section, we report the results related to the simulations obtained by means of modal analysis exploiting quasi-normal modes formalism and a model implemented with the software *Comsol Multiphysics 5.2* based on the Finite Element Method. In the second section, we report the results concerning the optical characterization obtained by means of the setups described in the previous Chapter.

5.1 Simulations Results

First, we performed simulations to determine the optical response of the nanostructure by performing a modal analysis in order to determine the modes sustained by the hyperbolic metasurface. The model, the geometrical configuration, and the parameters used for the modal analysis and simulations have been described and reported in Methodologies chapter. We show the results of the modal analysis in the following figure:

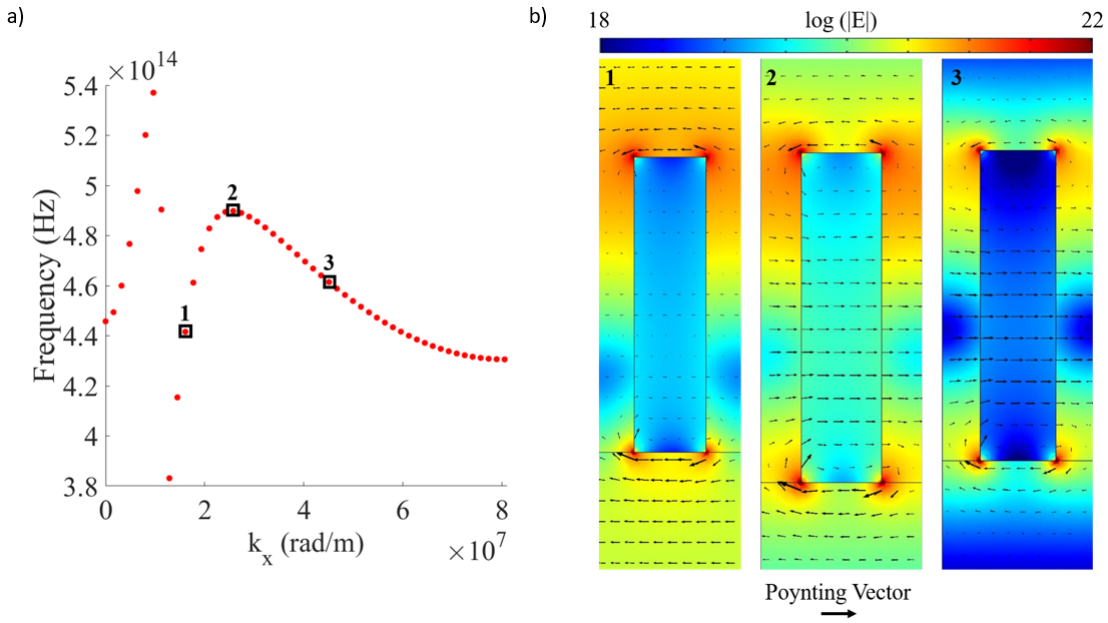

Fig. 5.1 (a) Dispersion curve estimated with modal analysis for 70 nm high lamellae. (b) Distribution in logarithmic scale of the electric field associated to the mode and Poynting vectors (black arrows) distribution for the three points highlighted in Fig. 5.1a.

From Fig 5.1a, we can see clearly that a mode appears with an interesting behavior. Indeed, by considering the group velocity, defined as $v_g = \frac{d\omega}{dk}$ with $d\omega = 2\pi df$, we can observe that for low wavevector values the group velocity has a positive value, and by increasing the wavevector values the group velocity becomes first equal to zero and then negative. The particular behavior can lead to the possible simultaneous presence of forward (positive group velocity) and backward (negative group velocity) propagation waves. Furthermore, a stationary wave (group velocity equal to zero) can be found. It is worth to notice that the dispersion curve is beyond the light line in the substrate and the electric field related to the mode is strongly localized on the surface, see Fig 5.1b. Hence, we can define the calculated mode a surface mode sustained by the hyperbolic metasurface. In Fig 5.1b we can also see the different behaviors of the Poynting vectors for the three points highlighted in Fig 5.1a. We can observe that for point 1 the Poynting vectors are mainly localized outside the substrate and superstrate and directed from right to left (forward). For point 2, the distribution is almost uniform, but the direction is from left to right around the lamella, while it is the opposite, from left to right (backward), inside the lamella (standing wave). While for point 3, the distribution is mainly localized inside the lamella and oriented from left to right. It is worth to notice that this system can

be compared to a positive index material (PIM) and a negative index material (NIM) that are coupled.

To determine how the surface mode is affected by the lamellae height, we performed the modal analysis for different lamellae heights. We report the results in Fig. 5.2:

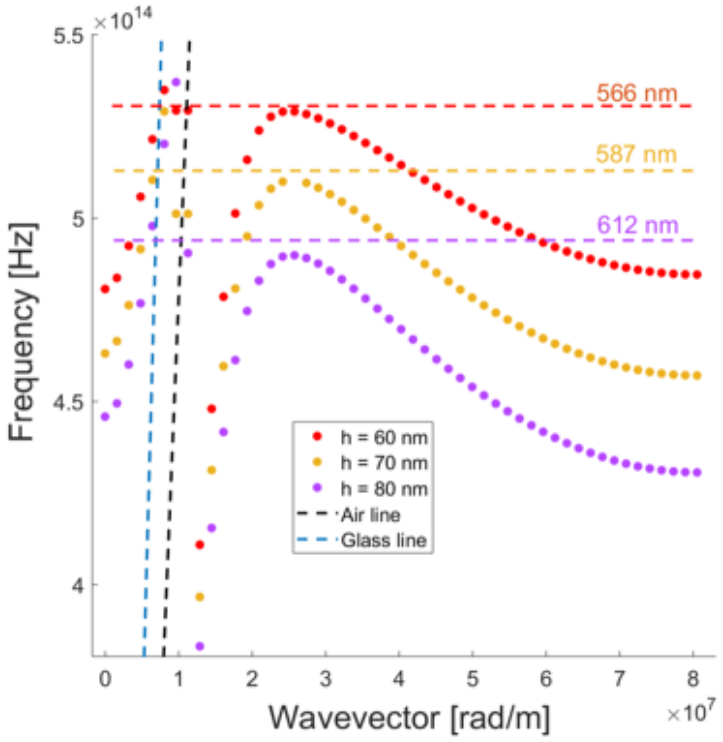

Fig. 5.2 Mode analysis performed for three different hyperbolic metasurface heights: 60 nm, 70 nm, and 80 nm. At the highlighted wavelengths, it is possible to observe the sustained modes that are stationary.

From Fig 5.2, we can see that increasing the height causes a redshift of the sustained modes, including the stationary mode.

With the software Comsol Multiphysics 5.2, we have analyzed the behavior of the hyperbolic metasurface and the effects of the surface modes when a photon source, a dipole, is coupled to the hyperbolic nanostructure. In particular, we have estimated the electric field distribution in the near-field by performing a frequency sweep between 500 nm and 800 nm by varying the height of our hyperbolic metasurface and keeping the distance dipole-metasurface constant (5 nm). We found out that the emitted radiation can couple with the modes sustained by the structure for

wavelengths close the ones estimated for the stationary mode in the previous modal analysis. As the radiation couples to the metasurface, the radiation can propagate efficiently along the hyperbolic structure as can be seen in the following figure:

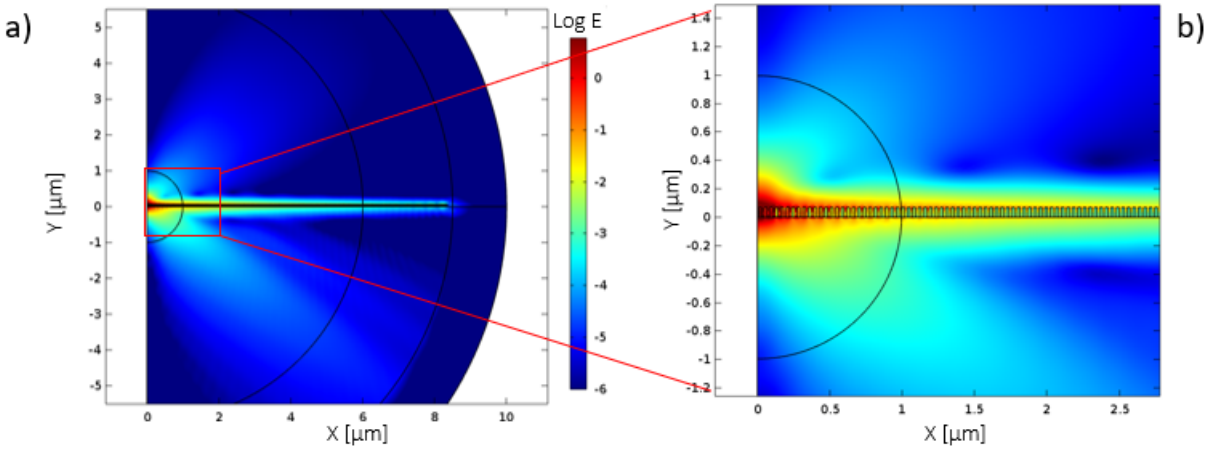

Fig. 5.3 (a) The estimated electric field distribution for a dipole emitting at 595 nm in the near field coupled to a hyperbolic 70 nm high metasurface. (b) The inset shows clearly the dipole emission coupling with the sustained mode in the HMM.

After considering the electric field distributions, we have estimated the Purcell factor for different metasurface heights. The Purcell factor has been estimated as the ratio between the emitted power by the dipole when coupled to the hyperbolic metasurface and the power emitted when placed in an air domain. From Fig 5.4a, we can see that the Purcell factor shows narrowband peaks. It is worth to notice that Purcell factor peaks have been found around the wavelength range where we have previously reported the stationary modes found in the modal analysis.

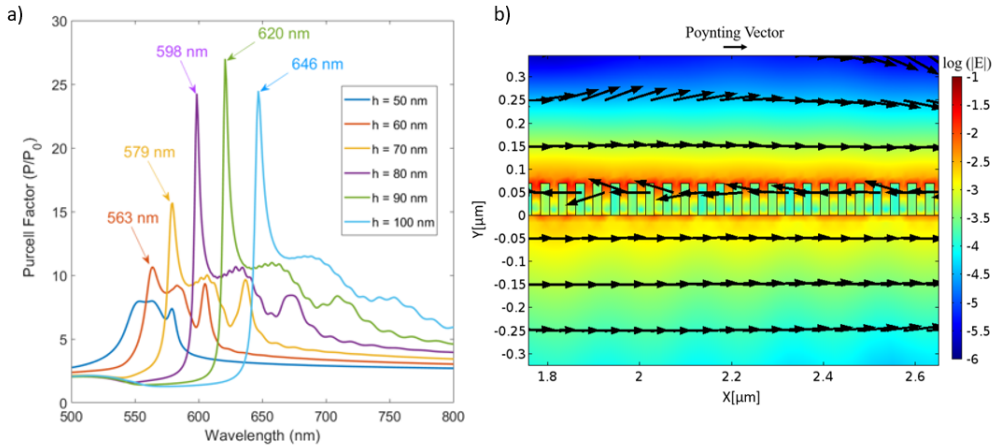

Fig. 5.4 (a)Purcell factor reported for different hyperbolic metasurface heights. The simulations have been performed with HMM heights from 50 nm to 120 nm with 10 nm steps. (b)Electric field distribution with black arrows that indicate the direction of the Poynting vectors.

Moreover, when we considered the Poynting vectors we observed an exotic behavior in the direction of the energy propagation for the wavelengths in which we expect stationary waves. Indeed, we found Poynting vectors propagating in both directions along the hyperbolic metasurface as mentioned in the previous modal analysis, see Fig. 5.4b. Poynting vectors are pointed forward around the lamellae (in air and also in the first nanometers of glass), while they are oriented in the opposite direction (backward) inside the hyperbolic metasurface.

The backward propagation enables an effective feedback mechanism that leads to an amplification. It is worth to notice that the effective feedback mechanism can be compared to the effect of a mirror in a resonant optical cavity. The optical cavity is typically composed of two mirrors at the end of a medium reflecting light back and forth inside the cavity leading to a rapid growth of the light intensity. Hence in a similar way, amplification can be provided to the radiation coupled with the hyperbolic metasurface. This exotic amplification could be related to the presence of averaged negative index inside the lamellae. Indeed, if we consider a negative refractive index slab (N) coupled with a positive refractive material (P) it has been demonstrated that light propagating in P can continuously couple to N where it propagates in the opposite direction. Hence, an effective feedback mechanism can occur and it leads to transmission resonances and optical bistability [143].

In addition, it is straightforward from the Fig. 5.4a that the spontaneous emission enhancement can be tuned by changing the height of the hyperbolic metasurface in order to match the peaks with the desired wavelength, for example, the NV centers ZPL. Indeed, by tuning the height it is possible to tune the modes that are sustained by the metasurface and consequently the wavelength range where the effective feedback mechanism leads to the enhancement analogous to the optical cavity. This represents one of the most significant advantages the HMMs can introduce by coupling them to an SPS. Moreover, a redshift of the Purcell factor peaks is caused by the increase in the height which is consistent with the results found in the modal analysis.

5.2 Optical Characterization Results

In this section, we report the results concerning the optical characterization of the proposed hyperbolic metasurface coupled with NV centers in nanodiamonds as photon emitters. We have fabricated two kinds of samples: uniform samples with a height gradient and samples with dewetted droplets. For all samples, the Au/air lamellae had around 19 nm lateral size.

In order to fabricate the samples, we have exploited the self-assembling BCP properties with the techniques and parameters described in the Methodologies chapter. Here, we show the obtained lamellae for the uniform samples with a height gradient (Fig. 5.5), and the dewetted droplets (Fig. 5.6):

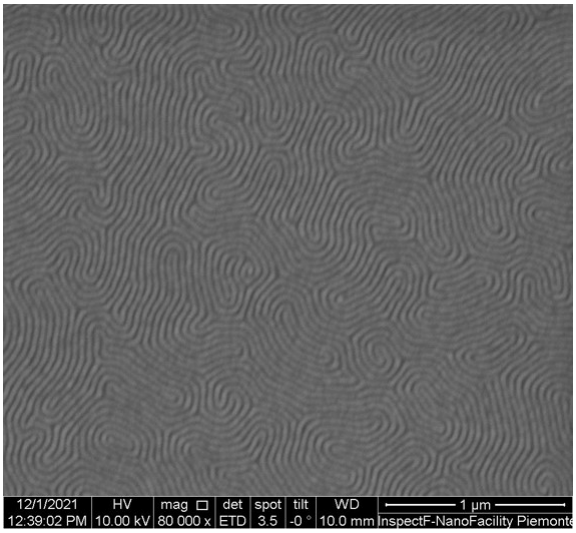

Fig. 5.5 SEM image of the uniform sample showing the morphology of the obtained lamellae.

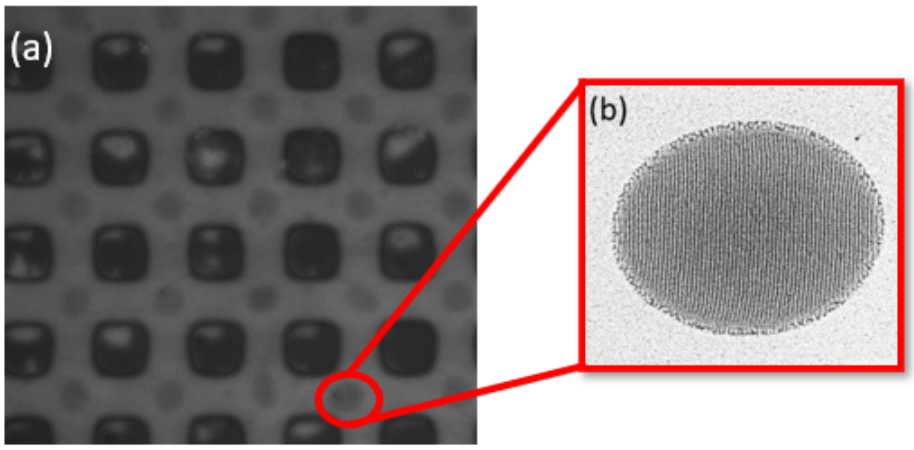

Fig. 5.6 (a) Image of the patterned sample with dewetted droplets. (b) The inset of the highlighted region in Fig 5.6a shows the detailed morphology of the highly ordered lamellae in the micrometric domains.

As can be observed in Fig 5.5 and Fig 5.6b, we have obtained Au/ air lamellae with different degrees of order. It is worth to notice that the dewetting process on a patterned sample can produce small regions (i.e. micrometric droplets) with highly ordered lamellae. During our analyses, we noticed that high-ordered lamellae can be produced even in larger regions inducing the dewetting process on unpatterned samples. This can be explained by the intrinsic random nature of the dewetting on unpatterned surfaces that can sometimes lead to larger droplets with lamellae order determined by the process parameters. Indeed, as we have previously described, the dewetting process occurs randomly on an unpatterned substrate, see Fig 4.9. In the following figure, we have reported the SEM images of an unpatterned sample with highly ordered lamellae characterized by 70 nm height obtained with the dewetting process.

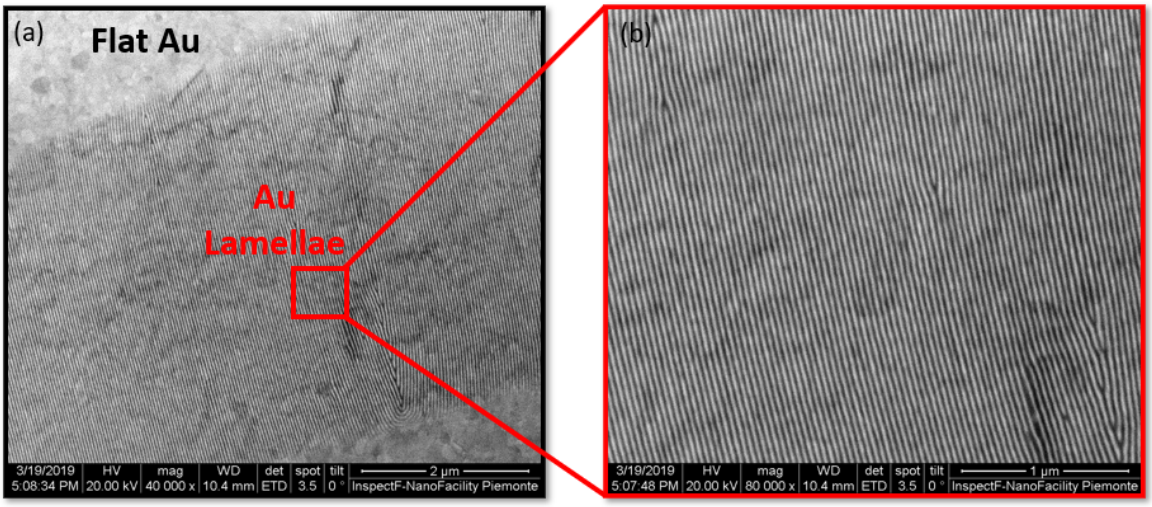

Fig. 5.7 (a) SEM image of the unpatterned sample with dewetted lamellae.(b) Inset of the highlighted region in Fig 5.7a showing the detailed morphology of the highly ordered lamellae.

As first step for our optical analysis, we have measured the photoluminescence spectra of NV centers in nanodiamonds as previously reported. To deposit the photon emitters on the sample surface, a dispersion of nanodiamonds in ethanol has been used. For example, here we report the images of photoluminescent nanodiamonds acquired during the optical investigation:

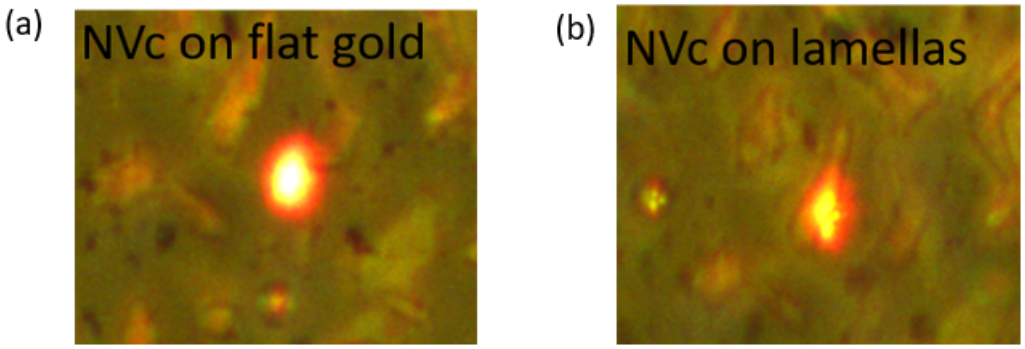

Fig. 5.8 (a) PL image of NV centers in nanodiamonds on flat Au deposited on the unpatterned sample with dewetted lamellas and on the Au/air lamellas (b) superposed to white light image of the sample.

To acquire the PL spectra we have used the home-built setup reported in Fig 4.14. First, we investigated the uniform sample with a height gradient in order to

observe the optical response of the hyperbolic metasurface with a variation in height. Here, we show the normalized PL spectra measured from the NV centers coupled to lamellae on the uniform sample:

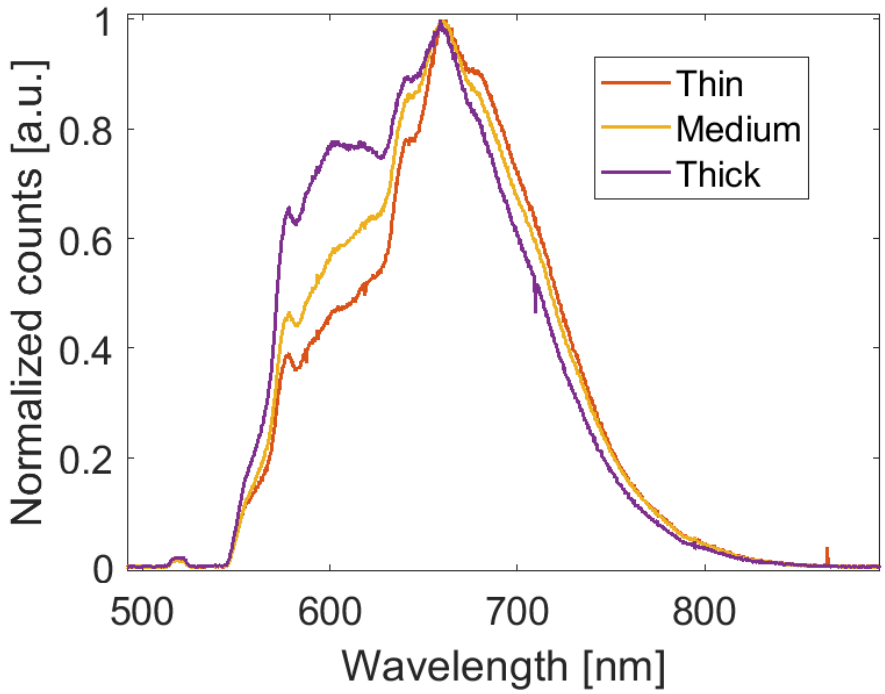

Fig. 5.9 (a) PL spectra of NV centers in nanodiamonds on gold/air lamellae with different thicknesses.

From Fig 5.9, we can observe that the emission from the NV centers clearly changes in regions with different lamellae thicknesses. In particular, it is worth to notice that a broad peak starts to emerge between 585 nm and 625 nm with increasing thickness. Moreover, the ZPL at 575 nm measured for thick lamellae is increased drastically with respect to the NV center emission when placed on the thin lamellae. This behavior can be explained by the dependence of the Purcell factor on the height of the lamellae as reported in Fig 5.4. Indeed, a spontaneous emission enhancement in the wavelength range between 570 nm and 625 nm was previously estimated for a structure with 70 nm high lamellae. The spectra acquired for thick lamellae are coherent with the estimated Purcell factor since the obtained thick lamellae are nominally 75 nm high and the enhancement occurs in the same wavelength range estimated in the simulations.

For what concerns the sample with dewetted droplets and highly ordered lamellae, we have measured the PL spectra and compared them to the ones of the uniform sample previously shown. We report the compared spectra in the following figure:

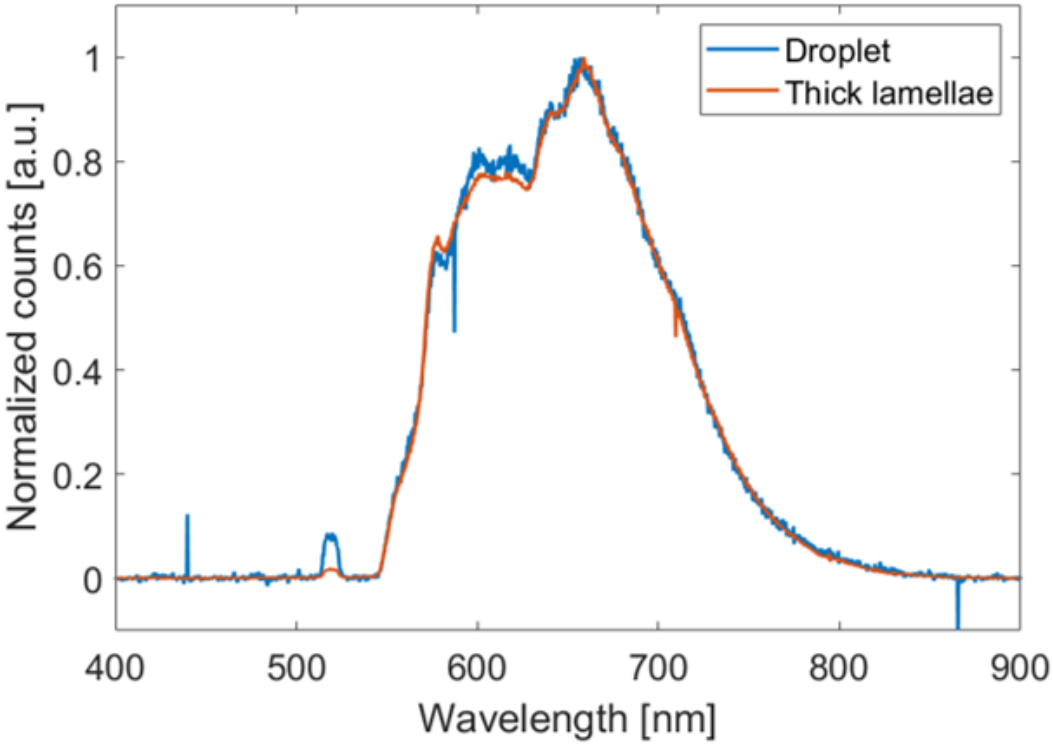

Fig. 5.10 (a) PL spectra of NV centers in nanodiamonds on gold/air lamellae on the uniform sample (orange line) and on the sample with dewetted droplets (blue line).

As can be seen from Fig 5.10, the PL spectra from the two kinds of samples are almost identical. In particular, they show the same emerging broad peak between 585 nm and 625 nm. Therefore the lamellae affect the NV center spontaneous emission in the same way in the two cases even if they possess different degrees of order. This could be explained by the fact that the droplets had dimensions comparable with the correlation length that characterized the pattern of the grains in the uniform sample, see Fig 5.5 and Fig 5.6. Hence the emitters interact similarly with the to samples because of their comparable morphology.

To make a comparison of the measured PL spectra and the estimated enhancement related to the Purcell factor we have considered for simplicity only the PL spectra

from the dewetted droplets. We have compared the acquired PL spectra and the product of the NV center spectrum on the glass with the estimated Purcell factor.

We report the results in Fig 5.11:

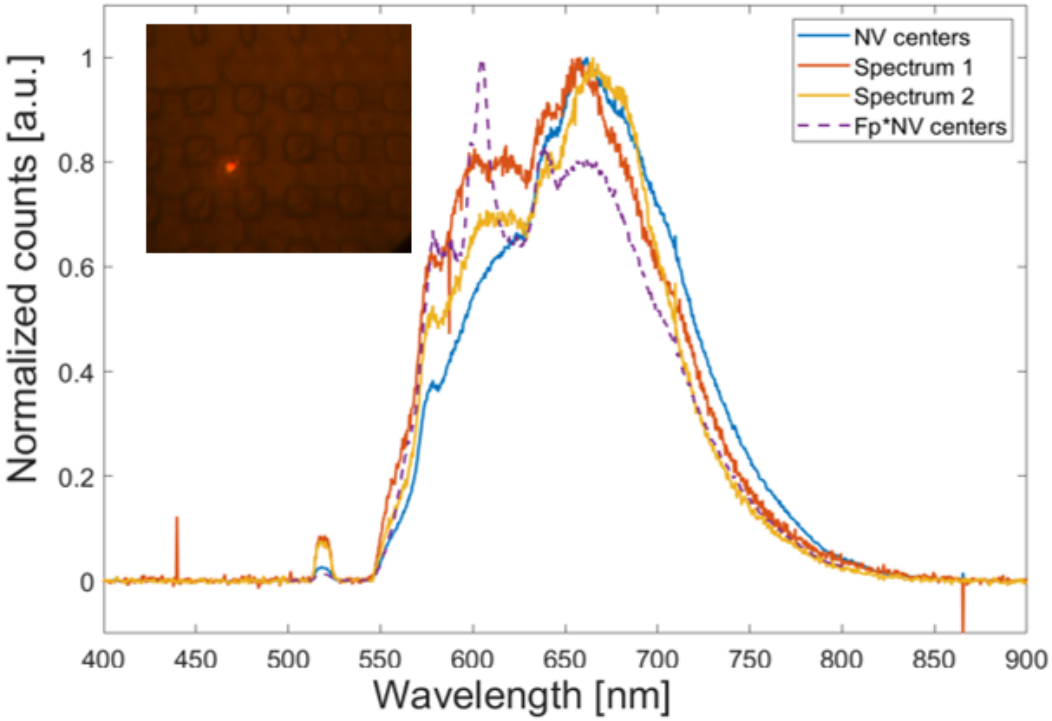

Fig. 5.11 Comparison between the PL spectra of NV centers in two different nanodiamonds on gold/air lamellae on the sample with dewetted droplets (orange and yellow lines), NV centers spectrum on the glass (blue line), and the product of the NV center spectrum on the glass with the estimated Purcell factor for different heights (dashed purple line). In the inset, an image of the nanodiamond emitting *Spectrum 1* is shown.

It is worth to notice that for the product between the estimated Purcell factor and the NV center spectrum we have exploited the averaged Purcell factor calculated for lamellae with different heights (i.e. 50 nm, 60 nm, 70 nm, and 80 nm). We have estimated the average value in order to consider the non-uniformity in the droplet thickness related to their curvature. From Fig 5.11, it is clear that a narrow peak should emerge at 605 nm when the NV centers are fully coupled to the hyperbolic metasurface. Moreover, the emerging peak overlaps clearly with the region where we have measured an enhancement and a modification of the NV centers spectrum. The fact we did not measure a narrowband peak could be explained by the dimension of the droplet with highly ordered lamellae since small regions of highly ordered lamel-

lae might sustain propagation modes that are slightly different from the estimated ones also affecting the effective feedback mechanism.

In order to establish how the dimension of the domains with highly ordered lamellae affects the NV center spontaneous emission, we have performed the PL spectra measurements on the unpatterned sample with dewetted droplets, reported in Fig 5.7.

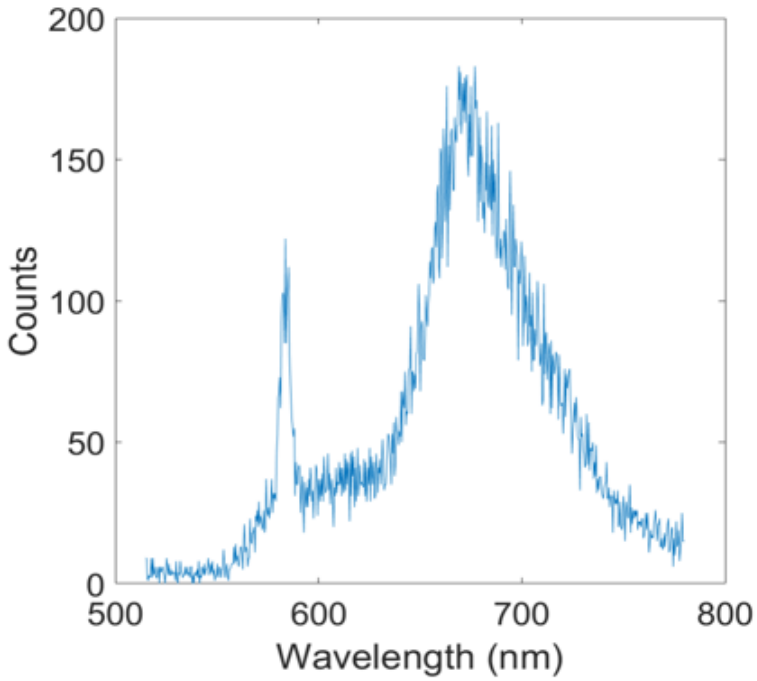

Fig. 5.12 PL spectrum acquired from NV centers on the unpatterned sample with dewetted droplets.

Fig 5.12 shows an emerging narrow peak that can be observed clearly. Moreover, this peak is centered at 578 nm while the Purcell factor estimated for a 70 nm high hyperbolic metasurface has a peak centered at 579 nm. Hence, the presence of the emerging narrow peak shows the fact that the obtained enhancement depends not only on the degree of order of lamellae but also on the dimension of the uniform domains with highly ordered lamellae. Therefore, it is necessary to obtain a few micrometer broad domains with highly ordered lamellae in order to fully sustain the estimated propagation modes and tune precisely the enhancement for specific wavelengths of the NV center spontaneous emission. We will discuss in more detail how this kind of domain can be obtained in the Future Perspectives Chapter.

After the PL spectrum analysis, we performed the time-resolved lifetime decay measurements on the unpatterned sample with dewetted droplets exploiting the setup reported in Fig 4.15. Here, we report the measured results:

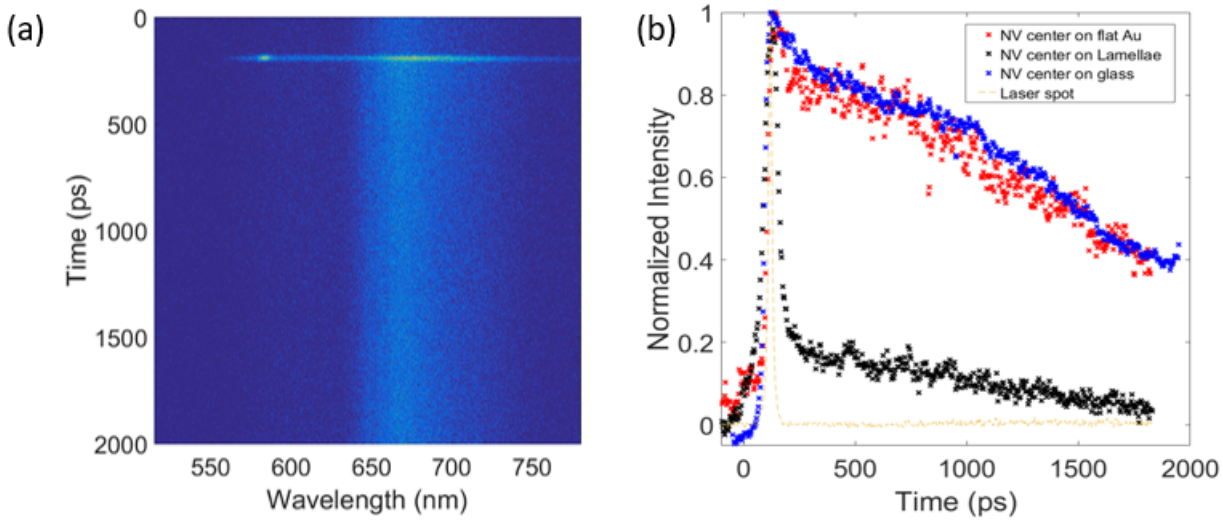

Fig. 5.13 (a) Time-resolved lifetime decay measurement map of emitting NV centers in nanodiamonds on gold/air lamellae on the unpatterned sample with dewetted droplets. (b) Comparison of the intensity decays for the emission measured on NV centers on different substrates: on the glass (blue dots), on flat gold (red dots), and on the highly ordered lamellae in a few micrometric domain (black dots).

The time-resolved lifetime decay map measured for NV centers in nanodiamonds on the unpatterned sample with dewetted droplets is reported in Fig 5.13a. From the acquired map, we can observe how the fluorescence signal evolves in time. In addition, also in this case we can see the peak at 578 nm, observed previously during the PL spectra analysis, as a bright narrow spot. In Fig 5.13b, we have reported the intensity decay in time measured from the map in Fig 5.13a and compared it to the intensity decay of the NV centers on different substrates. It can be clearly observed that there is a strong reduction of the lifetime value when the NV centers are placed on the hyperbolic metasurface. Furthermore, we have estimated a lifetime value that is comparable with the 30 ps laser pulse used for the measurement by fitting the intensity decay for NV centers coupled to the HMM with a bi-exponential function. The measured value is far below the 12 ns value commonly reported for NV centers in nanodiamonds on a glass substrate [144].

It is worth to notice that with the previous methodologies analyses, PL, and lifetime decay measurements, it is not possible to characterize in a precise way the increase of the available Local Density of Optical States (LDOS) affecting the NV centers' spontaneous emission. This is mainly due to the fact that the dispersed nanodiamonds cannot be pre-characterized before the coupling with the hyperbolic metasurface since they are dispersed randomly and contain a random number of emitting defects. Therefore, a possible solution could be the use of an optical nano-probe in order to analyze the hyperbolic metasurfaces with a more deterministic method. We propose a diamond-based nano-probe for optical near-field characterization in order to have a tool for the measurements of the larger LDOS present with the hyperbolic metasurface. We will discuss this tool in more detail in the next Chapter.

Chapter 6

Diamond-based nano-probe for optical near-field characterization

In this Chapter, we present a tool to measure the enhancement of the available LDOS in a more deterministic way: a diamond-based nano-probe. As we have mentioned in the previous Chapter, the precedent analysis methods cannot be exploited to measure the enhancement in the number of available optical states. This is mainly due to the fact the investigated nanodiamonds are randomly dispersed on the sample surface and therefore it is not possible to scan the hyperbolic metasurface in order to estimate the region with higher LDOS. In order to overcome this limitation, we propose a diamond-based nano-probe. It is worth to notice that nano-diamond probes have been already widely exploited for what concerns electromagnetic field sensing as reported in literature [145–150], while the studies as optical probes are still limited [151]. The diamond-based nano-probes can be exploited for the near-field optical characterization of hyperbolic metasurfaces described in the previous chapters. The proposed optical nano-probe is a modified Atomic Force Microscopy (AFM) tip on top of which we attached a nanodiamond hosting NV centers, see Fig 6.1.

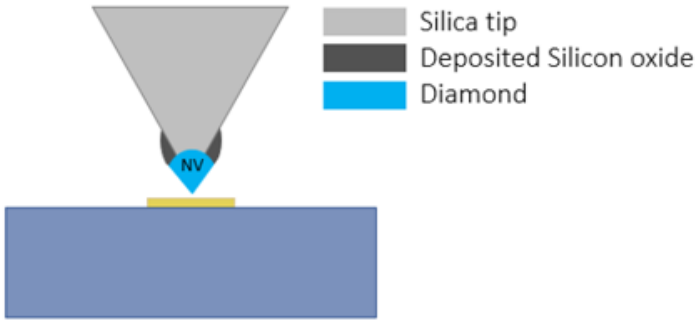

Fig. 6.1 (a) Schematic view of the diamond-based near-field probe.

In this way, it would be possible to measure the optical coupling of the nano-diamond with NV centers to the metasurface by measuring the emission spectrum at varying distances from the metasurface itself. More importantly, the measured spectra can be compared to the emitted spectrum of the nano-probe when it is not coupled to the hyperbolic metasurface. Hence, a measurement of enhancement due to the increase in the available number of optical states can be performed more directly. Moreover, using this kind of optical nano-probe in an AFM setup for tip-enhanced optical spectroscopy it would be also possible to scan the metasurface optical response and topography in order to overlap the two obtained scans to determine which regions and features determine the larger enhancement in the number of available optical states. In Fig 6.2, we report schematically the near-field characterization setup functioning:

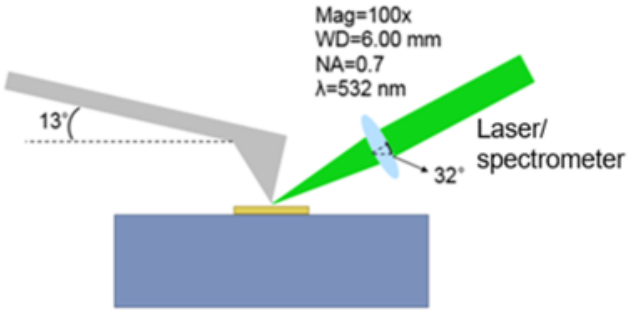

Fig. 6.2 Sketch of the characterization setup showing the near-field probe excited by a laser beam focused by a 100x objective. The same objective collects the fluorescence from the diamond probe.

The proposed method consists of an Atomic Force Microscopy setup with the opportunity to excite the near-field probe with a laser beam focused by a 100x objective and with a wavelength centered at 532 nm. The same objective collects the fluorescence from the nanodiamond probe and directs the emission to a spectrometer. During our investigations, we performed surface topography measurements of the hyperbolic metasurface and tip optical spectroscopy of the diamond-based nano-probe coupled with the proposed HMM.

We will discuss the exploited methodology for the above-mentioned measurements in more detail in the last section of the Chapter.

The chapter is divided into three sections: simulation results of the proposed diamond-based nano-probe, diamond-based nano-probe fabrication process, and optical characterization with the diamond-based nano-probe.

6.1 Nano-probe modeling results

As the first step to characterize the proposed optical nano-probe we simulated and estimated the spontaneous emission enhancement for a 70 nm high hyperbolic metasurface coupled with a dipole in the wavelength range of the NV centers at different distances with the software Comsol Multiphysics 5.2 by varying the dipole vertical position with 5 nm steps to simulate the approaching of the modified tip to the hyperbolic metasurface. It is worth to notice that by applying this methodology we can estimate the critical distance at which the enhancement becomes significant, so when the most efficient coupling occurs between the photon source and the metasurface.

The results are reported in the following figures:

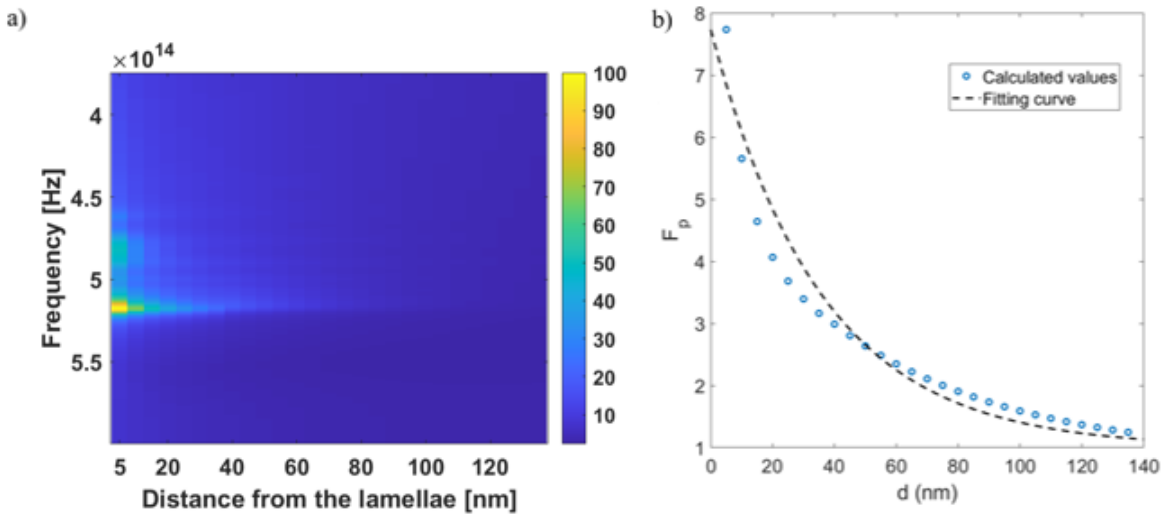

Fig. 6.3 (a) Percentage ratio between the Purcell factor values estimated for different dipole heights and the one estimated for the closest dipole, i.e. 5 nm from the surface. (b) Integrated values of the Purcell factor reported in Fig 6.3a (blue circles) for $625nm < \lambda_0 < 735nm$ (4.79 THz-4.09 THz). Calculated data are fitted by the black dashed line.

In Fig 6.3a we reported the percentage ratio between the Purcell factor values estimated for different dipole heights and the one estimated for the closest dipole (5 nm from the surface). In Fig 6.3b, we integrated the values reported in Fig 6.3a for $625nm < \lambda_0 < 735nm$. The curve shows a behavior similar to an exponential decay.

This behavior is consistent with the evanescent nature of the surface mode sustained by the hyperbolic metasurface.

We have fitted the data with the following equation:

$$F_p(d) = F_p(0) \cdot e^{-\frac{d}{d_0}} + 1 \tag{6.1}$$

Where d is the distance between the dipole and the metasurface. The fitting procedure results in an amplitude of the exponential function $F_p(0) = 6.73$, and a decay length $d_0 = 35.65$ nm.

From fig 6.3b, it is clear that the dipole vertical position plays a crucial role in the determination of spontaneous emission enhancement. Moreover, the Purcell factor value decreases drastically just by increasing the dipole height of 5 nm. Indeed, by moving the dipole from 5 nm to 10 nm from the metasurface the Purcell factor peak drops to 32 % in the previous map. In the next section, we will discuss a method to fabricate the proposed diamond-based nano-probe.

6.2 Diamond-based nano-probe fabrication process

In this section, we present the method used to fabricate the diamond-based nano-probe. As first step of the fabrication process, we dispersed nanodiamonds on a pre-patterned silica sample. The pattern was a grid of 5 μm size squares realized with the laser writing process described in the Methodologies Chapter. After the dispersion of the nanodiamonds, we scanned the sample surface with the PL setup reported in Fig 4.14 in order to determine the brightest nanocrystals, see Fig 6.4:

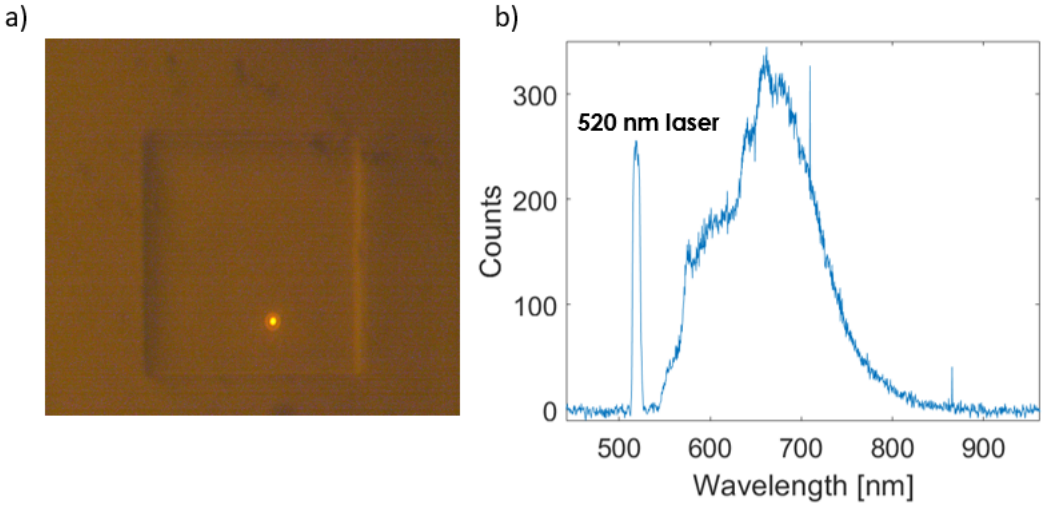

Fig. 6.4 (a) Wide-field white light image of the pre-patterned silica sample, used for the determination of the brightest nanodiamonds, superimposed to the fluorescence image of an emitting nanodiamond. (b) PL spectrum measured from the emitting nanodiamonds visible in Fig 6.4a

The sample was then loaded into a vacuum chamber of a Dual Beam electron microscope (an *FEI Quanta 3D FEG* shown in Fig 6.5) together with a gold-coated AFM tip purchased from Nano World with a nominal force constant of 0.1 Nm^{-1} and resonant frequency of 35 kHz.

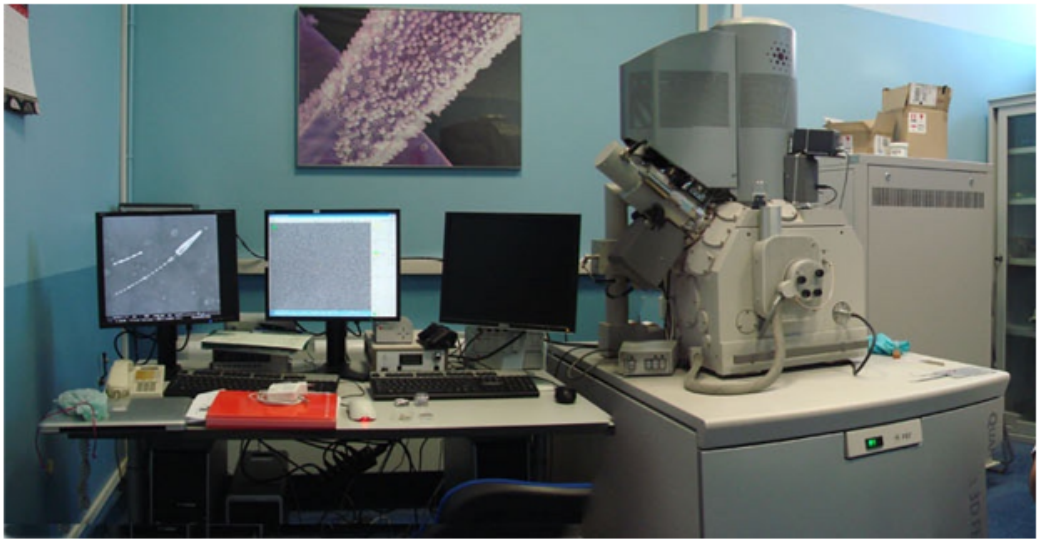

Fig. 6.5 Image of the FEI Quanta 3D FEG used for the fabrication of the proposed modified AFM tip at the QR laboratories at INRiM.

The Dual Beam microscope was equipped with a nanomanipulator (*MM3A-EM Kleindiek Nanotechnik*) and a gas injector for silicon oxide deposition with $SiC_8H_{20}O_4$ as precursor. In order to properly manipulate the nanodiamonds, the nanomanipulator's end was thinned by means of a Focused Ion Beam, since the typical nanodiamond lateral dimensions were around 500 nm, see Fig 6.5a. Afterward, the nanodiamonds chosen previously with the PL scan were picked up by gluing them to the nanomanipulator, by SiO_x local deposition see Fig 6.6. It is worth to notice that this process may occur in two possible ways: electrostatically or by means of silicon oxide deposition. In both cases, the chosen nanodiamond has been approached by the nanomanipulator until it was in contact with it. In this situation, when the electrostatic catching did not occur, a few nanometers (around 10-20 nm) of silicon oxide have been deposited to stick the nanodiamond to the nanomanipulator. This procedure has been performed by introducing the above-mentioned silicon precursor in the vacuum chamber, while the oxidation was induced by introducing air with a needle valve until reaching a 10^{-4} mbar pressure (starting from 10^{-5} mbar). The nanodiamond was then carried in close proximity to the AFM tip and carefully placed above the top of the tip. At this point, the nanomanipulator was finely moved down until the nanodiamond was in contact with the AFM tip and glued on top of it by SiO_x local deposition. In order to detach the nanodiamond from the nanomanipulator FIB cutting was used. We exploited the FIB etching also to

reshape the nanodiamond since a sharp end is more desirable for a precise scan of the hyperbolic metasurfaces. The final result of the fabrication process is reported in Fig 6.6b:

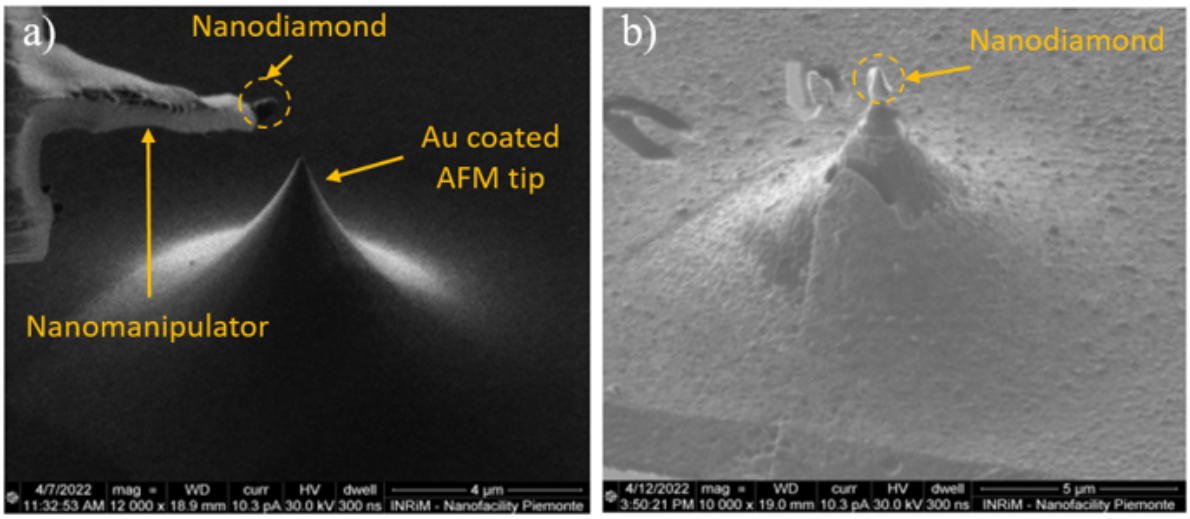

Fig. 6.6 (a) SEM image of the thinned nanomanipulator carrying the nanodiamond towards the AFM tip. (b) SEM image of the reshaped nanodiamond placed on top of the tip.

The modified tip was then observed under the fluorescence microscope to determine whether the nanodiamond on the modified AFM tip still preserved the same emission spectrum or not. Moreover, with this measurement, we can determine if the fabrication process was performed correctly without losing the emitting region of the nanodiamonds during the FIB etching and SiO_x local deposition. The results of the PL measurements after the fabrication are reported in the following figures:

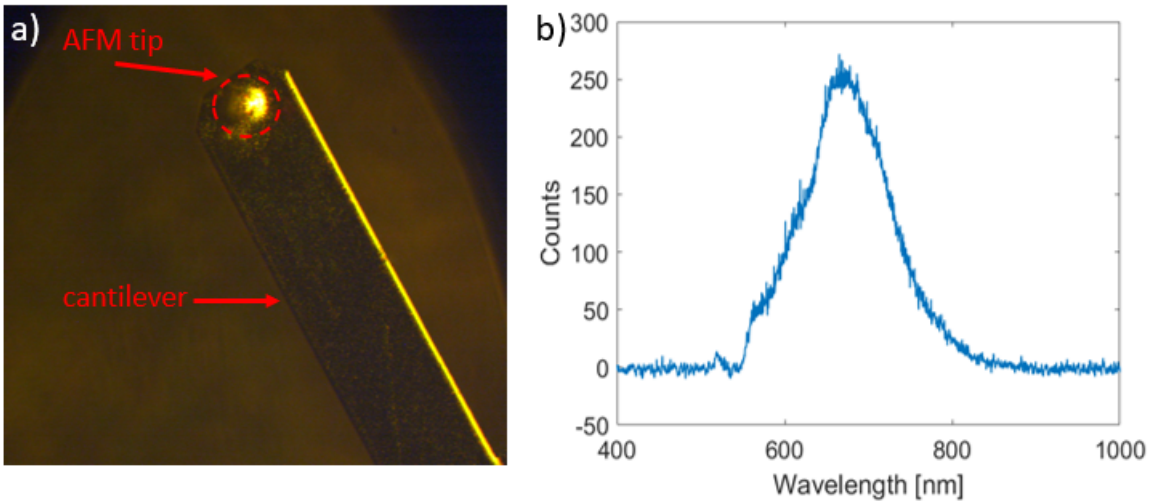

Fig. 6.7 (a) Wide-field white light image of the cantilever superimposed to the fluorescence image of the modified tip. b) Fluorescence spectrum collected from the AFM tip excited by the 520 nm laser.

Fig. 6.7a shows a white light image of the cantilever superimposed with the fluorescence image of the tip. The corresponding spectrum is reported in fig. 6.7b. From Fig 6.7b, it is clear that the fabrication process has led to the fabrication of an AFM tip with an emitting nanodiamond on top of it. Indeed, the acquired spectrum is the typical spectrum reported for the NV centers in diamonds, and it is comparable to the ones measured before the nanomanipulation process. Hence, we can conclude that the fabrication method described did not affect the characteristic spontaneous emission of NV centers in nanodiamonds.

In the following section, we will describe in more detail the proposed method to perform near-field characterization by means of the fabricated diamond-based nano-probe. Then, we will discuss the results acquired with the proposed modified AFM tip on a hyperbolic metasurface.

6.3 Optical characterization with the diamond-based nano-probe

After the fabrication of the diamond-based nano-probe, we exploited this tool to perform a near-field characterization of a hyperbolic metasurface. The sample used for this kind of analysis was the uniform sample with a height gradient shown in the previous chapters. In Fig 6.8, we report the near-field characterization setup exploited during our investigations in collaboration with the National Physical Laboratory:

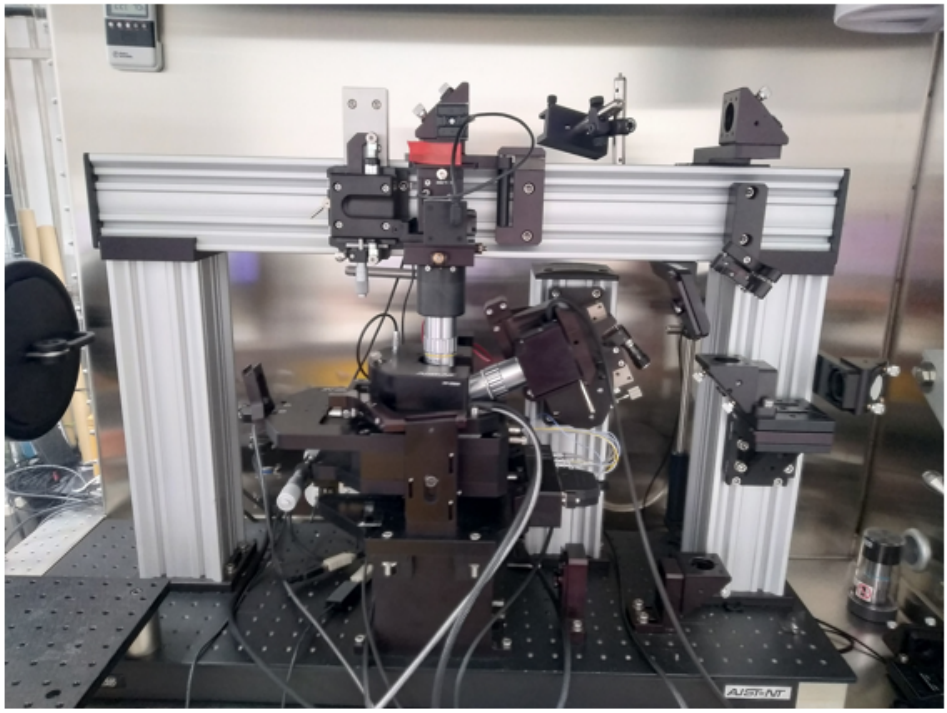

Fig. 6.8 Picture of the experimental setup used during the surface morphology and tip optical spectroscopy performed with the diamond-based nano-probe at the National Physical Laboratory (NPL) in Teddington (UK).

Fig 6.8 shows the Atomic Force Microscopy that was equipped with an AIST-NT Combiscope 1000 instrument. Surface topography measurements were carried out in non-contact mode using a BudgetSensors Tap300Al-G probe, with a nominal force constant of 40 Nm^{-1} and resonant frequency of 300 kHz.

For what concerns the tip optical spectroscopy, it was performed using the above-mentioned Combiscope 1000 with the TRIOS configuration, which provides an

optical access for side-illumination at an angle of 32° from the sample plane. For these measurements, the custom probe was used and optically excited using laser excitation with a wavelength of 532 nm and a 100× 0.7 NA Mitutoyo objective. The photoluminescence signal from the nanodiamond NV centers was collected in back-scattering mode by a HORIBA LabRam HR Evolution spectrometer using a 300-lines mm^{-1} grating. The laser power used was 0.5 mW, and the acquisition time was 5 s. In the tip optical spectroscopy, spectra were acquired as a function of tip-sample distance by removing the AFM feedback and moving the sample piezoelectric actuator to control the separation.

We have characterized firstly the hyperbolic metasurface performing AFM measurements with the above-mentioned BudgetSensors standard tip to analyze its topography. We report the obtained results in the following figure:

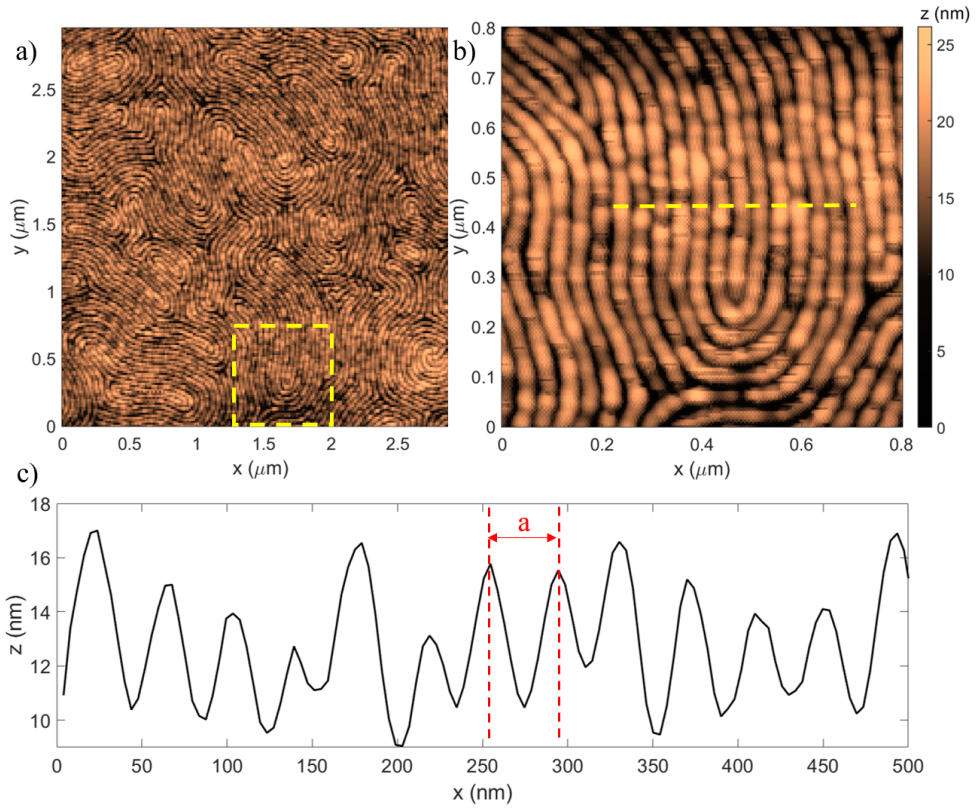

Fig. 6.9 (a) Atomic Force Microscopy images of the hyperbolic metasurface analyzed by means of the tip optical spectroscopy. (b) Zoom of the dashed yellow square in Fig 6.9a. (c) Linear profile along the yellow dotted line in Fig 6.9b.

In Fig 6.9a the morphology of the nanopatterned metasurface can be observed. Moreover, several grain boundaries are visible in the image and the correlation length that characterized the pattern is on the order of a few microns. In order to highlight the achieved degree of order, the region marked by the yellow dashed square has been zoomed in fig 6.9b. We have extracted a linear profile along the yellow dotted line reported in Fig 6.9b to precisely evaluate the periodicity of the nanostructured lamellae. The measured average period was equal to $a = (39 \pm 2)$ nm. The value is comparable with the lateral size equal to 19 nm for this sample reported in Methodologies chapter. Unfortunately, it was not possible to properly assess the height of the gold lamellae, and the fill factor exploiting this kind of measurement since the used AFM tip had a size that is comparable to the pattern and therefore it cannot fully penetrate into the lamellae air gaps.

After the characterization of the sample morphology, the diamond-based tip has been used to probe the spontaneous emission enhancement related to the coupling to the hyperbolic metasurface. To do so, we have continuously acquired the fluorescence spectrum from the diamond-based nano-probe while vertically approaching the sample surface to the tip. The acquired spectra are reported in Fig 6.10:

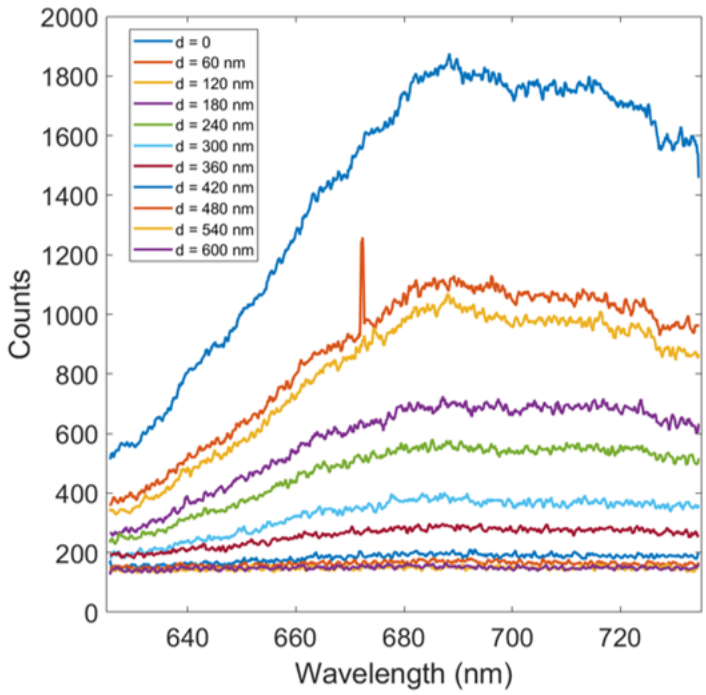

Fig. 6.10 Acquired spectra of the modified AFM tip photoluminescence during the vertical approaching.

In Fig 6.10 we have reported the fluorescence spectra acquired at different distances from the sample surface. It is clear that an enhancement of the fluorescence signal can be observed as the nano-probe gets closer to the hyperbolic metasurface. We have integrated the intensities along the measured wavelength range ($625nm < \lambda_0 < 735nm$) in order to extract the spontaneous emission enhancement profile as a function of the distance from the surface, see fig 6.11.

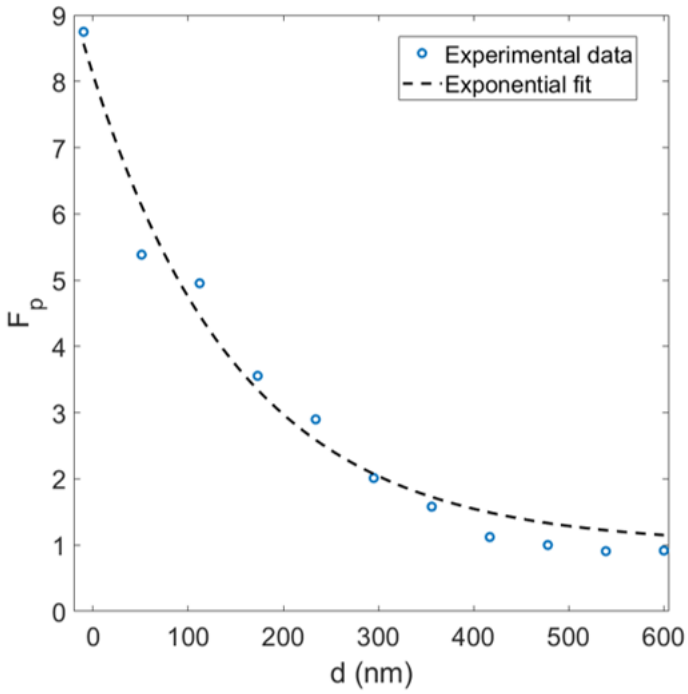

Fig. 6.11 Measured Purcell Factor as a function of the distance from the surface.

The Purcell Factor (Fp) has been computed as:

$$F_P = \frac{I_{HMM}}{I_0} \tag{6.2}$$

Where I_0 the average intensity of the last 2 spectra related to the flat part of the profile and I_{HMM} the intensity measured during the vertical approaching. As reported in the simulations' results, the measurements performed using the diamond-based probe confirmed the exponential enhancement of the fluorescence intensity following

Eq 6.1, with the following fitting parameters: $F_P(0) = 7.1$ and $d_0 = 156$ nm. It is worth to notice that in this case, the resulting decay length is larger than the calculated one ($d_0 = 35.65$ nm). This discrepancy can be explained by considering the fact that the emitting NV centers in the nanodiamond are distributed along the whole nanocrystal, hence what we have measured is an average enhancement weighted over all the defects. From the results reported in this Chapter, we believe that by reducing the diamond size it would be possible to increase the spatial resolution, especially in the out-of-plane direction, thus providing a tool to probe the local density of optical states of planar photonic devices such as the proposed hyperbolic metasurface.

In the next Chapter, we will discuss the future perspectives for the characterization and development of self-assembled hyperbolic metamaterials.

Chapter 7

Future Perspectives

In this Chapter, we discuss the future perspective of the presented research. We will discuss in more detail the opportunity to use different techniques for the fabrication and optical characterization of self-assembled hyperbolic metamaterials for the enhancement of SPS spontaneous emission. The Chapter is divided into three sections: fabrication of highly ordered lamellae in larger micrometric domains, an alternative self-assembled hyperbolic metamaterial, and future optical analyses of the hyperbolic metasurfaces.

7.1 Fabrication of highly ordered lamellae in larger micrometric domains

We decided to investigate a fabrication method to obtain highly ordered lamellae in large micrometric area since the dimensions of the highly ordered lamellae domains can affect the coupling with SPS, as reported in the Hyperbolic Metasurface Characterization Chapter. In collaboration with the University of Warsaw, we are analyzing an alternative fabrication process exploiting a Soft-shear Laser Zone Annealing process (SS-LZA) to order BCPs [152, 153].

In the following figure we report the setup for the SS-LZA process:

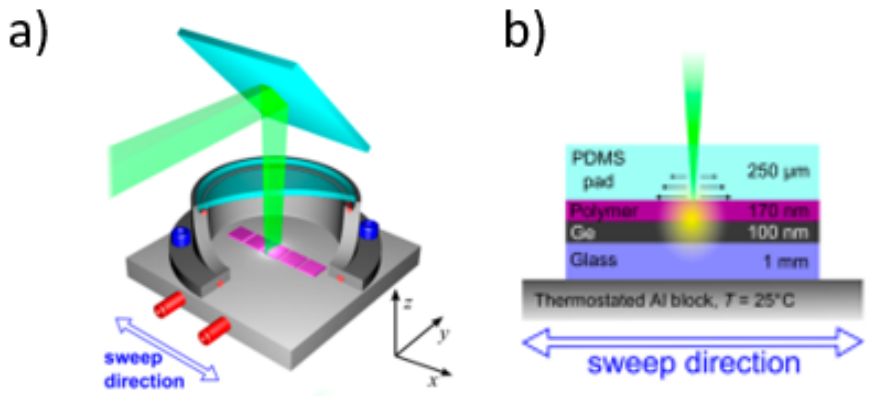

Fig. 7.1 (a) SS-LZA setup schematically reported. (b) A sketch of the sample with the region in which the annealing occurs locally highlighted in yellow [152].

From Fig 7.1, we can observe how the SS-LZA works. A temperature gradients is introduced by a 3 W power laser (Melles Griot 85 GHS 309) beam focused on a sample placed on a motorized motion stage (Newport ILS 250CC) inside a vacuum chamber with a thermostated sample holder baseplate to control the substrate temperature and optimize the quality of the BCP alignment. The laser beam is shaped into a narrow line by a set of lenses (two spherical lenses and one cylindrical) reaching a 20 μm full-width at half-maximum (FWHM) at the film surface. The sample is a glass substrated coated with 100 nm of germanium. This layer absorbs the light and enables larger temperature gradients (typically 270 °C) that locally anneal the BCPs inducing their self-assembling. For our purpose, a 0.5 mm thick PDMS layer will be placed on top of the sample to enhance the shear forces due to the difference in the thermal expansion coefficient between the polymer film and the substrate. Indeed, it has been demonstrated that by moving the sample shear forces can cause a stress in the laser sweep direction. Therefore the BCPs will result to be aligned in the same direction [152], see Fig 7.2. After the SS-LZA, the PDMS can be peeled off without residuals on the BCP films.

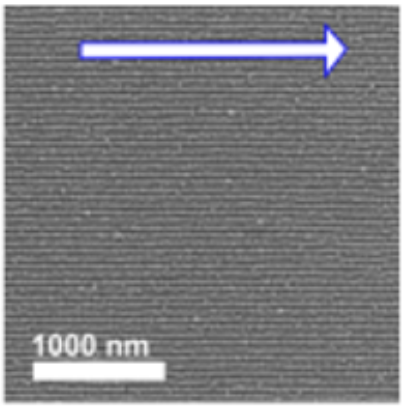

Fig. 7.2 SEM image of a micrometric domain with highly ordered BCPs that can be achieved with the SS-LZA technique [152].

It is worth to notice that with the proposed alternative fabrication method we have control over annealing conditions by tuning the laser power or focus and controlling the sample motion.

In addition, the proposed technique can be combined to other techniques in order to achieve the desired lamellae height. For example, by using a sequential infiltration technique a polymer phase can be converted into a metal oxide [156, 157]. Afterward, Reactive Ion Etching (RIE) can be performed to create a lamellar template with the desired height by tuning the etching parameters. In this way, we can obtain the hyperbolic metasurface with highly ordered lamellae on a transparent substrate by means of the peeling technique mentioned in the Methodologies Chapter.

7.2 An alternative self-assembled hyperbolic metamaterial

To enhance the spontaneous emission of the single-photon sources, we investigated the opportunity to exploit an alternative hyperbolic metasurface. The considered alternative HMM was composed of gold cylinders in a PS matrix. We considered gold cylinders in a PS matrix since they can be fabricated and ordered in a large uniform area with respect to the lamellae in a more direct way. In order to fabricate the periodic nanostructures, self-assembling BCPs have been used also in this case. The samples have been fabricated by self-assembly process of PS-b-PMMA BCPs

with M_w = 82 kg mol^{-1}, polydispersity index (PDI) = 1.06, f_{PS} = 69.5% (wt/wt). As reported for the lamellar nanostructures, random copolymer grafting process has been performed for the neutralization of a Si substrate. During this process we used PS-r-PMMA as random copolymer with M_n = 19.93 kg mol^{-1}, f_{PS} = 59.0% (wt/wt) and PDI = 1.13. After the deposition of cylindrical forming BCPs, the self-assembling process was induced thermally in RTP at 190 °C for 450 s in N_2 environment. The PMMA removal has been performed as described for the lamellar nanostructures: an isotropic O_2 plasma treatment to etch the PMMA previously exposed to ultraviolet radiation. Then, an electrodeposition process at 2.5 mA for 600 s has been used to deposit gold into the cylindrical template. Indeed, electrodeposition allows the growth of nanometric features of metals into solid templates. Here, we report schematically the fabrication steps:

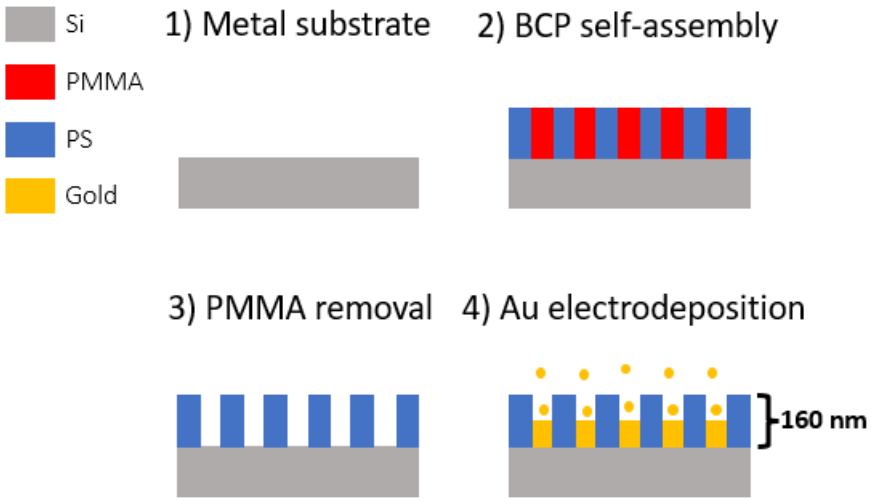

Fig. 7.3 Sketch of the fabrication steps necessary to obtain gold cylinders in a PS matrix

As can be seen Fig 7.4a, the electrodeposition process leads to an incomplete deposition inside the cylindrical template.

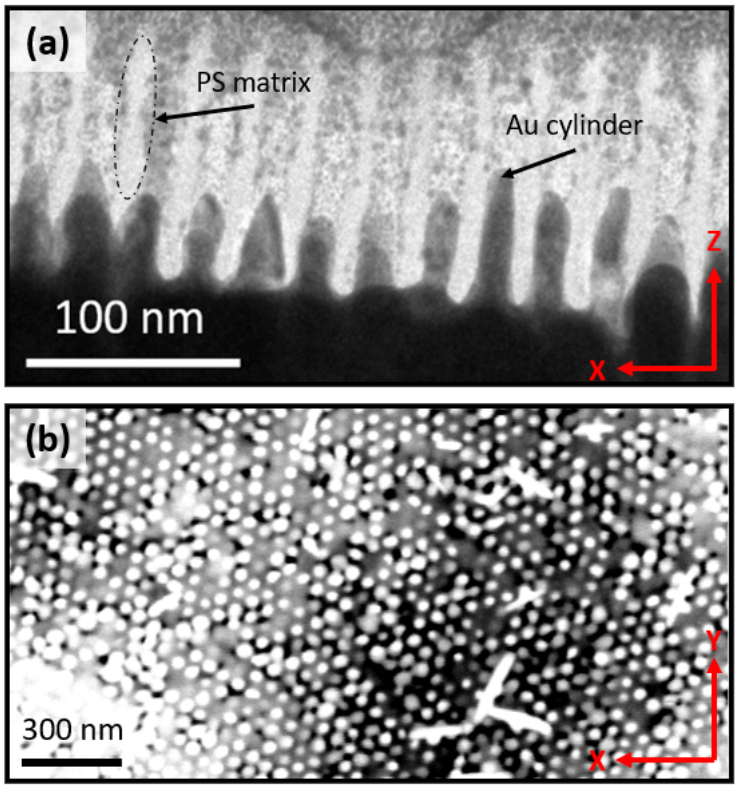

Fig. 7.4 (a) Cross-section TEM view of the cylindrical BCP template after gold electrodeposition (b) SEM image of the top-view of the cylindrical template reported in (a).

As done for the lamellar nanostructures, the optical behavior of the gold cylinders in a PS matrix has been investigated by means of a modal analysis and studying the acquired spectra of the NV centers emission coupled with the HMM. For what concerns the modal analysis we have performed the calculations for cylinders with a 15 nm diameter and 70 nm height.

From Fig 7.5, we can see that a sustained mode is present in the wavelength range between 570 nm and 610 nm. It is worth to notice that as reported for the lamellae a stationary mode is present.

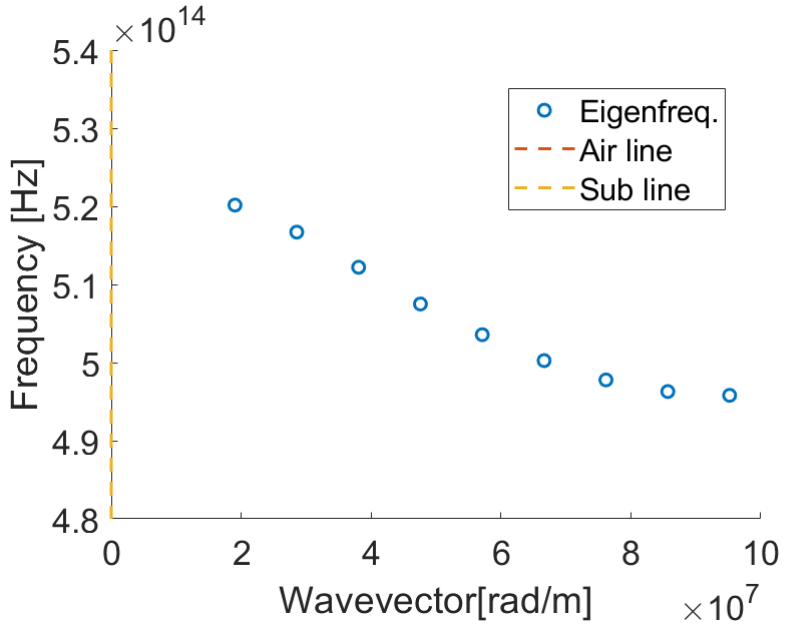

Fig. 7.5 Modal analysis result for the gold cylinders in a PS matrix.

Regarding the study of the emitted spectra of NV centers coupled with the HMM, we performed the measurements with the setup reported in Fig 4.14. Here we report the results for two different emitting nanodiamonds:

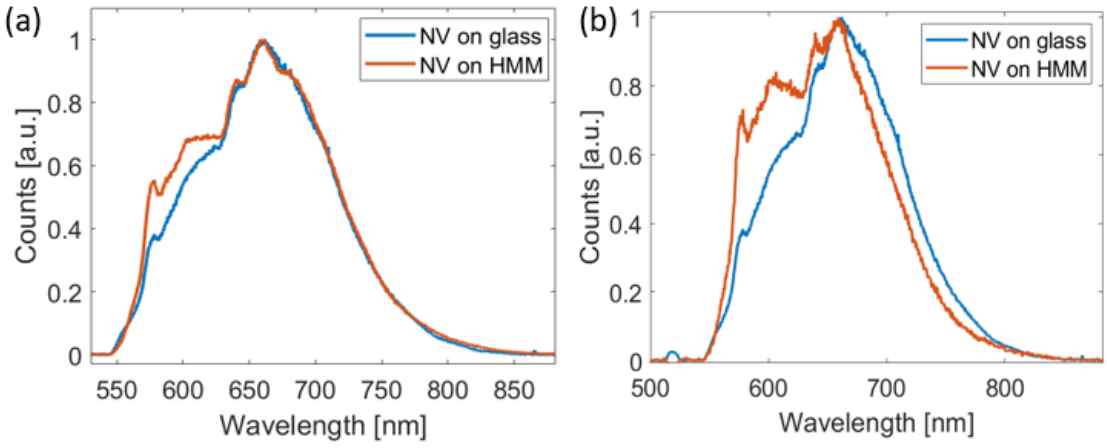

Fig. 7.6 Examples of two acquired PL spectra of NV centers in nanodiamons on the proposed HMM, orange line. The spectra are compared to the emission of nanodiamonds on a glass substrate, blue line.

From Fig 7.6, it is clear that the spectrum of the defects coupled to the metasurface shows different features with respect to the emitting nanodiamonds on a glass

substrate. Also for the gold cylinders, an emerging broad peak can be observed between 570 nm and 630 nm, hence in the same range of the sustained mode found in the previous modal analysis.

After the acquisition of the PL spectra, we have performed a time-resolved photoluminescence decay measurement to estimate the lifetime value related to the NV centers coupled with the hyperbolic metasurface, see Fig 7.7.

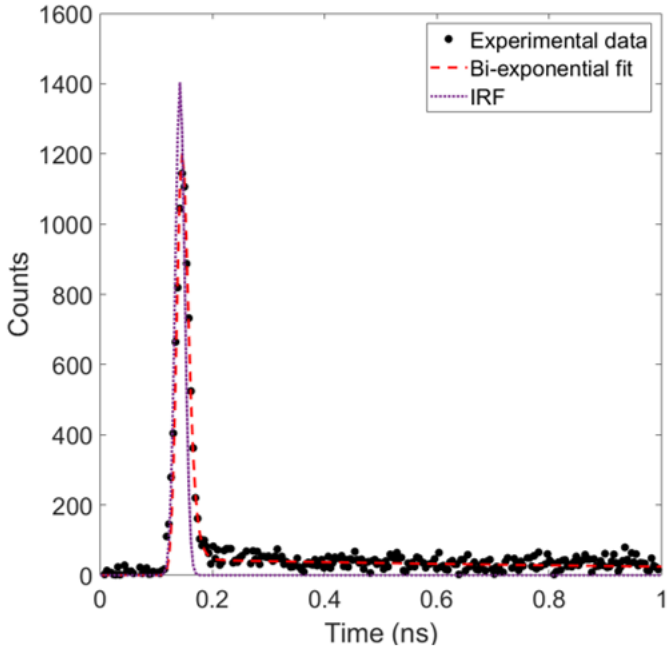

Fig. 7.7 Intensity decay for the emission measured on NV centers on the HMM.

As performed for the lamellar nanostructures, we exploited a bi-exponential function to fit the decay. From the bi-exponential behavior we extrapolated a lifetime value equal to 23 ps that is lower with respect to the typical 12 ns value reported in literature [144] and comparable with the laser pulse ($\sim 27ps$). Hence, we can conclude that the NV centers emission rate was enhanced by coupling the emitters with the hyperbolic metasurface based on gold cylinders in a PS matrix. In this way, we demonstrated that an alternative self-assembled hyperbolic metamaterial can be used to enhance and tune the spontaneous emission of single-photon sources for quantum optics applications.

7.3 Future optical analyses of the hyperbolic metasurfaces

7.3.1 Evaluation of the $g^{(2)}(\tau)$

After considering the fabrication of hyperbolic metasurfaces with different features as the ones reported in the previous sections, further optical characterizations of the proposed systems coupled to NV centers in nanodiamonds are needed to understand how the HMM affects the single-photon nature of the emitters. For this reason, the next step will be represented by measurements for the evaluation of the $g^{(2)}(\tau)$. In this way, it will be possible to observe how the lamellae affect the single-photon nature of the emitters, in particular the highly ordered lamellae.

In order to evaluate the $g^{(2)}(\tau)$ for emitters coupled with the proposed hyperbolic metasurfaces, a Hanbury-Brown-Twiss (HBT) interferometer will be necessary. We report the scheme of the HBT interferometer that we intend to exploit in the following figure:

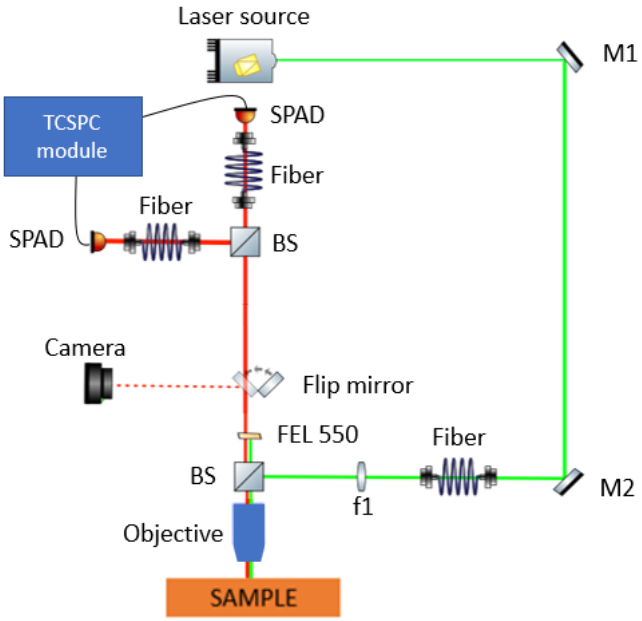

Fig. 7.8 Setup for the $g^{(2)}(\tau)$ evaluation

The reported setup is almost identical to the PL setup discussed in the Methodologies Chapter, see Fig 4.14. They are different only in the part after the flip mirror. In this case, the acquired fluorescence is directed by a beam splitter toward two Single-Photon Avalanche Diodes (SPADs of PDM series purchased from PicoQuant), instead of the previous spectrometer. In this way, the detectors allow the opportunity to perform coincidence measurements thanks to their detection electronics (Time-Correlated Single Photon Counting (TCSPC) module PicoHarp 300). To perform such measurements one of the SPADs acts as a start and the other as a stop while their electronics module measures the delay between the signals. Then, the TCSPC module generates a histogram of the measured delay times counting the number of detected photon pairs. From the measured histogram, an antibunching curve is expected to emerge, as the one reported in Fig 1.1. Afterward, by extrapolating the antibunching curve and by means of a fitting process, it is possible to evaluate the related $g^{(2)}(\tau)$. During the TCSPC measurements, we expect to observe and quantify $g^{(2)}(\tau)$ values below 0.5 for nanodiamonds coupled to the hyperbolic metasurfaces confirming and keeping the single-photon source nature.

7.3.2 Further measurements with improved diamond-based nano-probe

In order to perform further characterization of the enhancement induced by the HMMs, we will exploit also an improved diamond-based nano-probe we discussed in the previous chapter. As improvement of the presented solution, 240AC-NA AFM tips (nominal force constant of 2 Nm^{-1}, resonant frequency of 70 kHz) purchased from OPUS will be exploited for the fabrication process of the optical nano-probe. Using OPUS tips exciting the emitting nanodiamond with the 532 nm laser would be simpler and more efficient since they are characterized by a tip end that is at the end of the cantilever, as reported in the following figure:

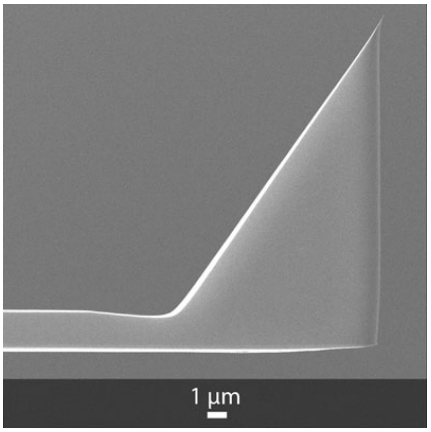

Fig. 7.9 Image of the 240AC-NA AFM tip end purchased from the OPUS website

Hence, it will be possible to obtain a stronger PL signal with respect to the previous AFM tip used for the nano-probe fabrication. After the improvement of the nano-probe, we intend to perform the optical near-field characterization on the samples that were not investigated in the reported measurements and have highly ordered lamellae such as samples with dewetted droplets, unpatterned samples with highly ordered lamellae, and the samples presented in the previous sections. With the samples characterized by lamellae arranged in a few micrometric domains, we expect to observe the narrowband peak found in the PL and lifetime measurements emerging while vertically approaching the probe to the surface. Moreover, as mentioned in the previous Chapter, we will perform a scan of the surface while acquiring the fluorescence spectrum in order to estimate the regions with higher spontaneous emission enhancement and relate the amplification to the surface topography of the same analyzed region.

Chapter 8

Conclusions

In this Thesis, we have presented a study that was aimed at the development of self-assembled hyperbolic metamaterials for the enhancement of single-photon sources. By exploiting the fabrication process of the self-assembling BCPs described in the Methodology Chapter, we have shown how to produce periodic nanostructures in order to obtain a hyperbolic metasurface with the in-plane optical axis: air/gold lamellae. From the results reported in this Thesis, we have observed that the proposed hyperbolic metasurface can be used as a platform to tune and enhance the spontaneous emission of NV centers in nanodiamonds. Indeed, we have observed the presence of stationary modes in the modal analysis and an effective feedback mechanism that determines a pseudo-cavity and consequently leads to emission enhancement in the wavelength range around the estimated stationary modes. Moreover, by means of the simulation model, we estimated the Purcell factor behavior finding narrowband peaks in the wavelength range where the effective feedback mechanism can occur. We showed that the optical response can be tuned by simply controlling the lamellae height. To verify the estimated results, we have then characterized experimentally the fabricated samples by using NV centers in nanodiamonds as single-photon sources. We have found out that the NV center emission was modified in a broad wavelength range when the emitters are coupled to the proposed hyperbolic metasurface. In particular, with a few micrometric domains of highly ordered lamellae, it is possible to enhance a specific narrow range of wavelengths that is comparable with the narrowband Purcell factor peak estimated in the simulations. Moreover, by fluorescence lifetime spectroscopy, a strong reduction of the lifetime value was measured confirming that the photon emitters coupled to hyper-

bolic metasurface modify the dynamics of their spontaneous emission process due to the higher local density of optical states (LDOS) associated with the hyperbolic dispersion relation. Unfortunately, with the previous measurement techniques, a direct estimation of the LDOS enhancement was not possible, hence we proposed the fabrication of a diamond-based nano-probe for near-field characterization: an AFM tip with an emitting nanodiamond on top of it. The proposed method consisted of an AFM setup with the opportunity to perform tip-enhanced optical spectroscopy with the modified AFM tip. From the estimation of the optical response of the proposed modified AFM tip we expected to observe a clear exponential dependence of the enhancement on the vertical distance from the hyperbolic metasurface during the measurements. The measured enhancement had a similar exponential behavior as reported in the calculations but with a different decay length. This can be due to the fact that we measured an average enhancement weighted over all the emitting defects, including the defects that are not coupled to the metasurface. Finally, we discussed the future perspectives of the presented research. We presented a technique based on self-assembling BCPs Laser Zone Annealing to obtain highly ordered lamellae in larger domains since the reported results suggested that with this kind of samples it is possible to enhance the spontaneous emission in a narrowband region. We also analyzed the opportunity to enhance the single-photon sources with another hyperbolic metamaterial: gold cylinders in a dielectric matrix. After describing their fabrication process, we showed that a modification of the emitted spectrum can occur with this hyperbolic metamaterial. Moreover, the cylinders in a dielectric matrix have the advantage of being more uniform on the sample surface and their height can be controlled more precisely. Then, we focused our attention on possible further optical analyses. To understand how the HMM affects the single-photon nature of the emitters, we discussed the setup for the evaluation of the $g^{(2)}(\tau)$. To evaluate the enhancement due to the increase of the available optical states, we considered an improved diamond-based nano-probe for the tip optical spectroscopy that will be performed on the samples that were not characterized in this Thesis.

In conclusion, we presented an innovative method to enhance and tune the spontaneous emission of single-photon sources by means of self-assembled hyperbolic metasurfaces and a technique for the evaluation of the emission enhancement through a diamond-based nano-probe. These are fundamental steps for the development of the necessary building blocks for the implementation of photonic devices for quantum applications. Nonetheless, further investigations are needed in particular for

what concerns the fabrication of highly ordered lamellae in a large area with a fine control and regarding the measurements to quantify how the hyperbolic dispersion relation affects the spontaneous emission dynamics of the single-photon sources.

Appendix A

Focus on lamellae with diamond as dielectric

In this appendix, we show the simulations results regarding another possible hyperbolic metasurface: diamond/gold lamellae. Indeed, during our investigations we have considered other possible materials for our HMM. In particular, we have focused our attention on the possibility to use diamond as dielectric in the lamellar structure since it may represent a simple way to implement a hyperbolic metasurface with photon emitter inside it. This could be possible by ion implantation as the depth of implantation can be finely tuned. For this reason, in this case we have simulated a lamellar structure made of diamond and gold with the previous periodicity (38 nm) but above a diamond substrate and the dipole placed 5 nm beneath the hyperbolic metasurface in a 5 μm radius domain. The refractive index used for the diamond was n=2.4. Also in this case we have estimated the electric field distribution performing a frequency sweep between 500 nm and 800 nm. Moreover, we have also studied the effects of the lateral position (along X axis) of the dipole on the spontaneous emission enhancement. To do so, we have swept the material inside the lamellar structure in order to simulate a lateral movement. Hence, we simulated a model with the leftmost lamella in gold, and in the second case in diamond.

If we consider the first case, we can see from Fig A.1 that the radiation propagates along the metasurfaces also in this case. This can be considered as a clue of the efficient coupling between the sustained mode by the HMM and emission of the dipole.

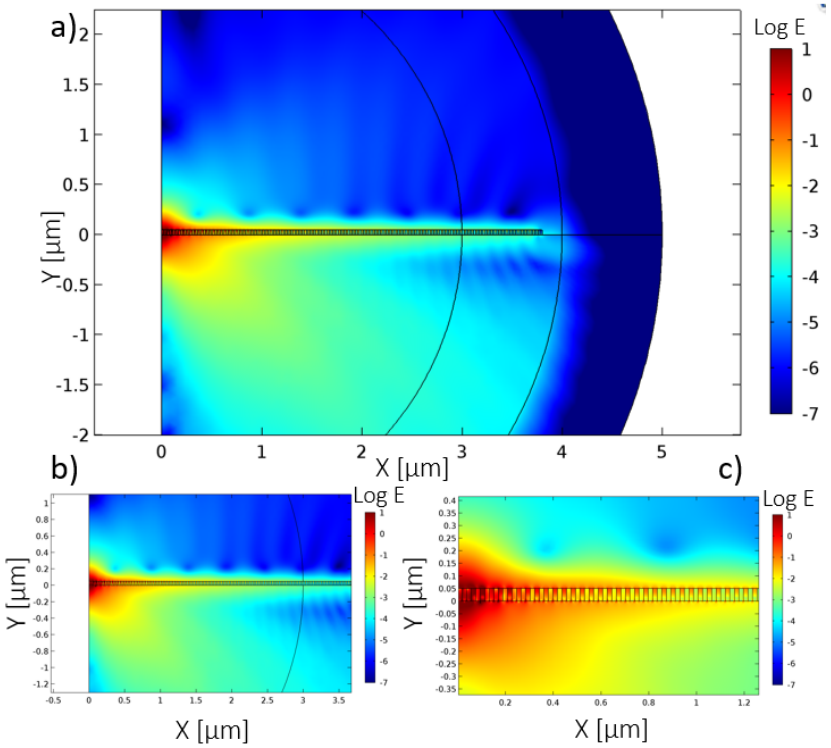

Fig. A.1 (a) Electric field distribution for a 50 nm high hyperbolic metasurface. (b-c) In the inset, it is clear that also in this case there is a coupling between the emission (dipole interacting first with gold at 780 nm wavelength) and the sustained mode.

In addition, we have estimated also the Purcell factor by varying the height of the lamellar structure with 2 nm steps from 20 nm to 64 nm. We report the results in the following figure:

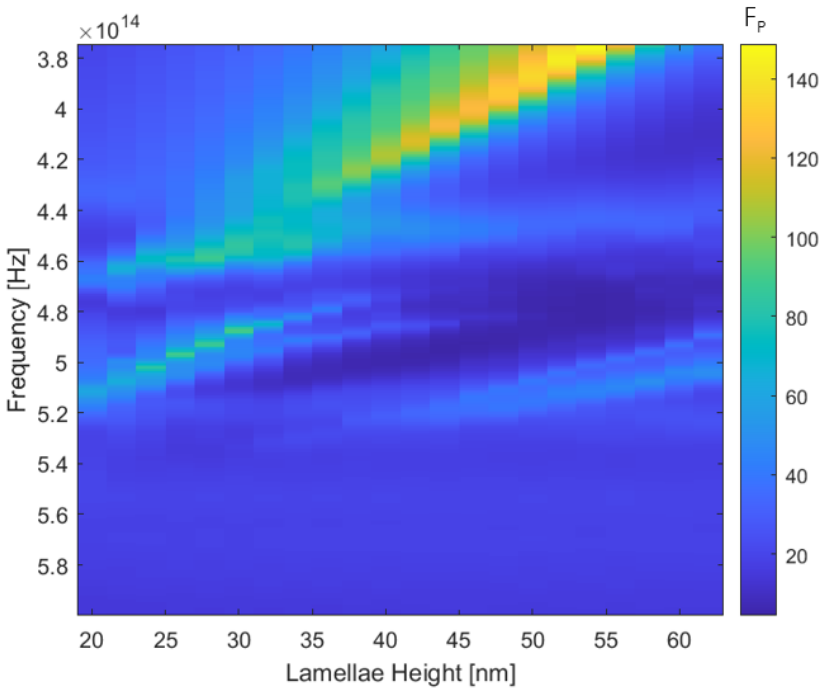

Fig. A.2 This map shows the Purcell factor values varying the lamellae height from 20 nm to 64 nm with 2 nm steps when the dipole interacts first with gold.

We can see that also in this case the Purcell factor peak has a redshift increasing the height of the hyperbolic metasurface, as reported for the gold/air lamellae. It can be also observed that the spontaneous emission enhancement values are higher with respect to the previous ones reported for the the gold/air lamellae. In particular, we obtain values around 100 even for small height values (from 24 nm to 36 nm). This is mainly due to the position of the emitter. Indeed it has been reported in the literature that higher enhancement can be reached by placing the photon emitter inside the HMM [46, 128].

For what concerns the second case, i.e. lefmost lamella in diamond, we report the electric field distribution in the following figure:

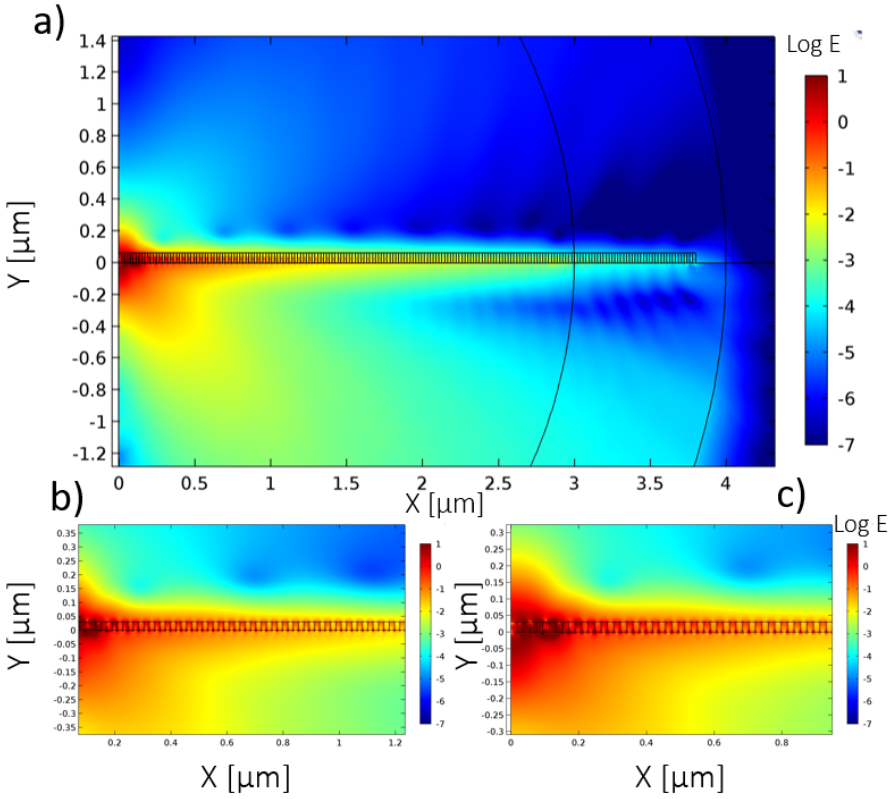

Fig. A.3 (a) Electric field distribution for a 30 nm high hyperbolic metasurface. (b-c) In the inset, it is clear that also in this case there is a coupling between the emission (dipole interacting first with diamond old at 660 nm wavelength) and the sustained mode.

Also in this case, the coupling between the emission and the sustained modes occurs even if with a slightly different distribution of the electric field. Furthermore, the most interesting thing occurs when we consider the Purcell factor for different lamellae height, see fig A.4.

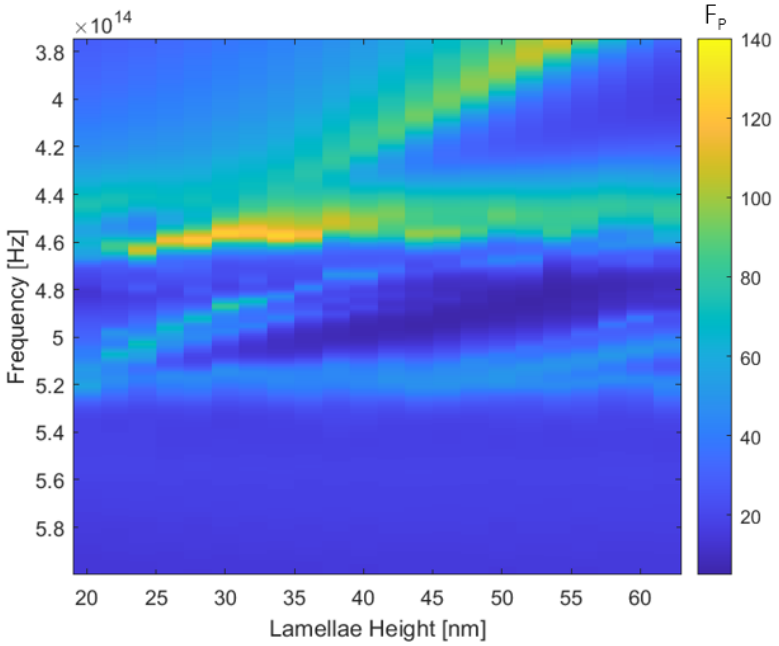

Fig. A.4 This map shows the Purcell factor values varying the lamellae height from 20 nm to 62 nm with 2 nm steps when the dipole interacts first with diamond

Indeed, we can see clearly that the Purcell factor peaks have values slightly lower the previous case and almost constant for heights between 24 nm and 36 nm. It is even more interesting the fact that by comparing the two maps, Fig A.2-Fig A.4, it seems that by laterally moving the dipole it is possible to *"switch on or off"* one of the spontaneous emission enhancement peak. Hence, for a hypothetical uniform layer of emitters in the lamellar structure we would expect to measure an average between the two maps.

As further step in the characterization of the proposed hyperbolic metasurface, we have chosen a specific height for the two cases and performed a simulation by varying the refractive index of the upper domain (starting from air so n=1) in order to analyze possible different optical response in the two Purcell factor peaks.

Here, we report the results for the leftmost lamella in gold and a 50 nm high hyperbolic metasurface:

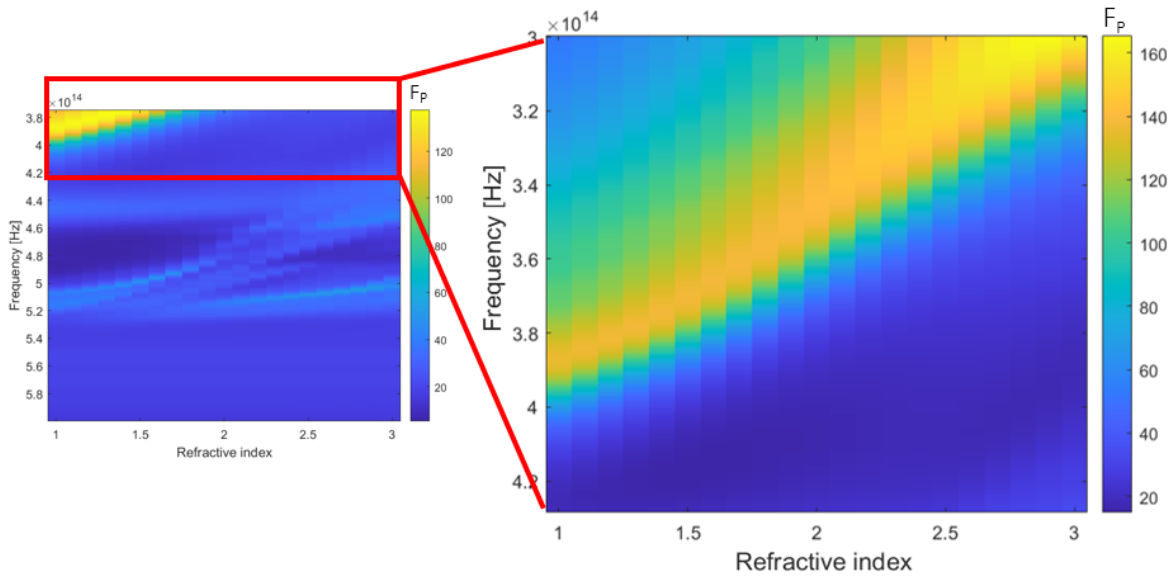

Fig. A.5 Here we report the map of the Purcell factor values for a dipole interacting first with gold and coupled to a 50 nm high hyperbolic metasurface by varying the refractive index of the upper domain. In this case, we can see clearly that the system becomes more sensitive in the NIR region.

We can see very clearly that the refractive variation of the upper domain causes a further redshift of the Purcell factor peak that we estimated to be 5 nm for every 0.1 refractive index variation.

In the other case, i.e. leftmost lamella in diamond, we have considered a 30 nm high HMM for the evaluation of the Purcell factor peak dependence on the refractive index of the upper domain. We found out a very different behavior for the considered case. Indeed, we have obtained a Purcell factor peak that does not seem to be affected in terms of frequency by the variation of the refractive index in the upper domain, but it simply fades as it can be observed in fig A.6:

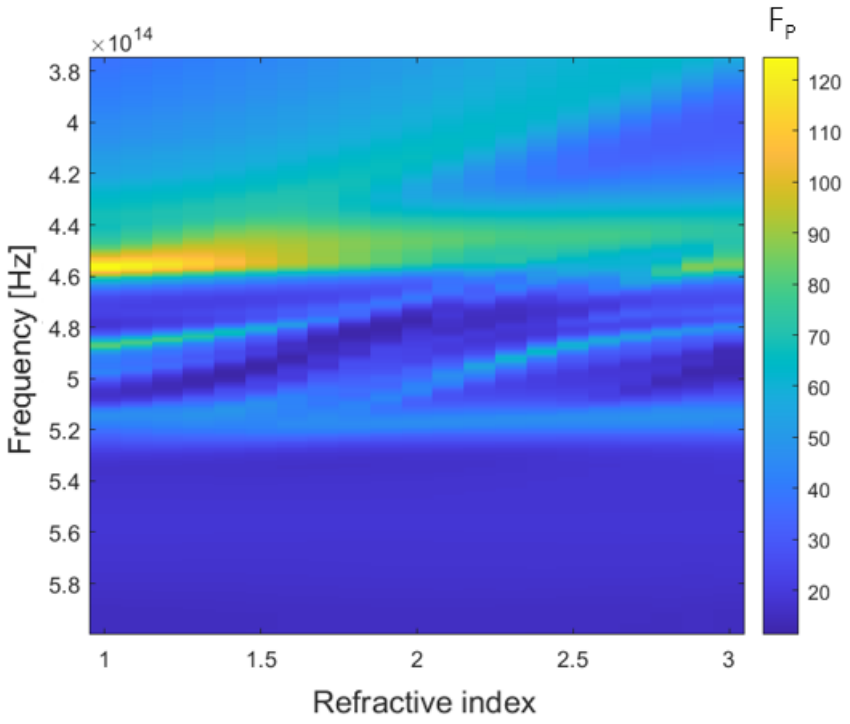

Fig. A.6 Here we report the map of the Purcell factor values for a dipole interacting first with diamond and coupled to a 30 nm high hyperbolic metasurface by varying the refractive index of the upper domain.

It is worth to notice that this kind of structure has appealing properties for applications in which the response must be stable for refractive index changes of the domain with which the hyperbolic metasurface interfaces. We can conclude that for the diamond/gold lamellae the emission enhancement is almost not affected in terms of frequency by the refractive index of the upper domain material, particularly for the last case considered, i.e. leftmost lamella in diamond.

In conclusion, with the reported simulations in this appendix we have shown how the optical response of the hyperbolic matesurface composed of nanostructured lamellae can be modified and controlled by choosing a different dielectric. With diamond as dielectric, the enhancement is not only tuned but also theoretically improved for low height values with respect to the air/gold lamellae. This is mainly due to the position of the emitters that can be placed inside the diamond for the proposed hyperbolic metasurface.

References

[1] Eisaman, Matthew D., et al. "Invited review article: Single-photon sources and detectors." Review of scientific instruments 82.7 (2011): 071101.

[2] Silitonga, Parasian DP, and Sorang Pakpahan. "Application of Integers in Vernam Cipher Cryptography (One Time Pad)." INFOKUM 9.2, June (2021): 350-353.

[3] Leung, Debbie W. "Quantum vernam cipher." arXiv preprint quant-ph/0012077 (2000).

[4] Bennett, Charles H., and Gilles Brassard. "An update on quantum cryptography." Workshop on the theory and application of cryptographic techniques. Springer, Berlin, Heidelberg, 1984.

[5] Sviatoslav Ditalia Tchernij, ”Use of energetic ion beams for the engineering and control of quantum-optical emitters and sensors in artificial diamond”, 2019

[6] A. Beveratos, R. Brouri, T. Gacoin, A. Villing, J.-P. Poizat, and P. Grangier, “Single Photon Quantum Cryptography,” Phys. Rev. Lett., vol. 89, no. 18, p. 187901, Oct. 2002.

[7] Carrasco-Casado, Alberto, Verónica Fernández, and Natalia Denisenko. "Free-space quantum key distribution." Optical Wireless Communications. Springer, Cham, 2016. 589-607.

[8] Chunnilall, Christopher J., et al. "Metrology of single-photon sources and detectors: a review." Optical Engineering 53.8 (2014): 081910.

[9] Von Helversen, Martin, et al. "Quantum metrology of solid-state single-photon sources using photon-number-resolving detectors." New Journal of Physics 21.3 (2019): 035007.

[10] Bhargav, Anish M., et al. "Metrology Perspective of Single-Photon Detectors: Review on Global Calibration Methods." Advanced Quantum Technologies 4.10 (2021): 2100008.

[11] Grünwald, Peter. "Effective second-order correlation function and single-photon detection." New Journal of Physics 21.9 (2019): 093003.

[12] Lukishova, Svetlana. "Efficient single-photon sources with definite polarization." SPIE Newsroom (2014).

[13] Alléaume, Romain, et al. "Experimental open-air quantum key distribution with a single-photon source." New Journal of physics 6.1 (2004): 92.

[14] Kobayashi, Toshiya, Akihisa Tomita, and Atsushi Okamoto. "Evaluation of the phase randomness of a light source in quantum-key-distribution systems with an attenuated laser." Physical Review A 90.3 (2014): 032320.

[15] You, Chenglong, et al. "Multiparticle quantum plasmonics." Nanophotonics 9.6 (2020): 1243-1269.

[16] Couteau, Christophe. "Spontaneous parametric down-conversion." Contemporary Physics 59.3 (2018): 291-304.

[17] Christ, Andreas, et al. "Parametric down-conversion." Experimental Methods in the Physical Sciences. Vol. 45. Academic Press, 2013. 351-410.

[18] Christ, Andreas, and Christine Silberhorn. "Limits on the deterministic creation of pure single-photon states using parametric down-conversion." Physical Review A 85.2 (2012): 023829.

[19] Arakawa, Yasuhiko, and Mark J. Holmes. "Progress in quantum-dot single photon sources for quantum information technologies: A broad spectrum overview." Applied Physics Reviews 7.2 (2020): 021309.

[20] Brokmann, X., et al. "Colloidal CdSe/ZnS quantum dots as single-photon sources." New Journal of Physics 6.1 (2004): 99.

[21] Buckley, Sonia, Kelley Rivoire, and Jelena Vučković. "Engineered quantum dot single-photon sources." Reports on Progress in Physics 75.12 (2012): 126503.

[22] Schmidt, Marco, et al. "Deterministically fabricated spectrally-tunable quantum dot based single-photon source." Optical Materials Express 10.1 (2020): 76-87.

[23] Senellart, Pascale, Glenn Solomon, and Andrew White. "High-performance semiconductor quantum-dot single-photon sources." Nature nanotechnology 12.11 (2017): 1026-1039.

[24] K. F. Mak and J. Shan,"Photonics and optoelectronics of 2D semiconductor transition metal dichalcogenides", Nature Photonics 10, 216 (2016)

[25] O. Iff, et al. ,"Purcell-Enhanced Single Photon Source Based on a Deterministically Placed WSe2 Monolayer Quantum Dot in a Circular Bragg Grating Cavity", Nano Letters 21, 4715 (2021), pMID: 34048254.

[26] Y. Luo,et al.,"Deterministic coupling of site-controlled quantum emitters in monolayer WSe2 to plasmonic nanocavities" Nature Nanotechnology 13, 1137 (2018)

[27] M. Turunen,et al. „"Quantum photonics with layered 2D materials" Nature Reviews Physics 4, 219 (2022).

[28] Berthel, Martin, et al. "Photophysics of single nitrogen-vacancy centers in diamond nanocrystals." Physical Review B 91.3 (2015): 035308.

[29] Khramtsov, I. A., M. Agio, and D. Yu Fedyanin. "Kinetics of single-photon emission from electrically pumped NV centers in diamond." AIP Conference Proceedings. Vol. 1874. No. 1. AIP Publishing LLC, 2017.

[30] Sviatoslav Ditalia Tchernij, "Use of energetic ion beams for the engineering and control of quantum-optical emitters and sensors in artificial diamond", 2019, PhD Thesis

[31] Gruber, A., et al. "Scanning confocal optical microscopy and magnetic resonance on single defect centers." Science 276.5321 (1997): 2012-2014.

[32] Hong, Sungkun, et al. "Nanoscale magnetometry with NV centers in diamond." MRS bulletin 38.2 (2013): 155-161.

[33] Doherty, M. W., et al. "Theory of the ground-state spin of the NV center in diamond." Physical Review B 85.20 (2012): 205203.

[34] Schirhagl, Romana, et al. "Nitrogen-vacancy centers in diamond: nanoscale sensors for physics and biology." Annu. Rev. Phys. Chem 65.1 (2014): 83-105.

[35] Hopper, David A., Henry J. Shulevitz, and Lee C. Bassett. "Spin readout techniques of the nitrogen-vacancy center in diamond." Micromachines 9.9 (2018): 437.

[36] Gali, Adam. "Theory of the neutral nitrogen-vacancy center in diamond and its application to the realization of a qubit." Physical Review B 79.23 (2009): 235210.

[37] Zhang, Tongtong, et al. "Toward quantitative bio-sensing with nitrogen–vacancy center in diamond." ACS sensors 6.6 (2021): 2077-2107.

[38] Moreva, E., et al. "Practical applications of quantum sensing: A simple method to enhance the sensitivity of nitrogen-vacancy-based temperature sensors." Physical Review Applied 13.5 (2020): 054057.

[39] V. K. A. Sreenivasan, A. V Zvyagin, and E. M. Goldys, "Luminescent nanoparticles and their applications in the life sciences," J. Phys. Condens. Matter, vol. 25, no. 19, p. 194101, May 2013.

[40] Acosta, V. M., et al. "Optical properties of the nitrogen-vacancy singlet levels in diamond." Physical Review B 82.20 (2010): 201202.

[41] Luo, Tingpeng, et al. "Creation of nitrogen-vacancy centers in chemical vapor deposition diamond for sensing applications." New Journal of Physics 24.3 (2022): 033030.

[42] Cortes, C. L., et al. "Quantum nanophotonics using hyperbolic metamaterials." Journal of Optics 14.6 (2012): 063001.

[43] Shekhar, Prashant, Jonathan Atkinson, and Zubin Jacob. "Hyperbolic metamaterials: fundamentals and applications." Nano convergence 1.1 (2014): 1-17.

[44] Huo, Pengcheng, et al. "Hyperbolic metamaterials and metasurfaces: fundamentals and applications." Advanced Optical Materials 7.14 (2019): 1801616.

[45] Ahmadivand, Arash, and Burak Gerislioglu. "Photonic and Plasmonic Metasensors." Laser Photonics Reviews 16.2 (2022): 2100328.

[46] Mahmoodi, Maryam, Seyed Hassan Tavassoli, and Andrei V. Lavrinenko. "Mode-resolved directional enhancement of spontaneous emission inside/outside finite multilayer hyperbolic metamaterials." Materials Today Communications 23 (2020): 100859.

[47] DaSilva, Ashley M., et al. "Enhancement of photonic density of states in finite graphene multilayers." Physical Review B 88.19 (2013): 195411.

[48] Wang, Yu, et al. "Broadband enhancement of local density of states using silicon-compatible hyperbolic metamaterials." Applied Physics Letters 106.24 (2015): 241105.

[49] Shalaginov, Mikhail Y., et al. "Enhancement of single-photon emission from nitrogen-vacancy centers with TiN/(Al, Sc) N hyperbolic metamaterial." Laser Photonics Reviews 9.1 (2015): 120-127.

[50] Kidwai, Omar, Sergei V. Zhukovsky, and J. E. Sipe. "Effective-medium approach to planar multilayer hyperbolic metamaterials: Strengths and limitations." Physical Review A 85.5 (2012): 053842.

[51] Kidwai, Omar, Sergei V. Zhukovsky, and J. E. Sipe. "Dipole radiation near hyperbolic metamaterials: applicability of effective-medium approximation." Optics letters 36.13 (2011): 2530-2532.

[52] Jacob, Zubin, Igor I. Smolyaninov, and Evgenii E. Narimanov. "Broadband Purcell effect: Radiative decay engineering with metamaterials." Applied Physics Letters 100.18 (2012): 181105.

[53] Jacob, Zubin, et al. "Engineering photonic density of states using metamaterials." Applied physics B 100.1 (2010): 215-218.

[54] Pelton, Matthew. "Modified spontaneous emission in nanophotonic structures." Nature Photonics 9.7 (2015): 427-435.

[55] Poddubny, Alexander N., et al. "Microscopic model of Purcell enhancement in hyperbolic metamaterials." Physical Review B 86.3 (2012): 035148.

[56] Mahmoodi, Maryam, Seyed Hassan Tavassoli, and Andrei V. Lavrinenko. "Mode-resolved directional enhancement of spontaneous emission inside/outside finite multilayer hyperbolic metamaterials." Materials Today Communications 23 (2020): 100859.

[57] Popov, Vladislav, Andrei V. Lavrinenko, and Andrey Novitsky. "Surface waves on multilayer hyperbolic metamaterials: Operator approach to effective medium approximation." Physical Review B 97.12 (2018): 125428.

[58] Ginzburg, Pavel, et al. "Spontaneous emission in non-local materials." Light: Science Applications 6.6 (2017): e16273-e16273.

[59] Wells, Brian M., Anatoly V. Zayats, and Viktor A. Podolskiy. "Nonlocal optics of plasmonic nanowire metamaterials." Physical Review B 89.3 (2014): 035111.

[60] Krishnamoorthy, Harish NS, et al. "Topological transitions in metamaterials." Science 336.6078 (2012): 205-209.

[61] Ferrari, L.; Smalley, J.S.T.; Fainman, Y.; Liu, Z. Hyperbolic metamaterials for dispersion-assisted directional light emission. Nanoscale 2017, 9, 9034–9048.

[62] Channab, M., C. F. Pirri, and A. Angelini. "Funneling Spontaneous Emission into Waveguides via Epsilon-Near-Zero Metamaterials." Nanomaterials 11.6 (2021): 1410.

[63] Chen, Yifang. "Nanofabrication by electron beam lithography and its applications: A review." Microelectronic Engineering 135 (2015): 57-72.

[64] Leggett, Graham J. "Scanning near-field photolithography—surface photochemistry with nanoscale spatial resolution." Chemical Society Reviews 35.11 (2006): 1150-1161.

[65] Seisyan, R. P. "Nanolithography in microelectronics: A review." Technical Physics 56.8 (2011): 1061-1073.

[66] Xie, Zhihua, et al. "Plasmonic nanolithography: a review." Plasmonics 6.3 (2011): 565-580.

[67] Ferry, D. K., et al. "Nanolithography." Semiconductor Science and Technology 11.11S (1996): 1552.

[68] Alvarez-Fernandez, Alberto, et al. "Block copolymer directed metamaterials and metasurfaces for novel optical devices." Advanced Optical Materials 9.16 (2021): 2100175.

[69] Botiz, Ioan, and Seth B. Darling. "Optoelectronics using block copolymers." Materials Today 13.5 (2010): 42-51.

[70] Kulkarni, Ashish A., and Gregory S. Doerk. "Thin film block copolymer self-assembly for nanophotonics." Nanotechnology 33.29 (2022): 292001.

[71] Li, Tao, et al. "Wafer-scale nanopillars derived from block copolymer lithography for surface-enhanced Raman spectroscopy." ACS Applied Materials Interfaces 8.24 (2016): 15668-15675.

[72] Kim J Y et al. 2016 "Highly tunable refractive index visible-light metasurface from block copolymer self-assembly" Nat. Commun. 7 12911–12911

[73] Rasappa S, Hulkkonen H, Schulte L, Ndoni S, Reuna J, Salminen T and Niemi T 2019 High molecular weight block copolymer lithography for nanofabrication of hard mask and photonic nanostructures J. Colloid Interface Sci. 534 420–9

[74] Liapis A C, Rahman A and Black C T 2017 Self-assembled nanotextures impart broadband transparency to glass windows and solar cell encapsulants Appl. Phys. Lett. 111 183901–183901

[75] Singh, G.; Batra, S.; Zhang, R.; Yuan, H.; Yager, K. G.; Cakmak, M.; Berry, B.; Karim, A. ACS Nano 2013, 7 (6), 52915299.

[76] Liu, Chuan, Dong-Yoon Khim, and Yong-Young Noh. "Organic field-effect transistors by a solvent vapor annealing process." Journal of nanoscience and nanotechnology 14.2 (2014): 1476-1493.

[77] Basutkar, Monali N., et al. "Through-Thickness Vertically Ordered Lamellar Block Copolymer Thin Films on Unmodified Quartz with Cold Zone Annealing." Nano letters 17.12 (2017): 7814-7823.

[78] Leniart, Arkadiusz A., et al. "Macroscopic alignment of block copolymers on silicon substrates by laser annealing." ACS nano 14.4 (2020): 4805-4815.

[79] Jin, Hyeong Min, et al. "Flash light millisecond self-assembly of high block copolymers for wafer-scale sub-10 nm nanopatterning." Advanced Materials 29.32 (2017): 1700595.

[80] Mai, Yiyong, and Adi Eisenberg. "Self-assembly of block copolymers." Chemical Society Reviews 41.18 (2012): 5969-5985.

[81] Kim, Jang Hwan, et al. "Smart Nanostructured Materials based on Self-Assembly of Block Copolymers." Advanced Functional Materials 30.2 (2020): 1902049.

[82] Beaucage, Peter A., et al. "Superconducting Quantum Metamaterials from Convergence of Soft and Hard Condensed Matter Science." Advanced Materials 33.26 (2021): 2006975.

[83] Park, Haedong, et al. "Block copolymer gyroids for nanophotonics: significance of lattice transformations." Nanophotonics (2022).

[84] Thedford, R. Paxton, et al. "Superconducting Quantum Metamaterials from High Pressure Melt Infiltration of Metals into Block Copolymer Double Gyroid Derived Ceramic Templates." Advanced Functional Materials 31.23 (2021): 2100469.

[85] Kilchoer, Cédric, et al. "Hyperbolic Optical Metamaterials from Shear-Aligned Block Copolymer Cylinder Arrays." Advanced Photonics Research 1.2 (2020): 2000037.

[86] Elbs, Hubert, and Georg Krausch. "Ellipsometric determination of Flory-Huggins interaction parameters in solution." Polymer 45.23 (2004): 7935-7942.

[87] Willis, James D., Tom M. Beardsley, and Mark W. Matsen. "Simple and accurate calibration of the Flory–Huggins interaction parameter." Macromolecules 53.22 (2020): 9973-9982.

[88] Lin, C. C., et al. "Effect of molecular structure on the thermodynamics of block copolymer melts." Macromolecules 27.26 (1994): 7769-7780.

[89] Shen, Lian, et al. "Broadband enhancement of on-chip single-photon extraction via tilted hyperbolic metamaterials." Applied Physics Reviews 7.2 (2020): 021403.

[90] Thurn-Albrecht, Thomas, et al. "Nanoscopic templates from oriented block copolymer films." Advanced Materials 12.11 (2000): 787-791.

[91] Zalusky, Andrew S., et al. "Ordered nanoporous polymers from polystyrene polylactide block copolymers." Journal of the American Chemical Society 124.43 (2002): 12761-12773.

[92] Ting, Yuk-Hong, et al. "Plasma etch removal of poly (methyl methacrylate) in block copolymer lithography." Journal of Vacuum Science Technology B: Microelectronics and Nanometer Structures Processing, Measurement, and Phenomena 26.5 (2008): 1684-1689.

[93] Jung, Yeon Sik, and Caroline A. Ross. "Orientation-controlled self-assembled nanolithography using a polystyrene polydimethylsiloxane block copolymer." Nano Letters 7.7 (2007): 2046-2050.

[94] Bates, Christopher M., et al. "Polarity-switching top coats enable orientation of sub–10-nm block copolymer domains." Science 338.6108 (2012): 775-779.

[95] Peng, Qing, et al. "A route to nanoscopic materials via sequential infiltration synthesis on block copolymer templates." ACS nano 5.6 (2011): 4600-4606.

[96] Ghoshal, Tandra, et al. "Size and space controlled hexagonal arrays of superparamagnetic iron oxide nanodots: magnetic studies and application." Scientific reports 3.1 (2013): 1-8.

[97] Subramanian, Ashwanth, et al. "Three-dimensional electroactive ZnO nanomesh directly derived from hierarchically self-assembled block copolymer thin films." Nanoscale 11.19 (2019): 9533-9546.

[98] Subramanian, Ashwanth, et al. "Enhanced hybridization and nanopatterning via heated liquid-phase infiltration into self-assembled block copolymer thin films." ACS applied materials interfaces 12.1 (2019): 1444-1453.

[99] Peng, Qing, et al. "Nanoscopic patterned materials with tunable dimensions via atomic layer deposition on block copolymers." Advanced materials 22.45 (2010): 5129-5133.

[100] Kamcev, Jovan, et al. "Chemically enhancing block copolymers for block-selective synthesis of self-assembled metal oxide nanostructures." ACS nano 7.1 (2013): 339-346.

[101] Chai, Jinan, et al. "Assembly of aligned linear metallic patterns on silicon." Nature Nanotechnology 2.8 (2007): 500-506.

[102] Chai, Jinan, and Jillian M. Buriak. "Using cylindrical domains of block copolymers to self-assemble and align metallic nanowires." ACS nano 2.3 (2008): 489-501.

[103] Cummins, Cian, et al. "Aligned silicon nanofins via the directed self-assembly of PS-b-P4VP block copolymer and metal oxide enhanced pattern transfer." Nanoscale 7.15 (2015): 6712-6721.

[104] Ghoshal, Tandra, et al. "Fabrication of graphoepitaxial gate-all-around Si circuitry patterned nanowire arrays using block copolymer assisted hard mask approach." ACS nano 15.6 (2021): 9550-9558.

[105] Jin, Hyeong Min, et al. "Ultralarge area sub-10 nm plasmonic nanogap array by block copolymer self-assembly for reliable high-sensitivity SERS." ACS applied materials interfaces 10.51 (2018): 44660-44667.

[106] Banbury, Carl, et al. "Tuneable metamaterial-like platforms for surface-enhanced raman scattering via three-dimensional block co-polymer-based nanoarchitectures." ACS applied materials interfaces 11.15 (2019): 14437-14444.

[107] Kim, Ju Young, et al. "Highly tunable refractive index visible-light metasurface from block copolymer self-assembly." Nature communications 7.1 (2016): 1-9.

[108] Oh, Semi, et al. "Polarized ultraviolet emitters with Al wire-grid polarizers fabricated by solvent-assisted nanotransfer process." Nanotechnology 31.4 (2019): 045304.

[109] Roberts, Philip MS, et al. "Nanowire polarizers by guided self-assembly of block copolymers." Journal of Nanophotonics 8.1 (2014): 083091.

[110] Yang, Qiuyan, and Katja Loos. "Perpendicular structure formation of block copolymer thin films during thermal solvent vapor annealing: solvent and thickness effects." Polymers 9.10 (2017): 525.

[111] Pula, Przemyslaw, Arkadiusz Leniart, and Pawel W. Majewski. "Solvent-assisted self-assembly of block copolymer thin films." Soft Matter 18.21 (2022): 4042-4066.

[112] Jin, Cong, et al. "Nanopatterning via solvent vapor annealing of block copolymer thin films." Chemistry of Materials 29.1 (2017): 176-188.

[113] Cummins, Cian, et al. "Strategy for enhancing ultrahigh-molecular-weight block copolymer chain mobility to access large period sizes (> 100 nm)." Langmuir 36.46 (2020): 13872-13880.

[114] Park, Sungmin, et al. "Giant gyroid and templates from high-molecular-weight block copolymer self-assembly." Scientific reports 6.1 (2016): 1-9.

[115] Selkirk, Andrew, et al. "Optimization and control of large block copolymer self-assembly via precision solvent vapor annealing." Macromolecules 54.3 (2021): 1203-1215.

[116] Wang, Hyun Suk, Ki Hyun Kim, and Joona Bang. "Thermal approaches to perpendicular block copolymer microdomains in thin films: A review and appraisal." Macromolecular rapid communications 40.4 (2019): 1800728.

[117] Matsen, M. W. "Architectural effect on the surface tension of an ABA triblock Copolymer Melt." Macromolecules 43.3 (2010): 1671-1674.

[118] Mita, Kazuki, et al. "Cylindrical domains of block copolymers developed via ordering under moving temperature gradient." Macromolecules 40.16 (2007): 5923-5933.

[119] Bodycomb, Jeffrey, et al. "Single-grain lamellar microdomain from a diblock copolymer." Macromolecules 32 (1999): 2075-2077.

[120] Deng, Hai, et al. "Fast annealing DSA materials designed for sub-5 nm resolution." Advances in Patterning Materials and Processes XXXV. Vol. 10586. SPIE, 2018.

[121] Pang, Yuanyuan, et al. "Directed self-assembly of styrene-methyl acrylate block copolymers with sub-7 nm features via thermal annealing." Macromolecules 52.8 (2019): 2987-2994.

[122] Kim, Jang Hwan, et al. "Smart Nanostructured Materials based on Self-Assembly of Block Copolymers." Advanced Functional Materials 30.2 (2020): 1902049.

[123] Leniart, Arkadiusz A., et al. "Macroscopic alignment of block copolymers on silicon substrates by laser annealing." ACS nano 14.4 (2020): 4805-4815.

[124] Jacobs, Alan G., et al. "Control of PS-b-PMMA directed self-assembly registration by laser induced millisecond thermal annealing." Alternative Lithographic Technologies VI. Vol. 9049. SPIE, 2014.

[125] Majewski, Pawel W., and Kevin G. Yager. "Rapid ordering of block copolymer thin films." Journal of Physics: Condensed Matter 28.40 (2016): 403002.

[126] Berry, Brian C., et al. "Orientational order in block copolymer films zone annealed below the order disorder transition temperature." Nano letters 7.9 (2007): 2789-2794.

[127] Murataj, Irdi, et al. "Hyperbolic metamaterials via hierarchical block copolymer nanostructures." Advanced Optical Materials 9.7 (2021): 2001933.

[128] Lu, Dylan, et al. "Enhancing spontaneous emission rates of molecules using nanopatterned multilayer hyperbolic metamaterials." Nature nanotechnology 9.1 (2014): 48-53.

[129] Feynman R 1982 Simulating physics with computers Int. J. Theor. Phys. 21 467–88

[130] Buluta, Iulia, Sahel Ashhab, and Franco Nori. "Natural and artificial atoms for quantum computation." Reports on Progress in Physics 74.10 (2011): 104401.

[131] Henriet, Loïc, et al. "Quantum computing with neutral atoms." Quantum 4 (2020): 327.

[132] Daley, Andrew J. "Quantum computing and quantum simulation with group-II atoms." Quantum Information Processing 10.6 (2011): 865-884.

[133] Dumitrescu, Eugene F., et al. "Cloud quantum computing of an atomic nucleus." Physical review letters 120.21 (2018): 210501.

[134] Knill E, Laflamme R and Milburn G J 2001 A scheme for efficient quantum computation with linear optics Nature 409 46–52

[135] Liu, Chunsen, et al. "Two-dimensional materials for next-generation computing technologies." Nature Nanotechnology 15.7 (2020): 545-557.

[136] Pollard, R. J., et al. "Optical nonlocalities and additional waves in epsilon-near-zero metamaterials." Physical review letters 102.12 (2009): 127405.

[137] Einstein A, Podolsky B, Rosen N. Can quantum-mechanical description of physical reality be considered complete? Phys Rev 1935; 47: 777–780.

[138] Bell JS. On the problem of hidden variables in quantum mechanics. Rev Mod Phys 1966; 38: 447–452.

[139] Purcell, E. M. Spontaneous emission probabilities at radio frequencies. Phys. Rev. 69, 681 (1946).

[140] Shannon, Claude E. "Communication theory of secrecy systems." The Bell system technical journal 28.4 (1949): 656-715.

[141] Ford, George W., and Willes H. Weber. "Electromagnetic interactions of molecules with metal surfaces." Physics Reports 113.4 (1984): 195-287.

[142] Barnes, W. L. Fluorescence near interfaces: the role of photonic mode density. J. Mod. Opt. 45, 661–699 (1998).

[143] Litchinitser, Natalia M., Ildar R. Gabitov, and Andrei I. Maimistov. "Optical bistability in a nonlinear optical coupler with a negative index channel." Physical review letters 99.11 (2007): 113902.

[144] Inam, Faraz A., et al. "Emission and nonradiative decay of nanodiamond NV centers in a low refractive index environment." ACS nano 7.5 (2013): 3833-3843.

[145] Maletinsky, P., Hong, S., Grinolds, M. et al. A robust scanning diamond sensor for nanoscale imaging with single nitrogen-vacancy centres. Nature Nanotech 7, 320–324 (2012). https://doi.org/10.1038/nnano.2012.50

[146] Aurélien Cuche, Aurélien Drezet, Yannick Sonnefraud, Orestis Faklaris, François Treussart, Jean-François Roch, and Serge Huant, "Near-field optical microscopy with a nanodiamond-based single-photon tip," Opt. Express 17, 19969-19980 (2009)

[147] Zheng, Wentian. "Magnetic and electrical field detection using NV-based AFM." Bulletin of the American Physical Society 65 (2020).

[148] Ziv, Amir, et al. "AFM-Based Spin-Exchange Microscopy Using Chiral Molecules." Advanced Materials 31.40 (2019): 1904206.

[149] Kainuma, Yuta, et al. "Scanning diamond NV center magnetometer probe fabricated by laser cutting and focused ion beam milling." Journal of Applied Physics 130.24 (2021): 243903.

[150] Hong, Sungkun, et al. "Nanoscale magnetometry with NV centers in diamond." MRS bulletin 38.2 (2013): 155-161.

[151] Choi, Sumin, et al. "Enhancing optical readout from diamond AFM tips for quantum nanosensing." ACS Photonics 5.11 (2018): 4244-4248.

[152] Majewski, Pawel W., and Kevin G. Yager. "Millisecond ordering of block copolymer films via photothermal gradients." ACS nano 9.4 (2015): 3896-3906.

[153] Majewski, Pawel W., et al. "Arbitrary lattice symmetries via block copolymer nanomeshes." Nature communications 6.1 (2015): 1-6.

[154] R. Kurzweil, The Singularity is Near: When Humans Transcend Biology, The Viking Press, 2006, p. 67.

[155] Lee, Dasol, et al. "Hyperbolic metamaterials: fusing artificial structures to natural 2D materials." ELight 2.1 (2022): 1-23.

[156] Cara, Eleonora, et al. "Recent Advances in Sequential Infiltration Synthesis (SIS) of Block Copolymers (BCPs)." Nanomaterials 11.4 (2021): 994.

[157] Murataj, Irdi, et al. "Liquid Phase Infiltration of Block Copolymers." Polymers 14.20 (2022): 4317.

[158] Zheludev, Nikolay I., and Yuri S. Kivshar. "From metamaterials to metadevices." Nature materials 11.11 (2012): 917-924.

[159] Mu, Di, et al. "A review of research on seismic metamaterials." Advanced Engineering Materials 22.4 (2020): 1901148.

[160] Qi, Jixiang, et al. "Recent progress in active mechanical metamaterials and construction principles." Advanced Science 9.1 (2022): 2102662.

[161] Fang, Anan, Thomas Koschny, and Costas M. Soukoulis. "Optical anisotropic metamaterials: Negative refraction and focusing." Physical Review B 79.24 (2009): 245127.

[162] Novikov, V. B., et al. "Superluminal and slow femtosecond laser pulses in hyperbolic metamaterials in epsilon-near-zero regime." Optics Letters 46.10 (2021): 2276-2279.

[163] Li, Borui, Yingran He, and Sailing He. "Investigation of light trapping effect in hyperbolic metamaterial slow-light waveguides." Applied Physics Express 8.8 (2015): 082601.

[164] P. Lalanne, et al. "Quasinormal mode solvers for resonators with dispersive materials," J. Opt. Soc. Am. A 36, 686-704 (2019)

[165] G. S. Doerk, R. Li, M. Fukuto, K. G. Yager, Macromolecules 2020, 53, 1098.

[166] K. M. Baek, J. M. Kim, J. W. Jeong, S. Y. Lee, Y. S. Jung, Chem. Mater. 2015, 27, 5007.

[167] Ferrarese Lupi, F., et al. "Tailored and Guided Dewetting of Block Copolymer/Homopolymer Blends." Macromolecules 53.16 (2020): 7207-7217.